Interactions Between Grain Boundary Faceting, Migration and Grain Rotation: Color Group and Molecular Dynamics Simulation Approaches

Yue Huang

A dissertation submitted in partial fulfillment
of the requirements for the degree of

Doctor of Philosophy

University of Washington

2006

Program Authorized to Offer Degree: Department of Materials Science and Engineering

INFORMATION TO USERS

The quality of this reproduction is dependent upon the quality of the copy submitted. Broken or indistinct print, colored or poor quality illustrations and photographs, print bleed-through, substandard margins, and improper alignment can adversely affect reproduction.

In the unlikely event that the author did not send a complete manuscript and there are missing pages, these will be noted. Also, if unauthorized copyright material had to be removed, a note will indicate the deletion.

ProQuest Information and Learning Company
300 North Zeeb Road
P.O. Box 1346
Ann Arbor, MI 48106-1346

University of Washington
Graduate School

This is to certify that I have examined this copy of a doctoral dissertation by

Yue Huang

and have found that it is complete and satisfactory in all respects,
and that any and all revisions required by the final
examining committee have been made.

Chair of the Supervisory Committee:

Gretchen Kalonji

Reading Committee:

Gretchen Kalonji

Rajendra K. Bordia

Olof Hellman

Date: 11/22/06.

In presenting this dissertation in partial fulfillment of the requirements for the doctoral degree at the University of Washington, I agree that the Library shall make its copies freely available for inspection. I further agree that extensive copying of the dissertation is allowable only for scholarly purposes, consistent with "fair use" as prescribed in the U.S. Copyright Law. Requests for copying or reproduction of this dissertation may be referred to ProQuest Information and Learning, 300 North Zeeb Road, Ann Arbor, MI 48106-1346, 1-800-521-0600, to whom the author has granted "the right to reproduce and sell (a) copies of the manuscript in microform and/or (b) printed copies of the manuscript made from microform."

Signature Huang Yu

Date Nov. 28. 2006

University of Washington

Abstract

Interactions Between Grain Boundary Faceting, Migration and Grain Rotation: Color Group and Molecular Dynamics Simulation Approaches

Yue Huang

Chair of the Supervisory Committee:
Professor Gretchen Kalonji
Department of Materials Science and Engineering

Color group theory and molecular dynamics (MD) simulations were used to study the faceting and rotation of grains in nanocrystalline materials and their interactions. Color group arguments were used to determine symmetry-dictated extrema with respect to misorientation of the grains and with respect to grain boundary normal orientations. MD simulations were used to study the evolution of the system and to elucidate the interactions between grain rotation and faceting in nano-scale systems. The systems of study were fcc bicrystalline systems with two grains sharing their [110] directions. Two geometric parameters were studied: the misorientation between two grains with a common rotation axis in the [110] direction of both grains, and the grain boundary normal orientation of fcc (110) tilt grain boundaries.

The symmetry-dictated extremum (SDE) with respect to misorientation around both grains' [110] direction is 90 degrees. The SDE with respect to GB normal orientations for (110) tilt GBs are located on top of the color and classical mirror planes of their dichromatic patterns.

By using periodic boundary conditions and a cylindrical embedded grain structure in our simulations, grains are only free to vary the misorientation between grains

around the common [110] direction, and the normal of the grain boundaries are always perpendicular to both grains [110] direction. All SDE studied in our simulation are observed to be local energy minimum states. We observed the systems reducing their excess energy through three main modes: forming facets at the boundaries, rotating between the two grains, and reduction of grain boundary area through grain shrinkage.

Facets are formed in low-energy grain boundaries and oscillating rotation occurred when the initial misorientation was not a SDE. A new algorithm was developed to quantitatively measure the grain rotation. The ovsered rotations are not rigid-body rotations and have strong interaction with faceting. Systems with lower energy facets rotate less. Low energy facets are also impede the continuous rotation and shrinkage of the grains. Embedded grains with higher energy facets shrink faster. Grains shrink layer by layer through formation of stacking faults and movement of dislocations.

TABLE OF CONTENTS

Page

List of Figures iv

List of Tables ix

Chapter 1: Motivation of this Dissertation 1

Chapter 2: Introduction and Background 3

2.1 Grain Boundaries 3

2.2 Grain Growth Mechanisms: Grain Boundary Migration and Grain Rotation 6

2.3 Color Groups 13

2.3.1 Introduction to Color Groups 15

2.3.2 Several Concepts of Color Groups Used in This Study 16

Dichromatic patterns and 2-color Groups 16

Structure of Color Groups 17

Symmetry Dictated Extrema 18

Idealized Construction of Cyrstalline Interfaces 19

2.3.3 Application of color groups in materials science 20

2.3.4 The Group of the Wulff Plot 20

2.4 Molecular Dynamics Simulation 23

2.4.1 MD algorithm 24

2.4.2 Boundary Conditions 26

2.4.3 Potentials 27

2.4.4 Energy Minimization Method 28

2.4.5 Visualization 29

2.4.6 Structure 30

Chapter 3: Color Group Study 34
3.1 Introduction and the dichromatic patterns of the systems 34
3.2 Color group of the DCPs 37
3.3 Symmetry dictated extrema (SDE) study with respect to misorientation between the grains 39
3.4 SDE with respect to the orientation of grain boundary normal, $\hat{n}$ . . . 40
3.5 Morphology studies using the group of Wulff plot 45

Chapter 4: Molecular Dynamics Simulation: Software, Simulation Structure and Method, and Visualization Algorithm 48
4.1 Introduction to kSan 48
4.2 New algorithm for calculating the orientation value of the grain to which a particle belongs 49
4.2.1 Color particle by its energy 49
4.2.2 Algorithm of tracking particle's axis angle 53
4.3 Pressure of the simulations 60

Chapter 5: Grain Boundary Excess Energy and Simulations With Embedded Grains 64
5.1 Grain Boundary Excess Energy 64
5.1.1 Simulation structure and method of measuring grain-boundary excess energy 64
5.1.2 Results 74
5.1.3 Discussion 75
5.2 MD simulations with a columnar grain embedded in a bigger grain . . 78
5.2.1 Structure and method of simulation with a columnar grain embedded in a bigger grain 78
5.2.2 Results 80
5.2.3 Discussion 85
5.3 Quantifying the excess energy associated with GBs 87
5.3.1 Results 87
5.3.2 Discussion 89

Chapter 6: Faceting, Grain Rotation, and Grain Shrinkage Mechanism . . . 90
6.1 Results 90

6.1.1 Faceting of the grain 90
6.1.2 Interaction between stacking faults and grain boundaries . . . 93
6.1.3 Grain rotation 99
6.1.4 Grain shrinkage mechanism 118
6.2 Discussion 121
6.2.1 Discussion of faceting 121
6.2.2 Discussion of rotation 126
6.2.3 Discussion of shrinkage mechanism 130

Chapter 7: Conclusion 133

Bibliography 138

LIST OF FIGURES

Figure Number		Page
2.1	Harris observed grain rotation during annealing of a gold thin-film at 250^o in 1998. TEM images taken before annealing (a) and after annealing 1h (b), 2h (c), 3h (d).	9
2.2	Diagram of the diffusive fluxes required for grain rotation to occur, in an idealized case in Harris' paper.	10
2.3	In their research in 2002, Haslam et al. offer an atomic-level mechanism of the first rotation-coalescence event from the viewpoint of the atoms in the grain interiors.	11
2.4	Sample of DCP of color symmetry	17
2.5	Possible property versus geometric parameter plot: example for the SDE	18
2.6	Six stpes of constructing a crystalline interface.	21
2.7	Schematic of the 3D periodic simulation cell for the synthesis of the bicrystal, indicating the crystallographic orientation of the seeds and the dimensions of the simulation cell.	30
2.8	Position and nearest neighbor miscoordinations of atoms in a slice of thickness 0.5 a_o centered about x=0 in the MD-grown bicrystal.	31
2.9	(a) The initial microstructure with 25 grains with a grain diameter of 15 nm is clearly delineated by the miscoordinated atoms. (b) The structure after simulation for 7.2 ns.	32
3.1	DCP of sample system 1 with two kinds of grain misorientated to each other by 90 degrees around the common [110] direction of both grains with mirror planes indicated by solid lines.	35
3.2	DCP of sample system 2 with two kinds of grain misorientated to each other by 45 degrees around [110] direction of both grains with mirror planes indicated by solid lines.	36
3.3	a) DCP with $R = 90^o - \delta$, b) DCP with $R = 90^o + \delta$.	40
3.4	a) DCP with $R = 45^o - \delta$, b) DCP with $R = 45^o + \delta$	41

3.5 DCP with R=90. The classical-mirror plane boundaries are identified by black solid lines; the color-mirror plane boundaries are identified by blue solid lines. 42
3.6 Classical mirror plane boundary: grain boundary on top of the classical-mirror plane with $\theta = 90^o$. 43
3.7 Color mirror plane boundary: grain boundary on top of the color-mirror plane with $\theta = 45^o$. 44
3.8 SDE study for $\theta = 90$, with a) $\theta = 90 + \delta$ and $\theta = 90 - \delta$. 45
3.9 SDE study for $\theta = 45$, with a) $\theta = 45 + \delta$ and $\theta = 45 - \delta$ 46

4.1 Color particles according to the sum of the potential energy and kinetic energy of each particle 50
4.2 A snapshot taken around 70000 simulation steps at 800 degrees with one columnar-shaped grain embedded in another. R_o=35.26 degrees. . 52
4.3 Flow chart of the new algorithm that assigns an angle value to each particle according to the orientation angle of the grain to which it belongs. 53
4.4 FCC structure, the red particle is the object particle, the other particles are colored according to their distance to the object particle. 55
4.5 FCC structure, object particle is the red particle in the center; blue plane is the FCC (110) plane passes through the object particle. The other particles are colored in the same way shown in Figure 4.4. . . . 56
4.6 Splat function, which assigns values between 0 to 0.75. 59
4.7 Calculated axis angle value versus orientation value of the grain to which the particle belongs. 61
4.8 Color particles by using each particle's axis angle, before we started simulation. R_o=35.26 62

5.1 The structure used in studying the grain boundary excess energy. . . 66
5.2 The structure used in studying the excess energy of the grain boundary: the E_{total} only included the energy of the particles in the dashed lined rectangular area. 67
5.3 The structure used in studying the energy of the grain boundary with only one grain boundary included into calculation: the E_{total} only included the energy of the particles in the dashed lined rectangular area. 68
5.4 This illustration shows the area that will be influenced by the periodic boundary conditions for the second structure design of the grain boundary excess energy measurement simulation. 70

5.5 The simulation structure that we need to use for higher temperature. 71
5.6 The simulation structure that we need to use for higher temperature. 72
5.7 The simulation structure that we need to use for higher temperature. 73
5.8 The excess energy of the grain boundaries in the fcc structure at 15 K and 500 K. 76
5.9 The possible Wulff plot of two fcc (110)//(110) systems. 77
5.10 The excess energy of the grain boundaries in the fcc structure at 800 K. 78
5.11 The column-shaped embedded grain. 78
5.12 Thermal equilibration of the system. 81
5.13 Potential energy of the system versus simulation time with longer simulation time. 82
5.14 Potential energy of the system versus simulation time of simulation with $R_o = 90^o$, with imbedded grain disappearing at an early stage of the simulation, around 35ps, which is about 35000 simulation steps. . 83
5.15 Sample plot of total potential energy of the system versus simulation time of simuatlion with $R_o = 90^o$, with imbedded grain disappearing at the end of simulation. 83
5.16 Sample plot of total potential energy of the system versus simulation time of simulation with $R_o = 35.26^o$, with imbedded grain disappearing around the 94.5ps. 85
5.17 Sample plot of total potential energy of the system versus simulation time of simulation with $R_o = 90^o$, with imbedded grain disappearing around the 35ps. 86
5.18 Snapshot of one simulation with original $R_o = 35.26^o$ taken after 76ps, with grain boundaries marked by color lines. 88
6.1 The snapshot taken in one of simulations with $R_o = 35.26^o$ and its DCP. Same grain boundaries are indicated by same colors on both the snapshot image and DCP. 91
6.2 The snapshot taken in one of the $R_o = 90^o$ simulations and the DCP of it. We used the same color to indicate the same boundary on the snapshot and the DCP of FCC (110) with $R_o = 90^o$. 91
6.3 Similar shapes were achieved for these two different simulations with exactly same grain boundaries formed. 92

6.4 A snapshot also taken around the 10,000th step (10ps) for the simulation with continual shrinkage, compared with the DCP pattern of $R_o = 35.26^o$. 93
6.5 Volume percentage changes of the embedded grain during simulation. 94
6.6 A snapshot taken after 1000 steps for the rotation with $R_o = 35.26^o$; the stacking faults exist both in the embedded grain and the enclosed grain, with only one direction for each grain. 96
6.7 A snapshot taken after 5000 steps for the simulation with $R_o = 35.26^o$; Another stacking fault with a dislocation at the end starts forming and grow through the movement of the dislocation 97
6.8 A snapshot taken after 26000 steps for the simulation with $R_o = 35.26^o$; the stacking faults exist both in the embedded grain and the enclosed grain, with only one direction for each grain. 98
6.9 A snapshot taken after 25000 steps for the simulation with $R_o = 35.26^o$; the embedded grain has a capsule shape in the cutting face, instead of a round one. The stacking faults exist both in the embedded grain and the enclosed grain, still with only one direction for each grain. 100
6.10 A snapshot taken after 53000 simulation steps of a simulation with $R_o = 45^o$. 101
6.11 Change of the rotation angle with simulation time for the simulation with $R_o = 45^o$; data were taken during simulation at every 0.02ps. . . 103
6.12 Snapshot taken before simulation with $R_o = 70^o$. 104
6.13 Snapshot taken after 2ps of simulation with $R_o = 70^o$. 105
6.14 Change of the rotation angle with simulation time for the simulation with $R_o = 70^o$; data were taken during simulation every 0.02 ps. . . . 106
6.15 Distribution of the angular values taken at every 0.5ps for all selected particles for the simulation with $R_o = 70^o$. 107
6.16 Change of the rotation angle with simulation time for the simulation with $R_o = 35.26^o$; data were taken during simulation every 0.02ps. . 109
6.17 Change of the misorientation angle with simulation time for the simulation with $R_o = 90^o$; data were taken during the simulation at every 20 steps. 110
6.18 R value versus time for single crystal which has no rotation. 111
6.19 Distribution of the angular values taken at every 0.5ps for all selected particles for the simulation with $R_o = 90^o$. 112
6.20 Facet formed in 2ps of the simulation while rotation lasts much longer. 113

6.21 These two snapshots were taken right before and after rotation in one of the $R_o = 35.26^o$ simulations, which corresponds to the first energy drop on Figure 5.16. 114
6.22 Snapshots to show how dislocation interacts with plan glide to change the orientation of part of the grain. 115
6.23 At the later stage, the embedded grain of simulation R45-101905 divided into three grains. Even though more grain boundaries were created in the system, the total potential energy decreased, as shown in the plot on the left. 116
6.24 Before the rotation, the grain is surrounded by mostly high-energy general grain boundaries; the place where rotation occurred had more dislocations and greater excess volume than did other sites. 117
6.25 After the rotation, the grain is surrounded by mostly low-energy grain boundaries of as shown on the Tri-chromatic pattern. 118
6.26 Two snapshots taken at different shrinkage stages of a simulation with $R_o = 35.26^o$. From the images we can tell that the although the inside grain's volume was changing, the direction of facets did not change much. 119
6.27 These two snapshots illustrate how stacking fault, dislocation, and glide system of the FCC worked together to move the particles around the grain boundaries. 120
6.28 Total energy versus simulation time after temperature is raised to 1500K after simulation has been run for 150ps at 800K. 122
6.29 Shrinkage of the grain at high temperature 123
6.30 The structures we used to calculate the stacking faults in (111) plane. 3 stacking faults are included. 132

LIST OF TABLES

Table Number Page

4.1 The energy values before and after changes of system volume at different simulation steps. 63

5.1 The energy of the color mirror plane grain boundary with 60-degree misorientation between two grains with different simulation sizes, calculation scopes, and simulation steps. 69

5.2 The average grain boundary excess energy of color mirror plane grain boundary measured by using different sampling size in width and length with different simulation duration. 73

5.3 The energy of grain boundaries with different geometrical parameters of fcc system taken at T=15K and T=500K. The unit of the grain boundary is eV/nm^2. 75

5.4 The excess energy of grain boundaries with different geometrical parameters of the fcc system taken at T=800K. The unit is eV/nm^2. . . 76

5.5 Table for the average energy at different stages of the simulation for some sample simulations. 84

6.1 The average energy per particle in different areas of the structure with stacking faults attached to the grain boundaires. 99

6.2 The ranges of the rotation after equilibration for simulations started with different R_o 108

ACKNOWLEDGMENTS

I sincerely thank my advisor, Gretchen Kalonji, for her support and encouragement throughout my research project. Her positive attitude in facing difficulties and the fact that she never gives up in the hardest situations will always encourage me to pursue the best in any circumstance. As an advisor, a friend, and a spiritual mentor, she gave me more than a professor can give to a student, a friend can offer to another friend, and a mother can hand to her own daughter.

No words can describe the sincere appreciation I have for Olof Hellman for his advice, encouragement, and support. I learned from him that research is not only inspiring and exciting, but also enjoyable and satisfying. My long discussions with him turned the most difficult obstacles into the most interesting challenges, and eventually became the most joyful accomplishment. I also thank Tomo Hellman, Staffan Hellman, and Aina Hellman for their patience and the friendship they offered to me. Their house is one of my favorite places in Seattle because it is full of love, care, and joy.

Even though my parents and brother have not been in Seattle during these five years, their trust, encouragement, and love have never left me throughout this project. They always have faith in me but never leave me alone to face the difficulties. From them I know what is real love and how to love life, love myself. I can not describe how grateful I am to have such a great family. I am proud of them and hope this thesis will make them feel the same way of me.

I sincerely thank Mr. Sidney Rittenberg, Yuling Ritternberg and Jenny Ritternberg. They offered another home for me on Fox Island and always stood behind me

when I felt uncertain about life. They used their own life experiences to teach me that love is bigger than anything, especially loving life, and nothing worth more than dedicate our life into meaningful works that helps the other people.

I want to thank my committee: Profressor Bordia, Professor Brush, Professor Dunham, and Professor Cooper. They all gave me great help and support in this project, especially after my advisor transfered to another campus. They made sure I remained in good standing on this campus and they supported me in every aspect of this project.

Special thanks to Denice Denton. As a great woman scientist, she showed me the basic and important qualities of a researcher. I also cherish all the joyful moments I had with her. She will always live in my memory and heart.

I also want to express my sincere appreciation to my dear friends: Zizhen Yao, Yaodong Liu, Shanying Liang, Chou Zhou, Yu Zhao, Ray Berntsen, Zixiao Pan, Kyobi Hinami, Nancy Meenen, Shin Shin Hsia, Harvard Wang, Loc Uyen, Savatei Sea, Yuping Bao, Hanson Fong, Jessica Torrey, Marcella Gonzales, Aaron Feaver, Nik Hrabe, Kelli Roberts, Julie Bardecker, Pisun Xu, Ning Chen, and Eddie Schmit for their friendship and love. They are the reason I can keep smiling every day.

DEDICATION

To My Parents, Huang Jiadong and Huang lin.

Chapter 1

MOTIVATION OF THIS DISSERTATION

Nanocrystalline materials have attracted much attention for their special properties. However, with grain-size ranging from several nanometers to several hundreds of nanometers, grain stability is difficult to achieve and is one of the biggest barriers to application. Therefore, it is critical to understand the grain growth and/or shrinkage mechanisms of nano-sized grains. It is widely agreed that grain boundary migration processes dominate the morphology changes of polycrystalline materials with grain-size less than 30 nm. Although observation and reports of grain rotation are rare, several experimental observations and molecular dynamics (MD) simulations showed that grain rotation played a role equal to grain boundary migration in nano-scale grain growth. Some simulation studies attempt to understand the morphology changes of nano-grains based on the mechanism of grain boundary migration. However, by using mesoscopic methods, they ignored the interactions between grains at the atomic level at boundaries and grain junctions, and thus are limited in discussing the role of interfaces and misorientation of adjacent grains in system evolution. Even studies that observed grain rotation in their simulations used a rigid-body rotation model, which assumed that grain rotation is an independent process from grain boundary migration, but the researchers did not give solid reasons to explain this assumption.

We began our study by asking the following questions: How do geometric parameters influence a grain's properties, especially morphology and stability of the grain? Are there any interactions between interfacial faceting and grain rotation? If there are, how does interface normal direction and excess energy influence grain rotation?

What is the mechanism of grain rotation and grain boundary migration? And, does the bicrystalline symmetry influence both faceting and grain rotations?

To answer these questions, we first need to understand the properties of the grain boundaries. We used two different methods to study grain boundary systems. We first studied our polycrystalline system using a theoretical tool called color groups. Color groups give us information about the symmetry of the systems, and more importantly, tell us the special geometric parameters that result in a system with extremum properties, either maximum, minimum or saddle point. These special geometric positions are called symmetry-dictated extrema (SDE) of the system. Then, we used molecular dynamics (MD) computer simulations to observe the evolution of systems beginning with special geometrical characteristics, which provided information on the relation between the geometric parameters and the properties of the grain boundaries.

Chapter 2

INTRODUCTION AND BACKGROUND

2.1 Grain Boundaries

During the last two decades, polycrystalline materials with grain sizes on the nanoscale have been the objects of extensive study. Since the grain size is on the nanoscale, up to as much as half of the atoms belong to, or are affected by, the presence of the interfaces. These interfaces are mostly grain boundaries. [1] Therefore, characterizing the structure and the properties of the grain boundaries becomes an essential focus of nano-science.

The existence of grain boundaries results in extra energy to the system, called grain boundary excess energy. Grain boundary properties, such as impurity segregation, mobility and fracture, diffusion and cavitation, are related strongly to grain boundary excess energy. [2] Three classes of grain boundary geometric parameters will influence grain boundary energy: the misorientation between two grains, the orientation of the grain boundary plane normal, and the translation parallel or perpendicular to the grain boundary plane. Read et al. [3] described these three aspects of geometrical structures of grain boundaries by five macroscopic degrees of freedom (DOFs), among which three are used to characterize the mis-orientation and two are used to describe the normal of the planes. [2, 4, 5] However, Kalonji [6] pointed out that to fully determine a grain boundary, a sixth macroscopic DOF is necessary to describe the position of the grain boundary plane along the normal of the plane. Another three microscopic DOFs are needed to describe the rigid-body translations of the grains, parallel and/or perpendicular to the grain boundary plane. Previous research related the influence of microscopic DOFs on the grain boundary excess energy to the volume

expansion of the structure at the grain boundary. [7, 8] These microscopic DOFs only describe translation on a length scale that is on the order of the atomic plane spacing; hence, their influence on grain boundary energy is difficult to distinguish from the influence of the local atomic structure of the grain boundary and does not play an important role in a fully relaxed grain boundary system. Therefore, this report will mainly focus on discussing the relation between the macroscopic DOFs and the properties of the grain boundary system.

The coincidence site lattice (CSL) is the most popular model in explaining the relationship between geometric DOF's and properties of grain boundaries. The CSL is a super structure that has special rotations between two grains in a bicrystalline system. In a CSL, two grains' infinite lattice structure have certain percentage of the lattice points exactly on top of each other. The value of Σ represents the portion of the coincident lattice points in the three dimensional pattern, and Σ grain boundaries are the special grain boundaries with high reciprocal density of CSL points. [9] Most investigations of the relation between the structure of grain boundaries and the energy of the grain boundaries to date focus on the special properties of symmetrical grain boundaries and Σ grain boundaries, and use the classification of the grain boundaries based on the CSL model. Considerable experimental evidence indicates that some low Σ grain boundaries have lower energy than those of "random" or general boundaries. [10, 9, 11, 12] The excess energy of special planar grain boundaries (such as twin boundaries) has been measured as a function of misorientation of adjacent grains, in which energy cusps are observed at several special misorientations, and are explained by using low Σ grain boundaries of CSL models. However, not all of the expected low Σ energy cusps were observed experimentally. [2, 9, 13]

Several groups used different methods to study the influence of misorientation on the excess energy of the grain boundaries, such as examining small single crystals that were produced on crystalline substrates by a sintering technique. The distribution of the misorientation of the single crystals did not have a random form, revealing

that the system had preferred misorientations. [14, 15, 16] However, several CSL misorientations predicted to have low energy were not observed in these experiments.

The results from different studies bring the completeness of the CSL model into question. Some groups believe that the experiments have not shown some predicted CSL misorientations because other factors besides the geometric parameters influence the properties of the structure, such as chemical structure and electronic interactions of species [9], solute segregation [17] and the saturation of the bonds in covalent solids. [13] Some researchers went further and concluded that grain boundary faceting in some alloys cannot be explained by geometric requirements of the CSL. [18]

Some researchers have suggested that Σ models of boundary structure can be used to explain grain boundary excess energy because the grain boundary excess energy is due to mismatch of the atoms at the boundary from the positions they would occupy in a perfect lattice. [19, 20] If this explanation is valid for the low-energy boundaries, then energy cusps should be observed in some cases that allow the best atomic fit at the boundary, such as coherent twin boundaries and some other low Σ grain boundaries. However, in the experiment of measuring the boundary energy with the variation of incoherence of the boundary, only very small cusps [21], or none at all [22], were found at coherent boundaries. This shows that this assumption is still not the right explanation for special grain boundaries.

All these studies reveal that geometric structure of the grain boundaries is connected to the properties of grain boundaries, especially grain boundary excess energies. However, CSL and the other models to date cannot fully explain the relation between structure and grain boundary excess energy. In our study, we found several low excess energy boundaries which are not CSL grain boundaries. The following chapters provide detailed discussion.

2.2 *Grain Growth Mechanisms: Grain Boundary Migration and Grain Rotation*

Grain boundaries are considered to be the active regions in polycrystalline materials due to their high energy. Many properties of nano-crystalline materials are believed to be related to grain boundary movement and faceting. For example, movement of grain boundaries and dislocations are critical in controlling deformation and fracture behavior of materials. For larger grain sizes (of 50–100 nm), grain growth is dominated by dislocation processes. For lower grain-sizes (<30 nm) a grain boundary-based grain growth process is dominant, in which grain boundary migration results in a reduction of yield and flow stress. [23, 24, 25] Due to the great amount of grain boundary area in nano-crystalline materials, grain growth (shrinkage) significantly influences the thermodynamic stability of nano-crystalline materials. Therefore, understanding grain growth mechanisms is important to the application of nanomaterials.

The conventional explanation of grain growth is that it is driven by the reduction of the total area of grain boundaries in materials. A curvature driven mechanism, analogous to the growth of cells in soap froths, is widely used in discussing the grain boundary migration by equation 2.2.1. [26]

$$D^{\frac{1}{n}} - D_0^{\frac{1}{n}} = k't \tag{2.2.1}$$

Here D is the curvature radius of the grain after shrinkage and D_0 is the original curvature radius; n is an empirical parameter; t is time; k' is grain growth speed. However, the value of n seems to change case by case for all these studies. For example, Ganapathi et al. [26] found their grain growth data on nano-crystalline Cu fit the equation with n equal to $\frac{1}{2}$, $\frac{1}{3}$, $\frac{1}{4}$; Kriall and co-workers [27] re-evaluated Marlow and Loch's results [28], whose n equaled to 0.32, etc. Moreover, the results of some grain growth studies cannot fit into this equation, and were called "abnormal grain growth". [29, 30] The assumption for this growth mechanism is that the grain's shape is close to spherical, and won't change during grain growth.

Classical theoretical studies of grain growth have considerable difficulties in fully explaining the mechanism of grain growth. Thus, researchers used computer simulations to study modes of grain growth, mostly in two-dimensional model systems. A variety of approaches have been used in mesoscopic simulations, such as grain boundary-dynamics models [31, 32], vertex models [33, 34], Potts models [35, 36], Voronoi tessellation [37], and mean-field models [38]. In these simulation studies, grain boundaries and grain junctions are treated as single objects without considering their atomic structure. Therefore, although these methods are computationally highly efficient, they often requires full knowledge of the physical laws which govern the evolution of the microstructure and the properties of the defects, for example, the excess energy of the grain boundaries and the activation energy for the movement of grain boundaries. According to Haslam et al. [39], such detailed material information is not always available, either from experiments or from atomic-level computer simulation. In some way, these mesoscale grain boundary simulations are based on simplified assumptions that are not very solid. For example, the trijunctions and grain boundaries are assumed to be a negligible volume fraction of the material. However, with decreasing grain size, the fraction of atoms belonging to the grain boundaries increases rapidly. Therefore, the simulations of grain boundary and junctions that do not consider the volume and atomic structure of grain boundaries are no longer practical. Moreover, in most mesoscale simulations, the trijunctions are assumed to be much more mobile than grain boundaries. However, it has been proven that this is not always true. [40] Srinivasan et al. [41] even found that trijunctions can have negative excess energy.

Mesoscale grain boundary simulation is also limited in studying the role of misorientation of adjacent grains in system evolution. Without considering the atomic-level interaction around grain boundaries, it is impossible to observe the rotation of grain in mesoscale grain boundary simulation. Although grain rotation is not usually considered to be an important mechanism of microstructural development, and the direct

experimental observation of grain rotation is relatively difficult, several groups observed the rotation of small grains during the deformation and coalescence of grains, such as Ke et al. in 1995 [42], Yamasaki et al. in 1996 [43], and Harris et al. in 1998. [44] Harris et al. observed the changes in angles between twins in adjacent grains in the process of annealing of their columnar-structured thin-film materials, and concluded that rotation occurred between these adjacent grains. Their results are shown in Figure 2.1. They believed that stress played at most a minor role in driving the rotation of the grains, and the rotation of a single grain was driven by the motivation of decreasing grain boundary excess energy. They assumed that their grains were rigid bodies and rotation occurred without changing of the size and the shape of the grains, as illustrated in the Figure 2.2. The driving force of the rotation was provided by the aggregate energy gradient with respect to misorientation as given in equation 2.2.2:

$$\Delta E_m = -\frac{16\Omega a_0}{L^2}\Sigma_i\left(\frac{\partial\gamma_i}{\partial\theta}\right) \tag{2.2.2}$$

Here a_0 is the atomic jump distance, and $\Sigma_i\left(\frac{\partial\gamma_i}{\partial\theta}\right)$ is an aggregated energy gradient of all of the boundaries. Ω is the atomic volume, and L is the the boundary length of the grain. Here they assumed their grain had a hexagonal shape with same length of grain boundaries at each face of the grain.

The vacancy flux generated by this equation is:

$$J = \frac{D_V}{\kappa T}C_V\frac{16\Omega}{L^2}\Sigma_i\left(\frac{\partial\gamma_i}{\partial\theta}\right) \tag{2.2.3}$$

Harris and colleagues concluded that the rates of grain rotation were consistent with a mechanism based on diffusion-limited grain boundary sliding in response to the variation of grain boundary energy with misorientation.

Their study also mentioned structural effects of grain rotation. Grain rotation is related to the existence of the Σ grain boundaries in the structure. They studied different Σ grain boundaries and concluded that rotation tended to occur in the grains with high Σ grain boundaries, rather than in the grains with low Σ grain boundaries.

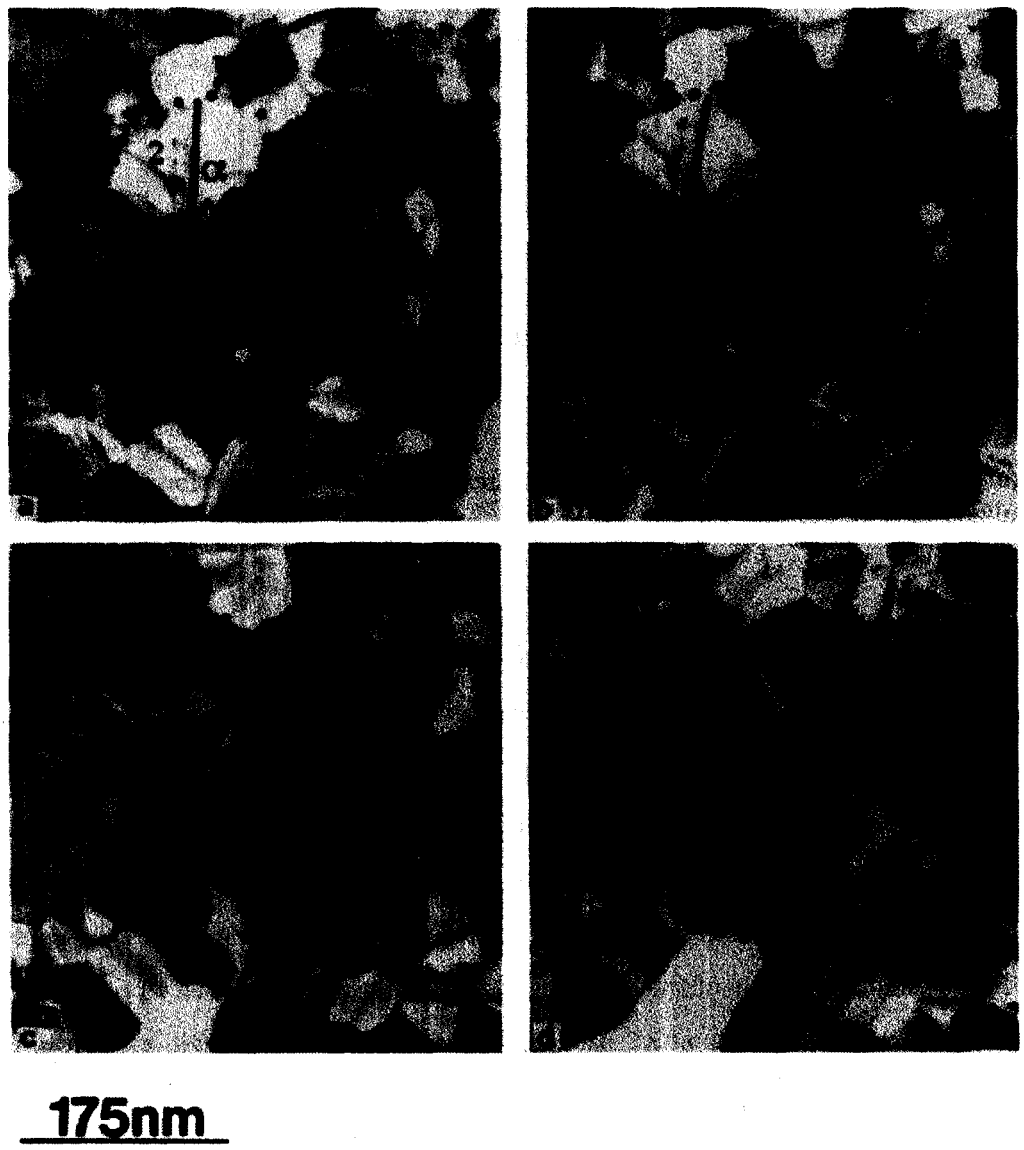

Figure 2.1: Harris observed grain rotation during annealing of a gold thin-film at 250^o in 1998. TEM images taken before annealing (a) and after annealing 1h (b), 2h (c), 3h (d).

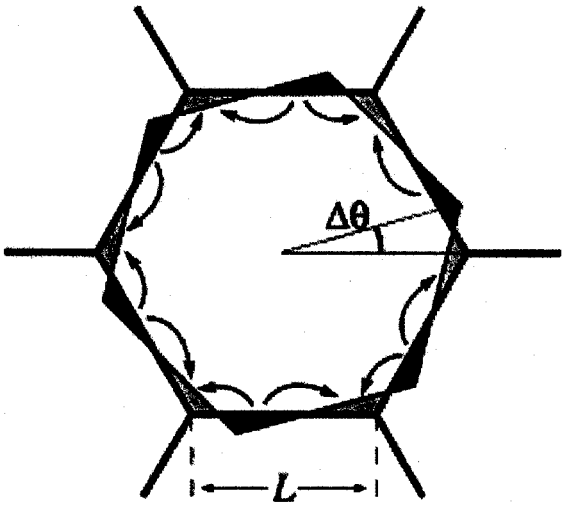

Figure 2.2: Diagram of the diffusive fluxes required for grain rotation to occur, in an idealized case in Harris' paper.

Their simulations did not study general grain boundaries. The limitation of the research of Harris et al. was that they treated grains as rigid-body objects and the interaction between atoms at the boundary was neglected. To involve the interactions between atoms at boundaries, other researchers used MD simulation to study grain boundary properties and deformation mechanisms. Without making any assumption as to the physical properties of grain boundaries and trijunctions, most researchers see MD simulation as one of the best tools in studying grain boundary properties and behaviors. In 2001, Haslam et al. used MD simulation to study grain growth in face-centered cubic (fcc) metals. [45] In their simulation work, Haslam et al. also revealed that, in addition to the conventional mechanism of grain growth by curvature-driven grain boundary-migration, grain rotation played an equally important role. [39]

In Figure 2.3 [39], the solid lines indicate $< 110 >$ directions. Image (a) gives the initial configuration of grain 8, 14, 16, with $\theta_{8-14} \approx 18^o$; image (b) gives the TEM snapshot after t=1.11 ns, $\theta_{8-14} \approx 11^o$; image (c) gives the snapshot after t=1.47 ns, $\theta_{8-14} \approx 9^o$; and after t=1.83 ns, as shown in image (d) $\theta_{8-14} \approx 4^o$. Haslam et al.

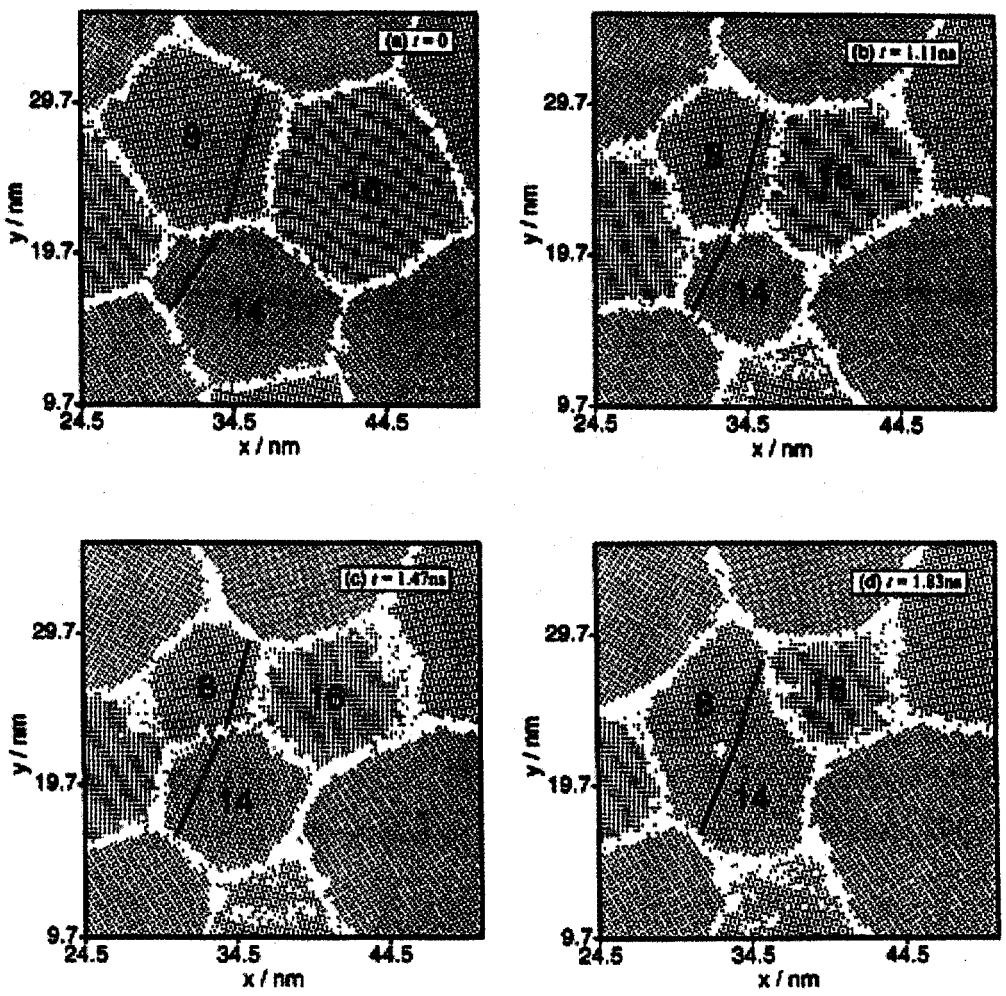

Figure 2.3: In their research in 2002, Haslam et al. offer an atomic-level mechanism of the first rotation-coalescence event from the viewpoint of the atoms in the grain interiors.

observed that grain 14 coalesced with grain 8 after $\sim 2.2ns$; after$\sim 2.3ns$, grain 16 suddenly started to rotate until it coalesced with the combined new grain 8-14; the resulting larger grain 8-14-16 subsequently coalesced with another grain after $\sim 3ns$, which is not shown in Figure 2.3. Noticing the decreasing areas of grain 8 and 16, and the initially decreasing and later again increasing area of grain 14, Haslam et al. concluded that the rotation-coalescence and grain boundary-migration mechanisms of grain growth were intimately coupled. They used a torque theory to explain why the rotation-coalescence mechanism was activated in one region of their sample but not the other. The angular velocity, ω_i, with respect to an axis through the center of the mass of grain i was given by:

$$\omega_i = M_i \tau_i \tag{2.2.4}$$

where M_i is the "rotational mobility" of grain i subject to a torque τ_i. For the columnar microstructure, the torque per unit column height is given by:

$$\tau_i = \Sigma_j \left(\frac{\partial \gamma_{ij}}{\partial \theta_{ij}} \right) L_{ij} \tag{2.2.5}$$

here γ_{ij} is the energy of the grain boundary between grain i and one of its neighbors j, θ_{ij} is the misorientation angle about $< 001 >$, and L_{ij} is the length of the grain boundary segment. Then the equation 2.2.4 will be modified to:

$$\omega_i = \frac{C_j}{2d_i^4} \Sigma_j \left(\frac{\partial \gamma_{ij}}{\partial \theta_{ij}} \right) \tag{2.2.6}$$

here C_j is a constant representing the atomic volume and temperature; d_i is the diameter of grain i.

Equation 2.2.6 was used in their research to approximately predict the angular velocity of any grain in the microstructure at any instant.

Again, this whole discussion was based on Harris' assumption that rotation was rigid body rotation and should be treated separately from the grain boundary migration. To use equation 2.2.6 on their non-hexagonal shaped grains, Harris et al. [44]

used a shape factor to modify C_i. However they assumed the shape of the grains remained unchanged during the rotation and even the shrinkage of the grains. According to this assumption, τ_i will decrease proportionally with the decrease of the grain size during shrinkage. However, even in their own study, they found that τ_i remained nearly constant for a significant amount of time while the grain decreases steadily.

Coupling between grain boundary migration and grain rotation was also briefly discussed by Haslam et al. [45] Although they thought interaction between grain boundary migration and grain rotation existed, they did not give a detailed model of the interplay between grain rotation and grain boundary migration. Their research pointed out two things: 1) Rotation mobility increased if the size of the grain was reduced by grain boundary migration. 2) While the grain shrank, although the shape of the grain changed, the rotation toque, τ_i, was maintained or even increased during grain boundary migration.

Understanding the interactions between faceting, shrinking, and rotation of the grains is one of the main topics of our study. In our MD simulations, we observed more interplay between grain rotation and grain boundary migration related to the geometric characteristics of the system, which will be discussed in the following chapters.

2.3 Color Groups

Crystallography started from the 17th century when people first connected observed properties of crystals to the internal order of "atomic" units. Researchers using point groups and space groups discovered the important role symmetry played on physical properties of a single crystal. [46] However, as materials scientists, we rarely study perfect single crystals. Imperfections in crystalline materials, such as grain boundaries, could dominate the physical properties. All these defects can exhibit symmetries of their own, which may be used to explain the properties of the structure with defects.

To extend the symmetry study to more realistic material systems with defects, Shubnikov and Belov [47] introduced black and white groups in the 1960's, known as "Shubnikov groups". Later, Shubnikov groups became the most applied color groups in describing the properties of magnetic materials.

In 1982, Kalonji [6] gave the first application of black and white groups to the study of grain boundaries. She for the first time derived the dichromatic pattern (DCP) to illustrate the rotation and translation relations of bicrystalline structure, and studied the symmetry of the DCPs using black and white groups. She studied the role of interfacial symmetry in the derivation of constraints upon the physical properties of interfaces and of polycrystalline aggregates. The applications included derivation of the group of Wulff plot in studying the morphology of crystal in a cyrstalline environment; symmetry dictated extrema of an interfacial system with the variation of geometric parameters; and symmetry constraints to the tensor properies and quantum mechanical properties of interfacial systems.

In 1989, Bendersky and Cahn [48] reported and thoroughly discussed a structure with icosahedral symmetry in Al-Mn-Fe-Si alloys. They found that their "general" grain boundaries (there is no coincident site lattice) were special with very low energy. They were not defined twin boundaries, but symmetry studies showed they were symmetry-dictated extrema. Their study suggested a re-examination of the concepts of twinning and grain boundaries that rely on CSL. They pointed out that the icosahedral symmetry was achieved by arranging five finer grains around a axis with 72^o degrees separation. These works suggested the uses of color symmetry in studying ploycrystalline materials. In the following sections I will first explain color groups and introduce several basic concepts that will be used in our study. Then I will review the literature on applications of color groups in materials science. Finally, I will introduce a special aspect of color symmetry: the group of the Wulff plot, which is useful in studying the morphology of grains growing in a crystalline environment.

2.3.1 Introduction to Color Groups

In color symmetry studies, multiple colors are used to represent different motifs which form a color symmetry pattern. Here, the motifs can be different chemical species, different orientations of a magnetic moment, or different crystals or domains of identical structure in polycrystalline materials. These different crystals or domains are arranged in space through some relative orientations and/or translations. Color symmetries arise from two situations in which geometric operations are brought into the system. In the first, the geometric operations are inherited from a higher symmetry structure before the symmetries are broken through a phase transition. In the second, the geometric operations are imposed into the system from the outside environment, such as constrained heteroepitaxy.

Kalonji and Cahn in 1997 discussed a 12- fold symmetry diffraction pattern of Al epitaxial thin-film given by Uli Dahman. This Al thin-film sample was grown epitaxially on Si(111) with three equivalent Al grains misorientated with each other by 120 degrees on the (100) plane of Al. After the substrate was etched, they achieved the diffraction pattern by putting the diffraction beam parallel to the [100] direction of Al of each domain and the [111] direction of the silicon substrate. This process gave a 12-fold symmetry diffraction pattern. It offers an example of an epitaxial thin-film system that has color symmetry imposed though external constraints. Similar combined diffraction patterns arise from other physical phenomena, such as symmetry-breaking solid-state phase transitions. In all cases, the number of colors is equal to the number of equivalent domains, and the classical subgroups are all crystallographic. However, as Kalonji and Cahn pointed out, crystallinity is not restricted on the group of the composite object, as proven by their 12-fold symmetry thin-film system example.

Although color groups have not been widely used in materials science research to date, after Bendersky and Cahn's study, the application of color groups in crystallographic studies increased. In recent decades, color groups have been used in

grain boundary studies, trijunction studies [49, 50, 51], antiphase domain boundaries studies, and quasiperiodic crystal studies. [52]

2.3.2 Several Concepts of Color Groups Used in This Study

In the following subsections, I will introduce several concepts of color groups used in this study. I will start by introducing the structure of color groups, and then explain an important concept: symmetry dictated extrema (SDE). Dichromatic pattern (DCP) and 2-color groups are used to study the symmetry of grain boundary systems, therefore, a detailed introduction of DCP and 2-color groups follows.

Dichromatic patterns and 2-color Groups

The first step to study the symmetry of a grain boundary is to derive the symmetry group of the dichromatic pattern (DCP), an imaginary construct composed of two infinite crystals, interpenetrated. It exhibits the relative misorientation and translation between the two grains that will characterize the eventual bicrystal. The symmetry groups that are appropriate for describing the symmetry of the DCP are the 2-color groups, also called Shubnikov groups. They contain two kinds of operations: classical ones that leave both of the component objects unchanged (red crystal to red crystal, and green to green); and the colored operations that bring the red crystal to green, and green to red. In the 2-D example shown in Figure 2.4, the classical operations include the 4-fold rotation operations, left handed and right handed denoted by C_{4+}, C_{4-}, 2-fold rotation operation denoted by C_2, and the identity, I. The colored operations include two kinds of mirror planes, indicated by solid lines in Figure 2.4 as m_1, m_2, m_3, m_4. So the symmetry group for this DCP is $G_{dcp} = 4m'm'(4)$. Here, the prime on a particular symmetry element indicates that the symmetry operation is colored, and the group within the parentheses is the classical subgroup of the group of the DCP.

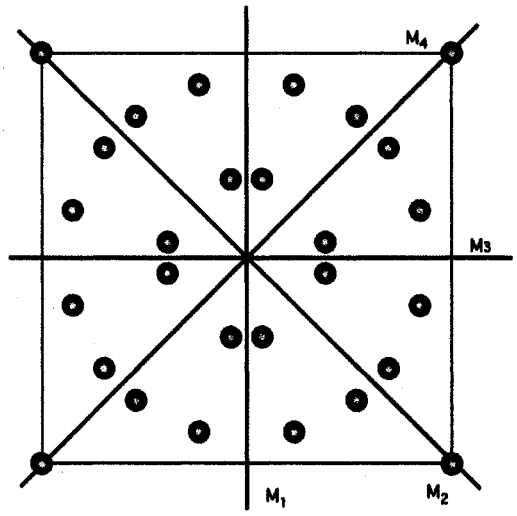

Figure 2.4: Sample of DCP of color symmetry

Structure of Color Groups

In addition to classical symmetry operations, color groups include special permutations, denoted by p_{ij}, which switch color i and color j of objects in color symmetry patterns. The operations that combine classical symmetry operations and color permutations are defined as color symmetry operations. Here, I will introduce several important subgroups of color groups by defining their color symmetry operations. G is the group containing all the operations that leave the multichromatic pattern invariant, with or without the changes of the color for each domains. The operations of the classical subgroup H are classical operations which leave the multichromatic pattern invariant without the change of the color for each domains. Operations in subgroup H can also be seen as the combination of the classical operation with the identity color permutation. H*, another subgroup of G, contains all the operations that leave at least one particular component object unchanged. Thus, H is a subgroup of H*, while H* is a subgroup of G. The index of G in H*, is, therefore, equal to the number of colors in the group, which are denoted as s. Each color group also has an

invariant subgroup of G, denoted as H. The index of G in H, which is equal to s!, indicates the number of the potential color permutations of s colors that can be found in the color group. For a 2-color group,

$$G = H + p_{12}H = H + H^* \tag{2.3.1}$$

here H is the classical subgroup of G of order n, and H* is the color subgroup of G of order n. G has order of 2n, and each of the H* group is a halving group of G. $|G/H^*| = s = 2$. $|G/H| = s! = 2$, which is consistent with two color permutations in the 2-color group. [53]

Symmetry Dictated Extrema

One of the primary applications of interfacial symmetry arguments is to locate values of the geometric parameters that by symmetry must yield extrema in grain boundary properties. These conditions are called symmetry-dictated extrema (SDE). [6] The locations of SDE depend only on symmetry and not on the details of interatomic interactions. Although we will not know whether the SDE are minima, maxima, or

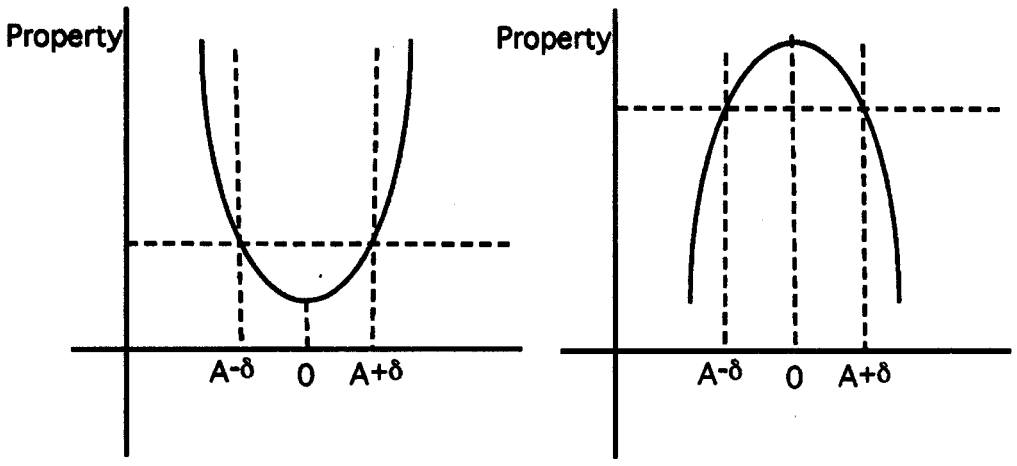

Figure 2.5: Possible property versus geometric parameter plot: example for the SDE

saddle points from the symmetry arguments, SDEs serve as powerful starting points for atomistic computer simulation and experimental studies.

Now I will explain SDE by giving an example. For a given system, chose a group of the geometric parameters, called state A, vary one of the geometric parameters to $+\delta$ to get state $A^{+\delta}$and vary the same parameter to $-\delta$ to get state $A^{-\delta}$. If for any δ value, $A^{+\delta}$ and $A^{-\delta}$ are equivalent by some symmetry operation, for an example mirror plane, there must be a local extrema existing at state A. Then, state A is an SDE with respect to that geometric parameter. If we fix all the other geometric parameters of the system, and only leave this particular geometric parameter free to vary, the location of the SDE with minimum energy with respect to this parameter will decide which constrained equilibrium state the system will evolve to after relaxation, and this equilibrium state only depends on the values of the other fixed parameters.

Idealized Construction of Cyrstalline Interfaces

We use a six-step method to construct a bicrystalline interface. First, we interpenetrate two identical crystals in the same coordination system. Second, we use different colors, such as green and red, to label these two crystals to achieve a DCP. Third, we choose the rotation axis and rotate one of the crystals around it. The rotation requires change in three geometric parameters of one crystal. Fourth, we make a rigid-body translation of one crystal, which also involves three geometric parameters. Fifth, we choose a planar surface in this DCP as the grain boundary plane. Here, another three parameters are required to specify the location of the planer interface: two for the orientation of the interface normal and one for the position of the surface along the normal direction. Finally, we discard the "wrong color" particles at each side of the plane, so one side of the plane only has red particles, and the other side only has green ones. The result is an idealized crystalline interface specified by nine geometric parameters. Figure 2.6 gives a schematic drawing to illustrate these six steps.

2.3.3 Application of color groups in materials science

As we mentioned before, color groups have been used to study trijunctions, quasicrystals, and magnetic materials. In this section, I will introduce some color group uses in studying quasicrystals. After the first quasicrystal was discovered by Shechtman [54], several groups studied the symmetry of long-term orientational order. Long-term periodicity is not included in the structure of quasicrystals, so they name an operation to be a symmetry operation of a quasiperiodic crystal if applying it on one structure will produce another crystal containing same spatial distribution of bounded substructures of arbitrary size. Instead of calling two structures to be **invariant** after applying a classical symmetry operation, they call two structures to be **indistinguishable** after applying a symmetry operation of quasicrystals. Niizeki used 2-color groups to study icosahedral point symmetry [55] and octagonal, decagonal, dodecagonal, and pentagonal quasicrystal lattices [56] in 1990. Lifshitz also did several studies using color groups on quasicrystal symmetry after 1997. In his color symmetry study on quasiperiodic crystals in 1997 [52], he extended the idea of color symmetry to non-periodic structures. His method has applications ranging from anti-ferromagnetism in tetragonal crystals to lattice structures with multiple types of atoms. [57]

Few studies to date have used color groups to study the properties and mechanism of evolution of microstructure of polycrystalline systems, which is the main topic of our studies. In the following chapter, I will use color groups to explain the symmetry of grains in bicrystalline systems and the mechanisms of grain growth.

2.3.4 The Group of the Wulff Plot

To study the morphologies of crystals growing in crystalline environments, we used another powerful tool of symmetry, the group of the Wulff plot (W). W is a symmetry group of interfaces that are physically equivalent to each other. [58] For single crystals that growing in an isotropic medium, Wulff plot symmetry and the symmetry of the

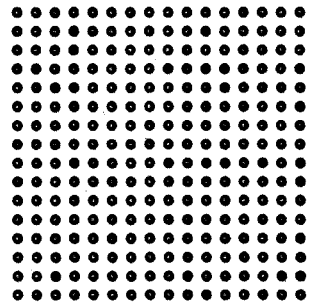

(a) Interpenetrate two

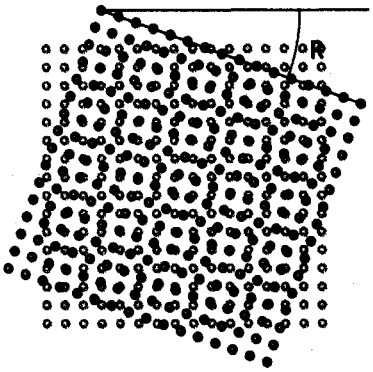

(b) Rotate one crystal

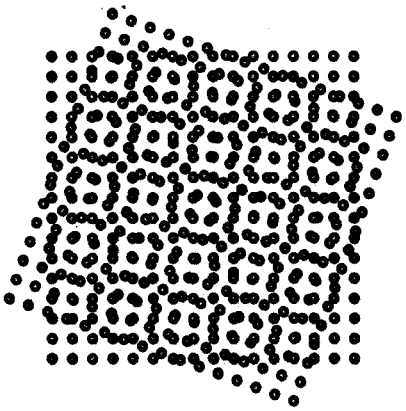

(c) Assign different colors to different crystals

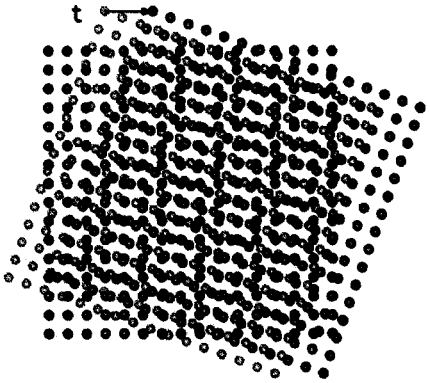

(d) Translate one crystal

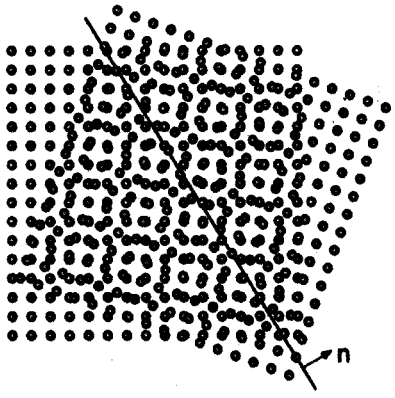

(e) Insert a planar plane

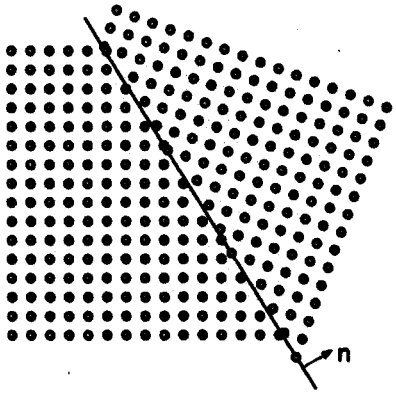

(f) Remove "wrong" color particles

Figure 2.6: Six stpes of constructing a crystalline interface.

resulting crystals will at least include the point group symmetry of the crystal, if not higher. For crystals growing in crystalline environment, such as a crystal growing in a bigger bulk crystal, the situation is more complicated. The group of the Wulff plot will always include the classical group H of the color group of the multi-chromatic pattern, but in some cases, will also include additional symmetries. W is equal to the union of the classical group, H, with the color operations' coset $(G - H)$, combined with an inversion, $\bar{1}$:

$$W = H \cup (G - H)\bar{1} \tag{2.3.2}$$

Since the 1980's, the group of the Wulff plot has been used to study the morphology of the grains under symmetry constraints. Most researchers studied expitaxial materials. For example, in 1995, Eflimov et al. used the idea given in reference [58] to analyze three heteoepitaxial systems, A_3B_5 nitride on sapphire, silicon on sapphire, and A_3B_5 on spinel. After comparison, they concluded that the results of the theoretical analysis were generally consistent with experimental data [59]. Kalonji and Cahn [60] used the group of the Wulff plot in their stacking-fault tetrahedron study, relating the shift of the crystal along $1/4\langle 111\rangle 111$ to the enclosing matrix. Carter and Handwerker gave a detailed illustration on the uses of the group of the Wulff plot to study the morphology of anisotropic interfaces and grain boundaries in ceramic materials. They introduced the group of the Wulff plot in discussing other symmetry-dictated low-energy interfaces in systems that include color symmetry. [61] The group of the Wulff plot has also been used to study precipitate morphology. Hugo and Muddle conducted an experimental and symmetry study in 1990 of the morphology of precipitates in an Al-Ge alloy. [62, 63] Dahmen in 1994 gave TEM photos of Ge precipitate morphology in Al for equilibrium single crystals with symmetry predicted morphologies. [64] Recently, Jiao, Aindow, and Pond [65] used the group of the Wulff plot to study precipitate orientation relationships and interfacial structures in a steel Zeron-100 system.

2.4 *Molecular Dynamics Simulation*

The molecular dynamics (MD) simulation method has been widely used since the 1980s to study the properties of materials with a critical characteristic size in nanometer scale. It computes the motions of individual particles in models of solids, liquids, and gases in describing how the positions, velocities, and orientations of particles change with time, based on the numerical integration of the classical Newton's equations.

Newton's 2^{nd} law gave the equation of motion:

$$F = ma \tag{2.4.1}$$

$$\frac{d^2x}{dt^2} = \frac{F}{m} \tag{2.4.2}$$

For N particles in three dimensions we have the differential of momentum per unit time equal to force acting on the particle or equal to the minor partial differential of the potential of position:

$$\frac{dp_i}{dt} = F_i\left(r_1, ..., r_{3N}\right) = -\frac{\partial U\left(r_1, ..., r_{3N}\right)}{\partial r_1} \tag{2.4.3}$$

$$\frac{dr_i}{dt} = \frac{p_i}{m_i} \tag{2.4.4}$$

Here U is the potential energy of the system, $F_i(r_1, ..., r_{3N})$ is the force acting on particle i from all the other particles in the system, and p is the momentum. So, if the potential and the starting status of a system is known, we should be able to integrate these equations forward or backward in time and thus determine the evolution of a molecular system through time. Several important aspects of the molecular dynamics technique will be introduced in the following sections.

2.4.1 MD algorithm

The positions of particles as a function of time can be written in starting positions, acceleration, and time in following equations 2.4.5

$$\begin{aligned} r(t) &= r(0) + v(0)t + \tfrac{1}{2}at^2 \\ v(t) &= v(0) + at \end{aligned} \tag{2.4.5}$$

Here, $r(t)$ is the position of the particle at t, and $r(0)$ is the position of the particle at t equal to 0, and a is the acceleration; $v(t)$ and $v(0)$ are the velocities of the particle at time equal to t and time equal to 0.

Given the starting positions of all the particles, the potential function for the system and the algorithm for the iteration, we can study the evolution of the system. The MD algorithm used in this study is the Verlet leapfrog method. It is one of the earliest and most popular numerical integration methods to date. [65, 66] The code listed below gives a simple "leapfrog" algorithm:

First, we need to set the position of all the particles at the beginning of the simulation at time equal to 0: $r_i(t_0)$, and all the velocities of particles at time equal to $t_0 + \delta t/2$ (halfway velocity): $v_i(t_0 + \Delta t/2)$

for $t = t_0 \rightarrow t_{0+\delta t}\{$

repeat for $i = 1 \rightarrow 3N\{$

using halfway velocity to calculate the next position of the particle

$r_i(t + \Delta t) = r_i(t) + v_i(t + \Delta t/2)\Delta t$

$\}$

calculate $F_i(\Delta t)$

for $i = 1 \rightarrow 3N\{$

the next halfway velocity is calculated using the force at $(t_0 + \Delta t)$

$v_i(t + 3\Delta t/2) = v_i(t + \Delta t/2) + (F_i(t + \Delta t)/m_i)\Delta t$

$\}$

$t = t + \Delta t \quad \}$

The Verlet algorithm is relatively fast and therefore used most widely because it only requires one evaluation of forces per timestep. However, other integration algorithms used to date include the general predictor-corrector algorithms and Gear's predictor-corrector algorithms, to name a few. [67] Other algorithms are used in constrained systems. For example, the SHAKE method is used for large molecules with internal degrees of freedom, such as bond constraints. [68] Fincham's implicit quaternion algorithm (FIQA) for rigid molecular species is used by a few researchers. [69] Several algorithms have been developed in the form of Verlet leapfrog or SHAKE integration algorithm with constant temperature and/or constant pressure, such as Berendsen's constant T algorithm with Verlet or RD-SHAKE [70] and Hoover's constant T algorithm with Verlet or RD-SHAKE. [71]

For most kinds of MD integration algorithms, the essential step of getting an accurate simulation is to choose an appropriate timestep Δt. To reduce the overall number of MD iterations, it is desirable to choose a timestep Δt as large as possible without sacrificing the accuracy and robustness. However, this does not mean that our simulation results will be more accurate if we keep Δt as small as possible. This is because two types of errors are associated with the choice of Δt: truncation error and round-off error. Truncation error refers to the accuracy with which a finite difference method is used to approximate the true solution to a differential equation. If our finite-difference equation is written in a Taylor series form, truncation error depends on the first nonzero term that has been omitted from the series. The Taylor series is

$$x(t+\delta t) = x(t) + \frac{dx(t)}{dt}\delta t + \frac{1}{2}\frac{d^2x(t)}{dt^2}\delta t^2 + \frac{1}{3!}\frac{d^3x(t)}{dt^3}\delta t^3 + ... \tag{2.4.6}$$

If we truncate at the nth term, the truncation error equal to the $n+1$ term of the Taylor series. and it will be:

$$te = \frac{1}{n!}\frac{d^{n+1}x(t)}{dt^{n+1}}\delta t^{n+1} \tag{2.4.7}$$

From equation 2.4.7 we can tell that the truncation error will increase with the increase of Δt. In contrast, round-off error is caused by the limitation on the storage

size for each data point. It includes all errors that result from the implementation of the finite-difference algorithm. For example, round-off error is affected by the number of calculations performed for each stage of the system; in other words, it will increase with the number of iterations in the same wall-clock time duration. Thus, round-off error will decrease with the increase of Δt. At some point, decreasing Δt, which will increase the iteration numbers in the same wall-clock duration, does not produce more accurate results. Ideally, we want to choose the value of Δt having the smallest total error. However, it is not practical to use this value: too much computer time would be required for a simulation. Consequently we used some value of Δt larger than that for minimum total error and determined its value empirically in test calculations, through an energy conservation test. [67]

To perform our MD simulations at constant temperature, we used a velocity re-scaling method to maintain system temperature. In this method, we set a thermal constant which is 0.3 ps in most of our simulations. For every thermal constant step, we compare system temperature with the chosen constant temperature. If the current temperature is higher than the constant temperature, we ratio the velocity of the particles so that the difference between the temperature after re-scaling and the constant temperature is half of the difference between system temperature and the constant temperature before re-scaling.

2.4.2 Boundary Conditions

All MD simulations require certain boundary conditions to reduce the size effect of surface interaction (interactions of the atoms with the container walls). Even for a system with millions of particles, the percentage of particles that are near the surface can be as high as about 6%. To eliminate the surface effects, periodic boundary conditions are used in most MD simulations. This means that we consider our N particle system to be surrounded on all sides by exactly identical N particle systems. A given particle in our primary cell interacts with the particles in the primary box plus

the particles in the neighboring image cells. However, periodic boundary conditions still require us to consider the new interactions of the particles in the cell with the replicas of these particles in the images of the cell. In the case of long-range potentials, such as electrostatic forces, these complications can be significant. Later, we will discuss the constraints required for periodic boundary conditions in our simulation structure to fit the periodicity of crystalline materials.

2.4.3 Potentials

The potential functions ϕ used in molecular dynamics simulation are mostly empirical and based on physically grounded assumptions. If, mathematically, we consider the system's energy to be a sum of pair-wise interactions between atoms, the potential we use is a pair function. In this study we used the Lennard-Jones potential, one of the pair potentials which was originally developed to model interactions between noble gas atoms. Although it is a relatively simple potential, and the simplest among all pair potentials, researchers also find that in simple structures, the simulation results obtained with this potential are reliable and show no significant differences with the simulation results done using more complicated potentials, especially in studying the properties of grain boundaries. [2]

For pair potentials, ϕ is the sum over pairwise interactions between all the particles. However, since this approach involves looping over all particles in the simulation, including all the "image particles" in the surrounding cells, the computational cost will be huge. Besides, since the Lennard-Jones potential is a short-range interaction, calculating all the pairs of particles in the system is not necessary. A truncation of the force interaction range is introduced in MD simulation for increasing the computational efficiency. [66] With the truncation method, the interaction between particles will not be calculated if the distance between two particles is over the truncation range, *rcut*. Most researchers shifted and truncated their Lennard Jones potential as

follows:

$$V_{L-J}(r_{ij}) = \begin{cases} \phi(r_{ij}) - \phi(r_c) & (r_{ij} < r_c) \\ 0 & (r_{ij} > r_c) \end{cases} \tag{2.4.8}$$

where

$$\phi(r_{ij}) = 4\epsilon \left[\left(\frac{\sigma}{r_{ij}} \right)^{12} - \left(\frac{\sigma}{r_{ij}} \right)^{6} \right] \tag{2.4.9}$$

Here σ and ϵ are the length and energy parameters, r_{ij} is the pair separation distance and the r_c is the potential cut-off distances. The common value chosen for r_c is usually 2.5 times σ. However, with this cut-off and shift method, at the cut-off range the force function is no longer a continuous function and is not very reliable.

We used a different truncation method in this study. Instead of choosing one cut-off distance and shifting the whole function, we choose two values for the cut-off range: inner cut off parameter (r_{ic}) and the outer cut off (r_{oc}) parameter. The potential used is modified as follows:

$$V_{L-J}(r_{ij}) = \begin{cases} \phi(r_{ij}) & (r_{ij} < r_{ic}) \\ \psi(r_{ij}) & (r_{ic} < r_{ij} < r_{oc}) \\ 0 & (r_{ij} > r_{oc}) \end{cases} \tag{2.4.10}$$

where $\psi(r_{ij})$ is a fit function equal to $\phi(r_{ij})$ when $r_{ij} = r_{ic}$; equal to 0 when $r_{ij} = r_{oc}$; in between, it ramps the function smoothly to zero. This function will give more accurate potential for short-range interactions and allow us to use a smaller cut-off range.

2.4.4 Energy Minimization Method

We used the energy minimization method at the beginning of the simulations to relax the system and achieve a suitable arrangement for the starting simulation structure. The energy minimization process eliminates thermally induced disorder by finding the particles closest local energy minimum position and helps elucidate a stable local

minimum energy structure. We used the method called conjugate gradient minimizer (CGM) in our studies. [72]

In stead of finding the global energy minimum, the energy minimization algorithms identify a local energy minimum of the potential at each iteration. The simplest approach to the 3D energy minimization is the steepest descent method. It computes the gradient at the point. Then the particle is pushed along the direction of the gradient. This process is repeated from the new point along the new gradient, which is always perpendicular to the old gradient. However, the steepest decent method will not be feasible for higher dimensional functions, especially for the problem in long narrow valleys that occur when one degree of freedom has much higher curvature than others. With the steepest descent method, the particle will cross and re-cross the valley many times. To solve this problem, conjugate gradient minimization was developed. It seeks a set of N conjugate directions along which to perform minimizations, where N is the dimensionality of the space. Minimizations along conjugate directions are non-interfering, which means that the gradients in the direction of previous minimization remain zero. With this algorithm, the particles in the system can get close to the local minimum in a small number of iteration steps.

2.4.5 Visualization

Atomic modeling involves many discrete degrees of freedom: the position of atoms. Therefore, how to visualize the simulation results becomes a critical part of atomistic modeling. Traditional scientific visualization methods, such as graphing and charting are still important in illustrating the simulation results. However, with the increase in the MD simulation scales, the raw data generated through MD simulation is enormous. Without an efficient visualization method, it is impossible to get useful information and locate the critical sites for special phenomena. The new kinds of visualization, such as snapshots, movies, and iterative navigation, greatly complement the traditional methods. For crystalline materials, the long range and short range orders

of particles are important. It is an essential task of visualization to use right light or color to identify and quantify these orders. However, the chosen atomic visualization method should vary with the purpose of the research. For a grain boundary MD simulation study, the visualization method could be specified as having two aspects: how to map out the particles in the system with time and how to color the particles to let the grain boundaries and other defects stand out from the ordered structure. In our research, it is critical to use different colors to represent grains with different orientations.

2.4.6 Structure

Two main methods to develop a starting structure for nano-crystalline materials in MD studies are the growing method and static define method. The most common growing method is to synthesize microstructures by MD simulation of a super-cooled melt. [73] In the study of Phillpot et al. [73], two small, pre-oriented crystalline seeds were inserted into the melt followed by a cooling processor below the melting point, with external pressure to initiate crystal growth. The schematic of the 3D periodic simulation cell for the synthesis of the bicrystal is shown in Figure 2.7. The final

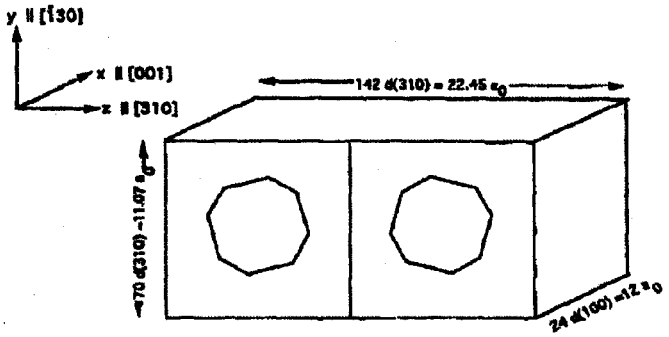

Figure 2.7: Schematic of the 3D periodic simulation cell for the synthesis of the bicrystal, indicating the crystallographic orientation of the seeds and the dimensions of the simulation cell.

atomic structure after synthesis is shown in Figure 2.8. The boundary was identified by the atomic miscoordinations. Solid lines enclose atomic structure originally in the crystalline seeds.

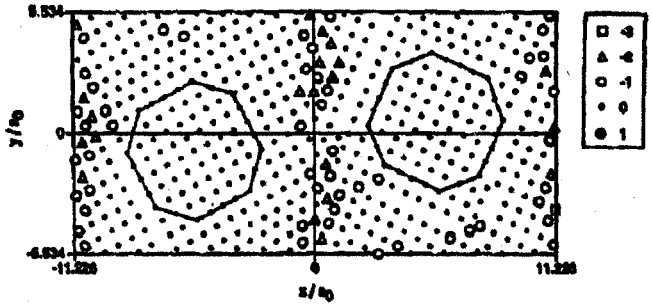

Figure 2.8: Position and nearest neighbor miscoordinations of atoms in a slice of thickness 0.5 a_o centered about x=0 in the MD-grown bicrystal.

This method allows suitable synthesis conditions (temperature, pressure, size, and shape of the crystalline seed) for identifying crystal growth, and has been used in many syntheses of polycrystalline structures. However, since the seeds are relatively small, the orientation of each grain can not be perfectly assigned. Consequently, this method is more feasible for studying twin boundaries and other low energy boundaries, but not general high angle grain boundaires.

Another growing method used for thin-film MD studies sequentially deposits the atoms of the upper level from a fixed height. During the deposition, no interactions between the newly introduced atom and substrate atoms were allowed through assigning the initial distance between the new atom and substrate or previously dropped atoms to be greater than the cut-off range. This structure was used in many studies of different phase interfaces or studies of thin-films. [45]

The static defining method scripts each particle's position one by one, and uses different methods to get rid of extra strain and stress at the interfaces caused by overlapping of the particles. Using this method, we can define the size of each grain

and the location and morphology of the grain boundaries. We can study the evolution of the grain boundary and grain morphology at constant temperature or constant pressure. Haslam et al. [39] made a columnar microstructure using this method as shown in Figure 2.9. With this inequilibrated starting structure, they observed grain

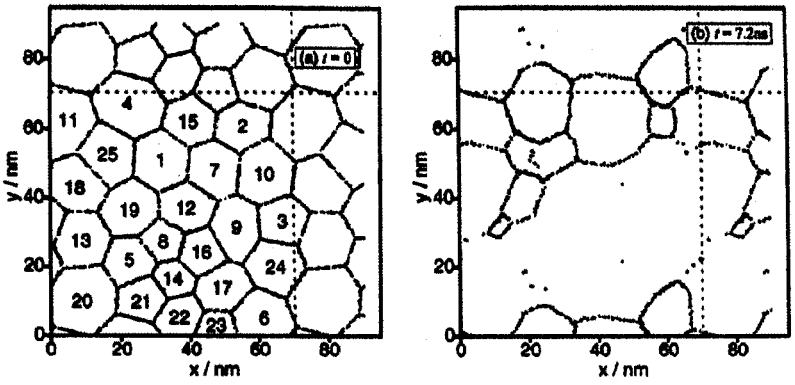

Figure 2.9: (a) The initial microstructure with 25 grains with a grain diameter of 15 nm is clearly delineated by the miscoordinated atoms. (b) The structure after simulation for 7.2 ns.

shrinkage and grain rotation.

The Voronoi construction is another commonly used static defining construction method. [74] However, the structure generated with this method will include more defects besides grain boundaries and relatively more complicated structures. With the orientation of grains generated randomly, it is not feasible to study the rotation of the grains and properties of particular grain boundaries.

In most of the static defining construction methods of polycrystalline materials, it is possible that two particles from different grains get too close to each other, sometime even overlapping each other, which causes unphyically large energies and forces to the system as the simulation starts. In some studies, [74], such particles are removed manually to prevent extra distortion.

To study the influence of one particular geometric parameter on the grain bound-

ary's properties and behavior, we used a columnar structure similar to the one used in the study of Haslam, et al. [39], with more constraints added to reduce the degrees of freedom. We will fully explain the structure of our system in Chapter 4.

Chapter 3

COLOR GROUP STUDY

3.1 Introduction and the dichromatic patterns of the systems

The main purpose of our study is to understand the mechanisms of grain growth and grain shrinkage, and how the geometric parameters will influence the properties and behavior of the system. Since the questions we are studying are quite general, we used a relatively simple material structure, face-centered-cubic (FCC), in our study to decrease the difficulty of MD simulation. Another advantage is that FCC is one of most common and important crystal structures in nature; hence, it is also one of the most studied structures, which gives us more chance to find experimental study comparisons.

We first studied color symmetry of the systems. We assumed there was an FCC crystalline thin-film grown epitaxially in the (110) plane on an body-centered-cubic (BCC) substrate on (100) plane. As many studies have shown, the symmetry of the substrate is imposed on the thin-film through atomic interactions, and therefore influences the morphologies and orientations of the grains of the thin-film. [75] 4-fold symmetry is imposed from the substrate, which gives two possible orientations of the FCC grains in the thin-film. One has its $[1\bar{1}0]$ direction parallel with the [001] direction of the BCC substrate, and its [001] direction parallel to the [010] direction of the BCC substrate. The second has its $[1\bar{1}0]$ parallel to the [010] direction of BCC substrate, and [001] parallel to the [001] of the BCC substrate. Both kinds of grains will exist and be misorientated with each other by 90 degrees about the [110] direction in the FCC (110) plane.

If we use different colors to represent different orientation of the grains, and extend

both kinds of structures in space, we will get the DCP of this system, as shown in Figure 3.1. Here, the different motifs of the DCP are different grains that misoriented

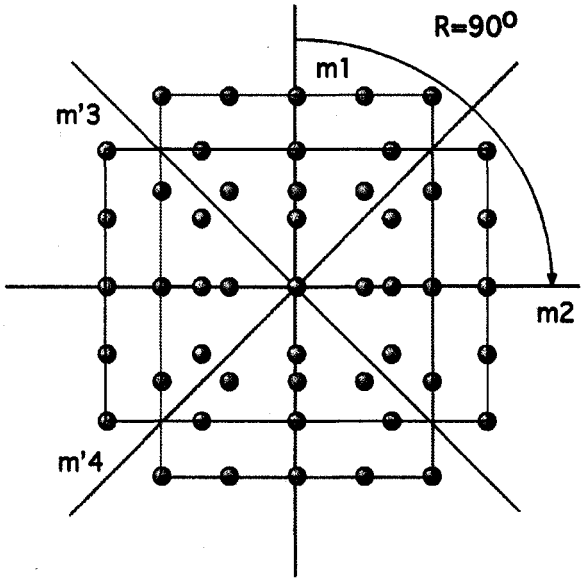

Figure 3.1: DCP of sample system 1 with two kinds of grain misorientated to each other by 90 degrees around the common [110] direction of both grains with mirror planes indicated by solid lines.

with each other by 90 degrees in the (110) plane. We use red and green to color the atoms belonging to different grains, and use R to indicate the misorientation between the two grains about the [110] direction in common (110) plane, assuming $R = 0^o$ means that no misorientation exists between two grains and R increases in a clockwise direction. For this DCP, $R = 90^o$. To compare this system to more general DCPs, we studied DCPs with different misorientations. For example, we studied a system with two grains misoriented with each other by 45 degrees. One grain's FCC $[1\bar{1}0]$ parallel to the [001] direction of BCC substrate and its [001] direction parallel to the [010] of the substrate; the other grain's FCC $[1\bar{1}0]$ is parallel to the [011] of the BCC substrate and its [001] is parallel to the $[0\bar{1}1]$ of the substrate. Using the same method, we achieved the DCP pattern with $R = 45^o$, as shown in Figure 3.2. These

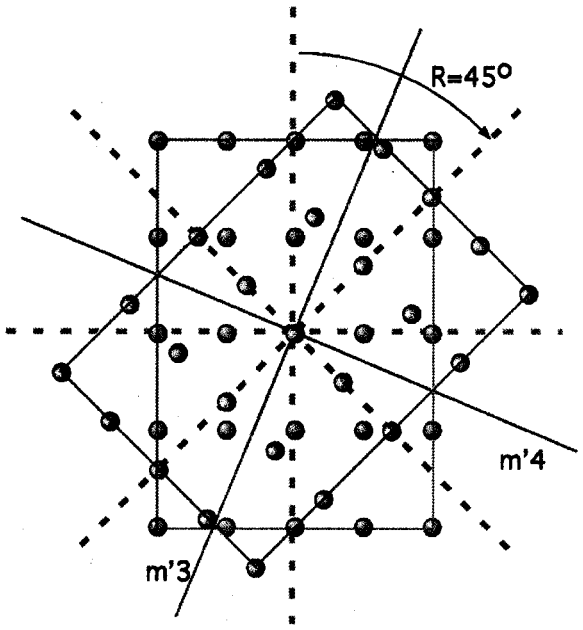

Figure 3.2: DCP of sample system 2 with two kinds of grain misorientated to each other by 45 degrees around [110] direction of both grains with mirror planes indicated by solid lines.

are the two main DCPs we studied. In the following sections, we will first discuss the color group study of these DCPs, and then the SDE for the misorientation and the SDE for orientation of grain boundary normal, $\hat{n}$, for these two DCPs.

3.2 Color group of the DCPs

Let's first illustrate the DCP with $R = 90°$, as shown in Figure 3.1. Assume that the green grain is in the original orientation, and the red grain is achieved by imposing a 90-degree rotation operation onto the original green grain. The classical symmetries of the FCC (110) structure that survive from the rotation operation that bring green particles to green particles and the red particles to red particles are: $\{I, C_2, C_2, C_2, \bar{I}, m_1, m_2, m\}$. Here the "I" is the identity symmetry, three "C_2"s indicate the 2-fold symmetries along the primary periodic directions of the FCC, $\bar{I}$ is the inversion symmetry, m_1 and m_2 are the mirror planes of the structure indicated by solid lines in Figure 3.1, and m is the mirror plane parallel to the (110) plane of both grains. According to the property of 2-color groups, the order of the classical symmetry group should be the same as the order of the color symmetry coset. Therefore, we should have exactly the same number of symmetries for the color symmetries. The colored symmetries that bring the red particles to the green particles and the green particles to red are: $\{C_{4'-}, C_{4'+}, m'_3, m'_4, C_{4'\bar{I}+}, C_{4'\bar{I}-}, C_{2'_{(x,x,0)}}, C_{2'_{(x,\bar{x},0)}}\}$. Here $C_{4'-}$ and $C_{4'+}$ are the 4-fold symmetries along the FCC [110] direction of both grains, right handed and left handed. m'_3 and m'_4 are the color-mirror planes indicated by solid lines in Figure 3.1; $C_{2'_{(x,\bar{x},0)}}$ and $C_{2'_{(x,x,0)}}$ are the 2-fold symmetries with their rotation axes in color-mirror planes, and perpendicular to the [110] direction of both structures. Combining the classical symmetries and the color symmetries of this DCP, produces the color group of this DCP, which is $G_{DCP} = 4'/mmm'(mmm)$.

We used the same method to create the DCP of the system with $R = 45°$. As shown in the Figure 3.2, the classical symmetries for this DCP that survive from this rotation operation are $\{I, C_2, \bar{I}, m\}$; here the I is the identity, C_2 is the 2-fold

symmetry around [110] direction for both grains, $\bar{I}$ is the inversion symmetry, and m is the mirror symmetry parallel to (110) plane. The color symmetries are $\{m_3', m_4', 2', 2'\}$; here m_3' and m_4' are two color-mirror planes indicated by solid lines in Figure 3.2 and two 2' represent the color 2-fold symmetries with their axes in the color-mirror planes and perpendicular to the [110] direction of both grains. Combining the classical symmetry and the color symmetries of this DCP, produces the color group of this DCP: $G_{DCP} = m'm'm(2/m)$. Since we are studying a FCC bicrystalline system with different R in the common (110) plane, we could extend this discussion to arbitrary values of R. We found that an arbitrary value of R will give results of color group identical to that of $R = 45^o$. No matter how many degrees we chose for R, the classical symmetries $\{I, C_2, \bar{I}, m\}$ will always survive from the rotation operation. This occurs because these symmetries were not in the (110) plane, so the rotation operation with the rotation axis in [110] direction for both grains will not change these symmetries. These color symmetries will include two color-mirror planes that are perpendicular to the (110) plane of both grains, and oriented $R/2$ away from the original orientations of the grains. For $R = 45^o$, it will located at 22.5^o and 112.5^o from the initial position for both grains. Two colored 2-fold symmetries will also be included after this rotation operation, with the 2-fold rotation axis in each of the color-mirror planes and perpendicular to the [110] direction. Therefore, no matter what value we chose R to be, the structure after a rotation in (110) plane will at least have color symmetries that include $\{m_3', m_4', C_{2'}, C_{2'}\}$; the color group of the DCP will be $G = m'm'm(2/m)$. This also shows that $R = 45^o$ is not a symmetry dictated extremum value with respect to R, and the color group of the FCC (110)//(110) DCP does not change with R except for $R = 90^o$.

3.3 Symmetry dictated extrema (SDE) study with respect to misorientation between the grains

We used SDE study to determine the geometric parameters that require the system to have extremum properties, such as the extrema of the energy. Although SDE study will not be able to give us further information as to whether it is an energy minimum, energy maximum, or saddle point, it will serve as a good starting point for further study, such as our MD simulations.

As explained in the introduction, in general, three geometric parameters are needed to specify the rotation between two grains: two for the normal direction of the rotation axis and one for the angle of the rotation about the rotation axis. However, to discover direct relationships between geometric parameters and the properties of the system, we reduced the degrees of freedom down to one by allowing only one geometric parameter to vary. In our systems, since all misorientations are around the axis that is parallel to the common [110] direction of the FCC bicrystalline structure, we assume that the rotation happens in the FCC (110) plane only. With this assumption, we simplify the our color symmetry study of misorientation to finding the SDE with respect to R, the misorientation in the FCC (110) plane of our two-grain system.

To know whether $R = 90^o$ is an SDE with respect to R, we need to compare two DCPs, one with $R = 90^o+\delta$ and the other with $R = 90^o-\delta$, as shown in Figure 3.3 For these two structures, the differences exist only in red grains: one rotated $R = 90^o + \delta$ and the other rotated $R = 90^o - \delta$. These two structures are mirror image of each other with mirror plane parallel to the (100) direction and $(1\bar{1}0)$ direction of the unrotated grain.

So adding a mirror operation on the structure a) will give us the structure b), which means the structure a) is identical with structure b). Since δ could be any value, the DCP with $R = 90^o$ is the SDE with respect to the misorientation on the

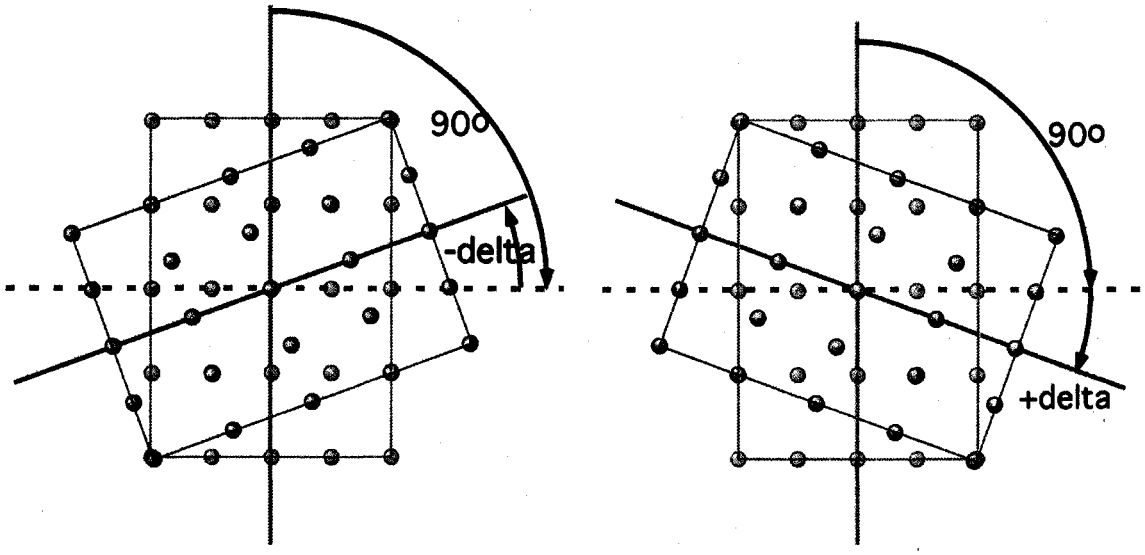

Figure 3.3: a) DCP with $R = 90^o - \delta$, b) DCP with $R = 90^o + \delta$.

FCC (110) plane. However, as shown in Figure 3.4, DCP with $R = 45^o - \delta$ is not identical to DCP with $R = 45^o + \delta$. Hence, the $R = 45^o$ is not an SDE with respect to misorientation.

3.4 SDE with respect to the orientation of grain boundary normal, $\hat{n}$

In an FCC bicrystal system, with a given misorientation, three other parameters are required to identify a grain boundary plane. To study the SDE with respect to the orientation of grain boundary normal, we fix two of the parameters and only give one degree of freedom to the orientation of grain boundary normal by letting all our grain boundaries be perpendicular to (110) plane of FCC. In other words, in our system, we assume all our grain boundaries are tilt grain boundaries of the $\langle 110 \rangle$ directions.

We first study the SDE with respect to the orientation of the $\langle 110 \rangle$ tilt grain boundaries normal with $R = 90°$. The DCP of the FCC with two grains misorientated with each other by 90 degrees in the common (110) plane is shown in Figure 3.5, defined as $R = 90^o$ in our study. Since all SDE are located at special symmetry

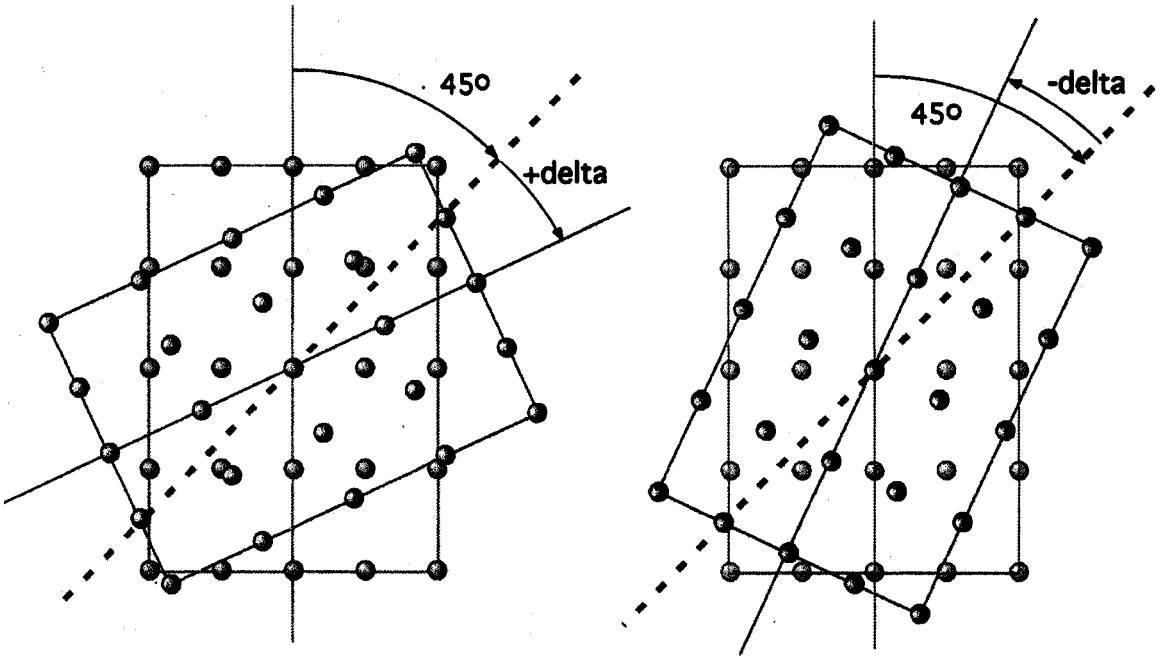

Figure 3.4: a) DCP with $R = 45^o - \delta$, b) DCP with $R = 45^o + \delta$

locations of the colored symmetry pattern, we will focus our study on the special grain boundary planes in the DCP. As we found in the color group study, this DCP has two kinds of special mirror planes: classical-mirror planes: m_1, m_2, m; and color-mirror planes: m_3', m_4'. Among these mirror planes, four have their normal directions perpendicular to $\langle 110 \rangle$ direction: m_1, m_2, m_3', m_4'. In Figure 3.5, which is a two-dimension illustration of the DCP seen from the $\langle 110 \rangle$ direction, these planes are shown with solid lines, with classical boundaries in black and color boundaries in blue.

By putting the grain boundaries on top of these special mirror planes in the DCP with $R = 90^o$, we studied SDE with respect to $\hat{n}$ of grain boundaries on top of the classical-mirror plane and color-mirror plane boundaries. The only geometric parameters that differ for all these grain boundaries are the angles between the normal directions of grain boundary planes in the common (110) plane; therefore, it is the only

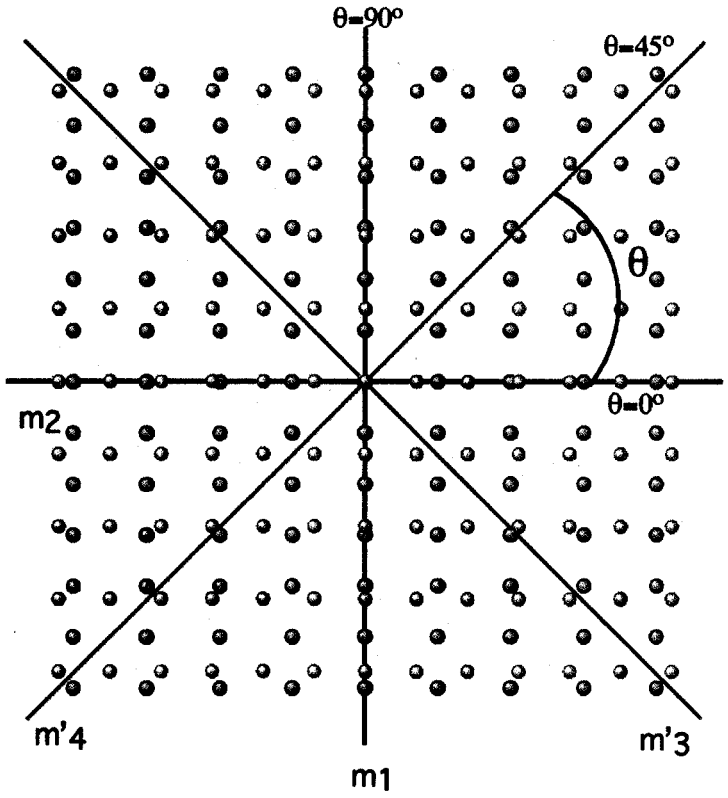

Figure 3.5: DCP with R=90. The classical-mirror plane boundaries are identified by black solid lines; the color-mirror plane boundaries are identified by blue solid lines.

parameter that is free to vary in our discussion. Let we use θ to identify this parameter by assuming $\theta = 0^o$ is located on top of the mirror plane m_2 and θ increases in anti-clockwise direction. So the grain boundaries on top of the classical-mirror planes have

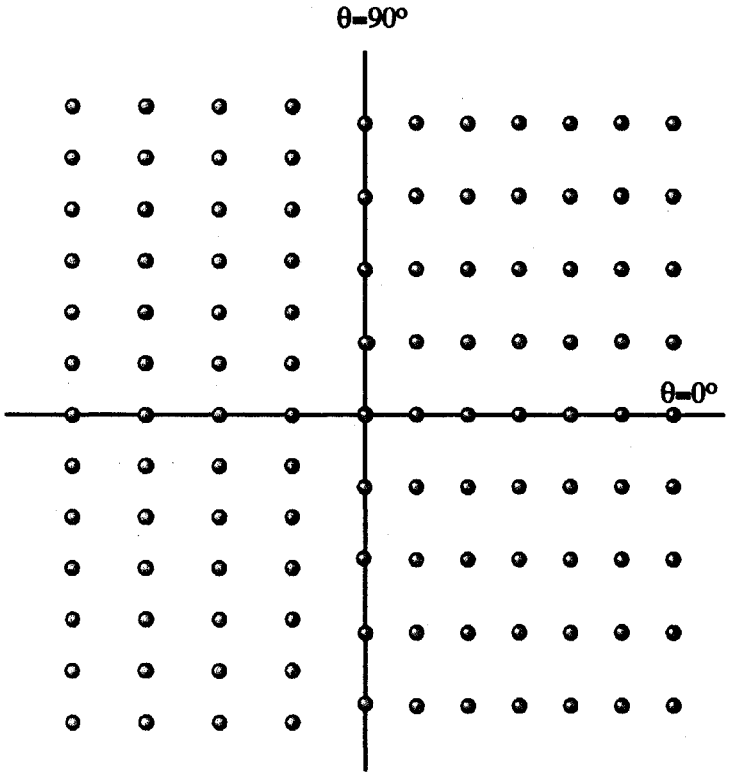

Figure 3.6: Classical mirror plane boundary: grain boundary on top of the classical-mirror plane with $\theta = 90^o$.

their θs equal to $0^o$and 90^o, shown in Figure 3.6; and the grain boundaries on top of the color-mirror planes have their θs equal to $\pm 45^o$, shown in Figure 3.7.

The SDE with respect to θ is studied by comparing the structures with $\theta = 90 + \delta$, and the structure with $\theta = 90 - \delta$ as shown in Figure 3.8. These two structures are related with each other through the mirror plane parallel to the $\langle 110 \rangle$ direction with $\theta = 90^o$. Thus, classical-mirror plane boundaries are SDE with respect to θ in (110) plane.

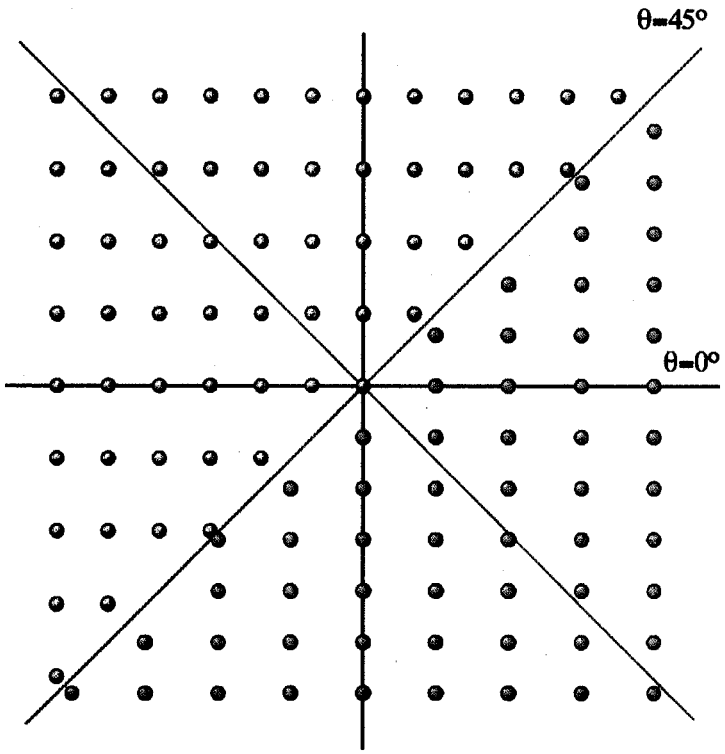

Figure 3.7: Color mirror plane boundary: grain boundary on top of the color-mirror plane with $\theta = 45°$.

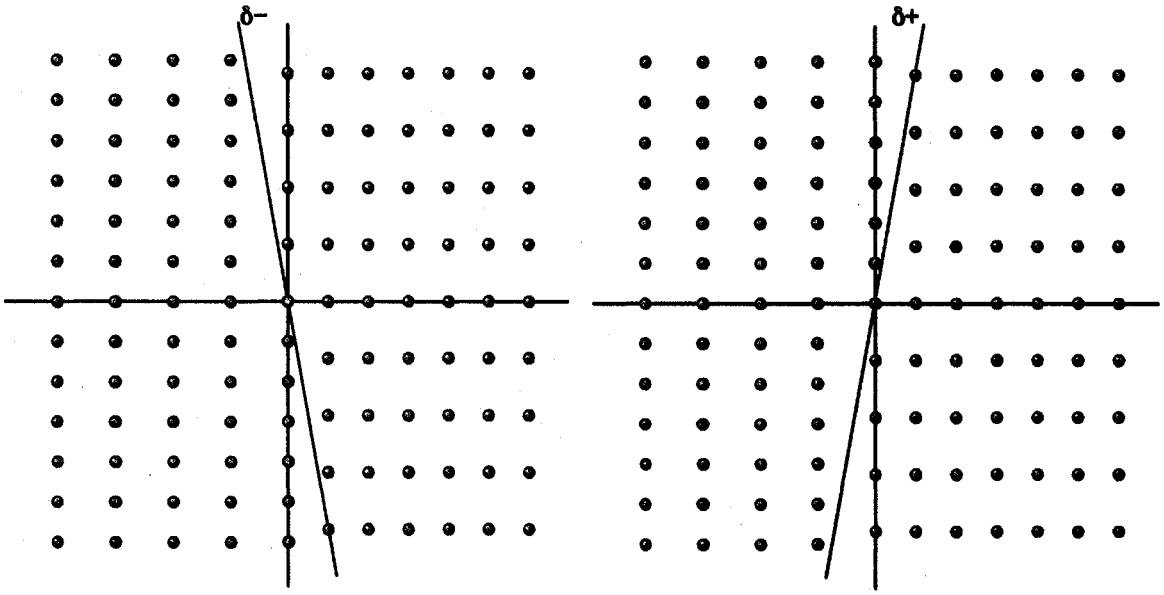

Figure 3.8: SDE study for $\theta = 90$, with a) $\theta = 90 + \delta$ and $\theta = 90 - \delta$.

Moreover, any grain boundary located on top of a mirror plane of the DCP is an SDE with respect to the location of the grain boundary in the plane that is perpendicular to the mirror plane. [6] Thus, the grain boundary on top of the color-mirror plane is also an SDE with respect to θ, as shown in Figure 3.9.

For the structure that is $R \neq 90$, no classical-mirror plane perpendicular to the (110) plane survives after rotation, and the SDE with respect to the grain boundary location is located at all of the color-mirror planes. Notice that none of these boundaries found by our SDE studies are coincident site lattice (CSL) boundaries.

3.5 Morphology studies using the group of Wulff plot

Using the group of the Wulff plot, we can study the possible morphologies of our sample systems at equilibrium. As we explained in Chapter 1, the group of the Wulff plot is given by equation 2.3.2.

In the DCP of the FCC bicrystalline system with misorientation in common (110)

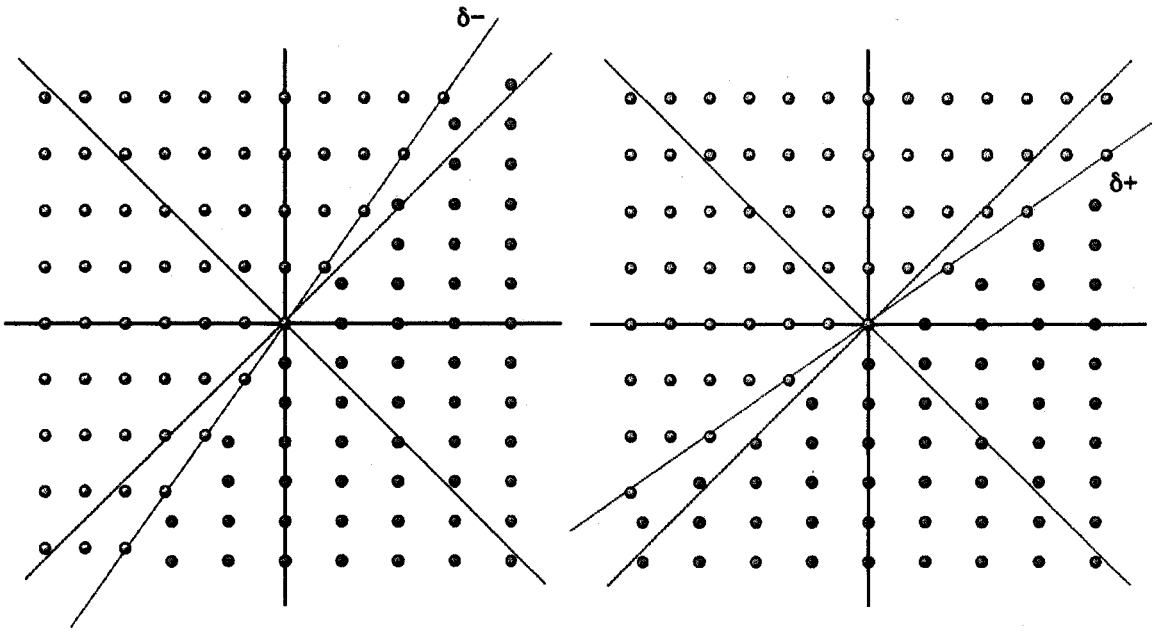

Figure 3.9: SDE study for $\theta = 45$, with a) $\theta = 45 + \delta$ and $\theta = 45 - \delta$

plane, since the inversion operation $\bar{1}$ is among the classical symmetry operations of the color group, and classical symmetry will not change the color coset, we will get the color symmetry coset itself if we operate the inversion $\bar{1}$ on the color symmetry coset:

$$\{G - H\}'\bar{1} = \{G - H\}' \tag{3.5.1}$$

So the equation 2.3.2 will become:

$$W = \{H\} \cup \{G - H\} = G \tag{3.5.2}$$

Thus, in the FCC (110)//(110) system, the group of the Wulff plot is the same as the color symmetry group of the DCP. The group of the Wulff plot of FCC bicrystalline system with $R = 90^o$ in FCC common (110) plane is $4/mmm$. Thus, the morphology of a crystal growing in this crystalline environment must include at least $4/mmm$

point symmetry in equilibrium. However, for the system with R equal to 45 degrees, or any arbitrary rotation that is not equal to 90 degrees, the group of Wulff plot will be mmm, and mmm symmetry should be included for the crystal growing in this condition in equilibrium.

In the following chapters, we will use all these analyses as the starting points for our molecular dynamics simulation studies.

Chapter 4

MOLECULAR DYNAMICS SIMULATION: SOFTWARE, SIMULATION STRUCTURE AND METHOD, AND VISUALIZATION ALGORITHM

4.1 Introduction to kSan

The molecular dynamics simulation tool used in this study is called kSan, a software package for the Macintosh originally developed by Dr. Olof Hellman. It bridges the gap between the home computer and experimental molecular dynamics simulations running on super-parallel-processing computers. kSan uses the graphical user interface (GUI) of MacOS to provide run-time visualization of simulations, so users can see the movements of the particles. Information about the particles, such as positions and directions of movement, can be displayed on a graphic window during simulation. Applescript, a scripting tool installed with MacOS, allows users to interact with kSan, such as taking snapshots for the graph window and generating movies by compiling these snapshots. The properties of the particles and the system can be observed directly through the data window, or can be recorded by scripts while movies are generated.

kSan has a plugin-friendly structure that enable users to easily develop their own plugins to add more features. kSan is still in development, and we are working on coding it to make it more powerful in studying polycrystalline systems. Several versions of kSan have been developed during the course of our research project. Features added to the earlier versions include a different colorizer method and more values of the properties of the particles in the data list. Some updates corrected mistakes in the earlier version. The main improvements we have made for kSan during this project

include shifting kSan from the OS9 to OS X operating system, adding constant temperature controlling, adding a new algorithm to calculate the miorientation of the grain a particle belongs to, and adding the new "**color by axis angle**" colorizer based on this algorithm. The following sections explain our new method of structuring the experiments that helped us to achieve more accurate results with a small simulation system, the new algorithm we developed for kSan, and some observations resulting from comparing different versions of kSan.

4.2 New algorithm for calculating the orientation value of the grain to which a particle belongs

4.2.1 Color particle by its energy

During our study, we found that although it is easy to visualize the particles in kSan, it is hard to identify the location and normal orientation of grain boundaries since the size and the color of the particles are same. The boundaries are a big portion of our relatively small system, so it is even harder to let the particles belonging to the grain boundaries stand out from the crystalized area in the graphic window. Hence, we developed functions to change the color of the particles with the properties of the particles. Particles at interfaces with different properties, such as potential energy, will have different colors than the particles inside grains. In this way, we will be able to specify the locations and the orientations of grain boundaries. We call these functions colorizers of kSan.

The first colorizer we developed is called "**color by energy**". It assigns a color according to the sum of kinetic energy and potential energy of the particle. By using this method, we will be able to distinguish the location of the grain boundary since the particles at boundaries almost always have higher energy, and therefore lighter color, than the particles in perfect crystal structures. Figure 4.1 shows that a cylinder-shaped boundary located at the center of the graphic window stands out because the color differs from the other part of the system.

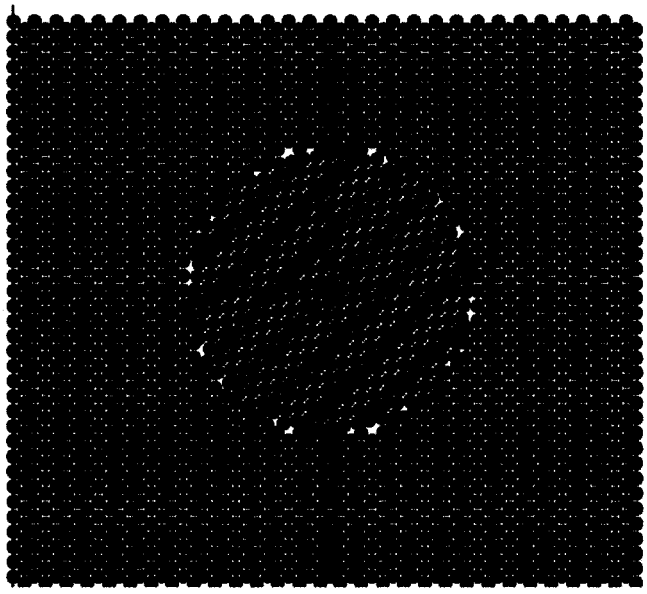

(a) before color by energy

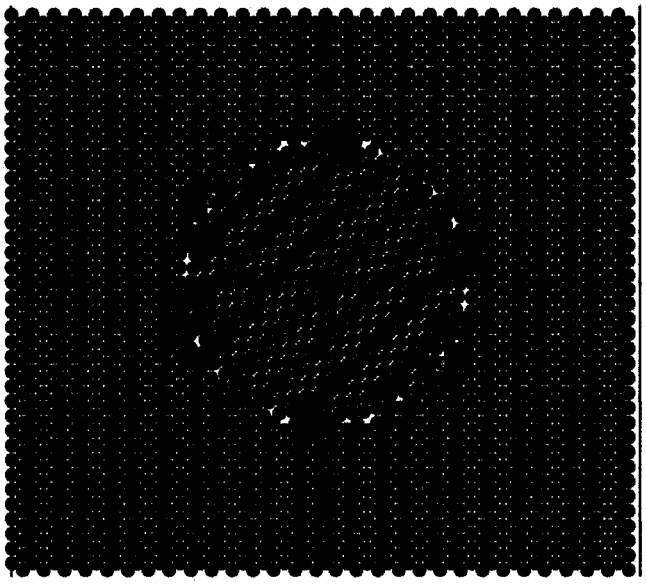

(b) after color by energy

Figure 4.1: Color particles according to the sum of the potential energy and kinetic energy of each particle

However, since we are studying the grain boundary, which is the boundary between crystals with exactly the same structure, the two grains in the system have exactly the same energy. As shown in the Figure 4.1, the particles in the embedded columnar-shaped grain and the ones in the outside grain have the same energy and thus the same color. Although the boundary is clear and easy to identify in Figure 4.1, after long-time system evolution at higher temperatures, the stress of the grain boundary will spread out into the whole system which usually makes it harder to distinguish the difference between the particles in the grain and the particles at the boundaries. Figure 4.2 is a snapshot taken at 800 degrees after 70000 simulation steps. It is difficult to study the interfacial properties with this colorizer method even though we can vaguely identify the location of the grain boundaries. We need a better colorizer for this research, especially at increased temperature.

Most of the simulations in our study include two grains, and the only difference between them is the orientation angles. Therefore, the best way to identify the location of the grain boundary is to color the particles with respect to the orientation of the grains to which the particles belong. Hence, we worked on a new algorithm that will calculate for each particle the relative position of its neighboring particles and give a value for its relative misorientation with respect to a reference direction. By using this algorithm, we will be able to color the particle according to the orientation of the grain it belongs to during the evolution of the system. Even if the particles belonging to one grain become part of another grain as the simulation progresses, this algorithm will make it possible to track the grain a particle belongs to. Moreover, since this algorithm assigns a quantitative value to each particle according to the orientation of the grain it belongs to, we will be able to track the change of the orientation of the grain during the evolution of the system by averaging the orientation values of each particle of the grain. In other words, we will be able to quantitatively track any rotation of the grain. The following section explains how this algorithm works.

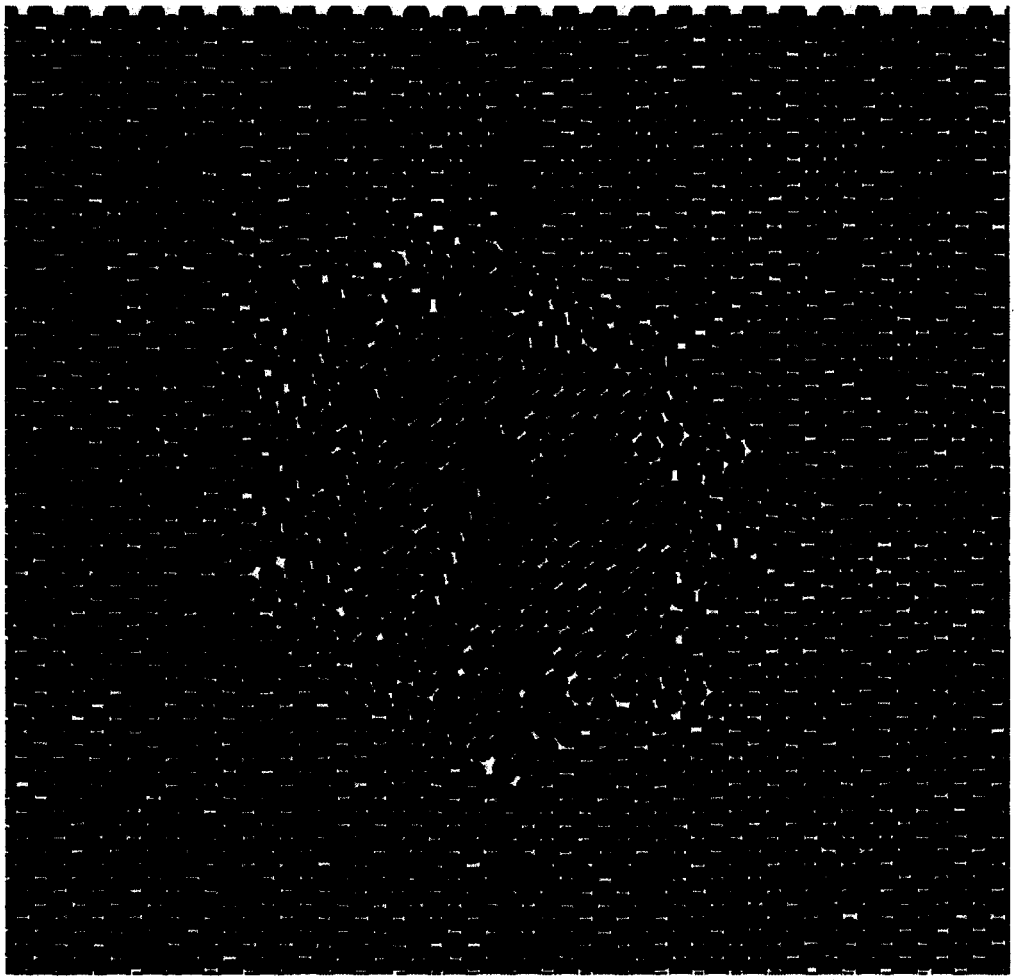

Figure 4.2: A snapshot taken around 70000 simulation steps at 800 degrees with one columnar-shaped grain embedded in another. R_o=35.26 degrees.

4.2.2 Algorithm of tracking particle's axis angle

For this new colorizer, the main goal is to quantify the arrangement of the particles around one certain particle and assign the orientation value to this particle. Such 3D problems require enormous calculation. However, in this research, we only studied problems in FCC (110) plane, which means the only difference between grains is their misorientation in FCC (110) plane. Therefore, this is a 2D problem with only one degree of freedom. We only need one variable to represent the orientation, which is also the rotation angle of the grain with the rotation axis in the FCC [110] direction. Figure 4.3 is a flow chart of that lists the main steps of this algorithm.

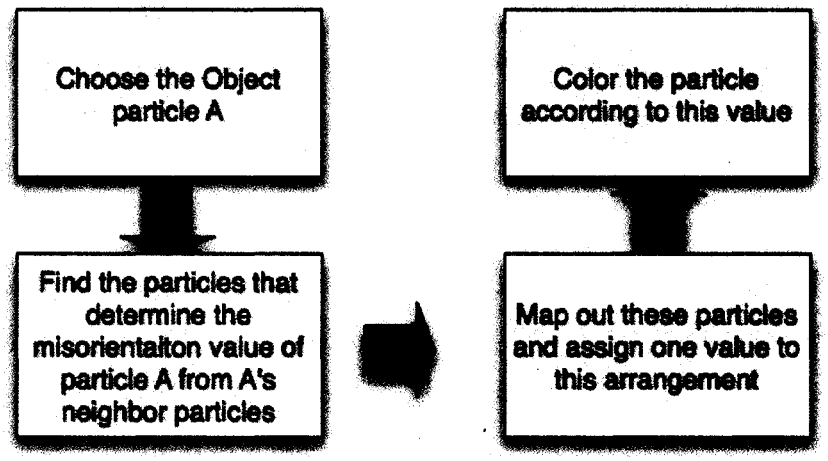

Figure 4.3: Flow chart of the new algorithm that assigns an angle value to each particle according to the orientation angle of the grain to which it belongs.

This algorithm includes a series of functions of one particular particle, since we are trying to characterize each particle. The first step is to chose an object particle. For convenience, we name it particle A. Second, we need a list of neighbor particles close to particle A. Third, we need to have the angle value of each neighbor particle to represent their relative positions to particle A. Fourth, we need a function to map

out these particles, and assign one value to represent the arrangement of particle A's surrounding particles. The last step is to assign the color property of particle A linearly according to this value.

The difficulty of this algorithm is to obtain the average value which represents the neighbor's orientation relation to the target particle. We need to have average value because we need to obtain the value during simulation with thermal effects. However, at high temperature, it is very likely that the neighbor particles do not locate at perfect lattice sites because of thermal effects. Thus, if we just simply average the angular values, we won't have a reliable angular value. Moreover, we cannot simply average the angular value by using their arithmetic means because that would not represent the symmetry of the system. In our study, we used a function called splat function to solve this problem. The following paragraph explains this algorithm in detail by first describing the geometry of the system.

Here, we still use FCC structure as an example. Figure 4.4 shows an FCC structure with the object particle colored red. We use the same color for particles that are the same distance to the object particle, and use a different color for particles with different distances from the object particle. In Figure 4.4, the blue particles are the first-nearest neighbors, the yellow ones are the second-nearest neighbors, the magenta ones are the third-nearest neighbors and the grey ones are the forth-nearest neighbors.

We redraw the FCC structure by putting the object particle in the center, and let the [110] direction of FCC be parallel to the Z direction of the coordination system of the graph, as shown in Figure 4.5. Here the blue plane is the (110) plane that passes through the object particle. Still, blue particles are the first-nearest neighbors, yellow ones are the second-nearest neighbors, magenta ones are the third-nearest neighbors and grey ones are the fourth-nearest neighbors.

The first function in this algorithm aims to obtain the list of the neighboring particles, including the particles that determine the misrientation of the grain to which particle A belongs. As we have explained earlier, since all rotation and difference of

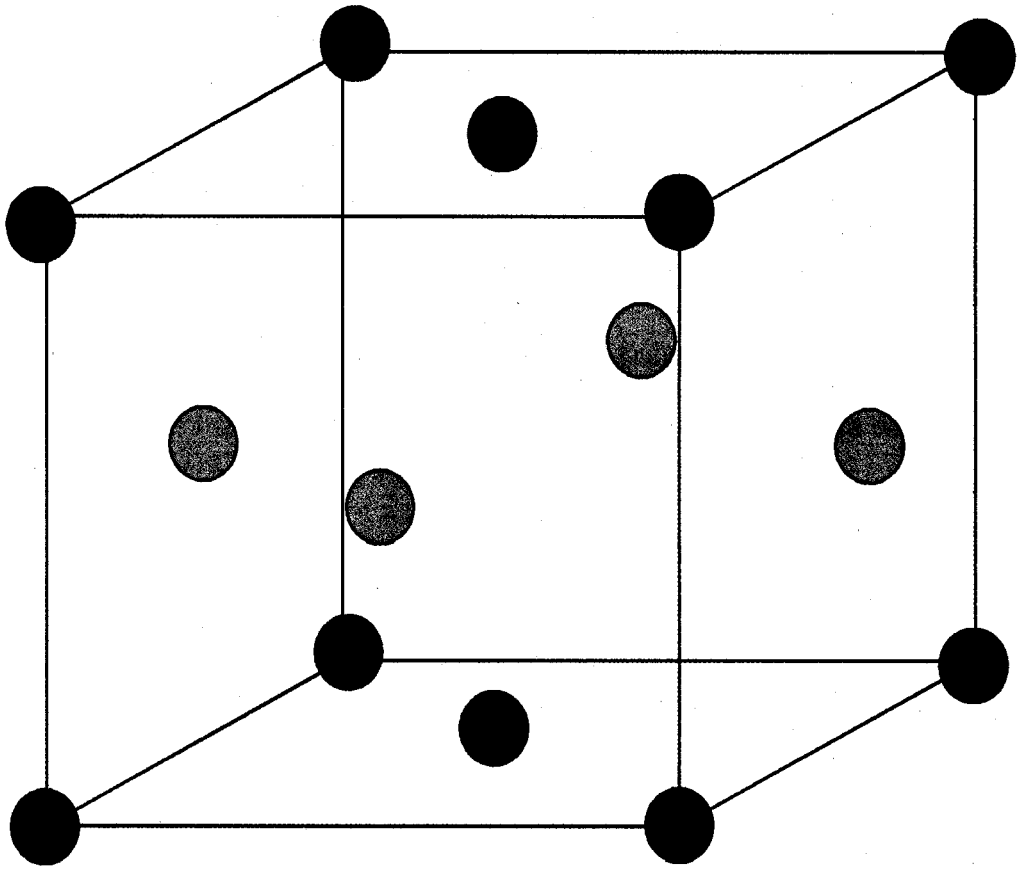

Figure 4.4: FCC structure, the red particle is the object particle, the other particles are colored according to their distance to the object particle.

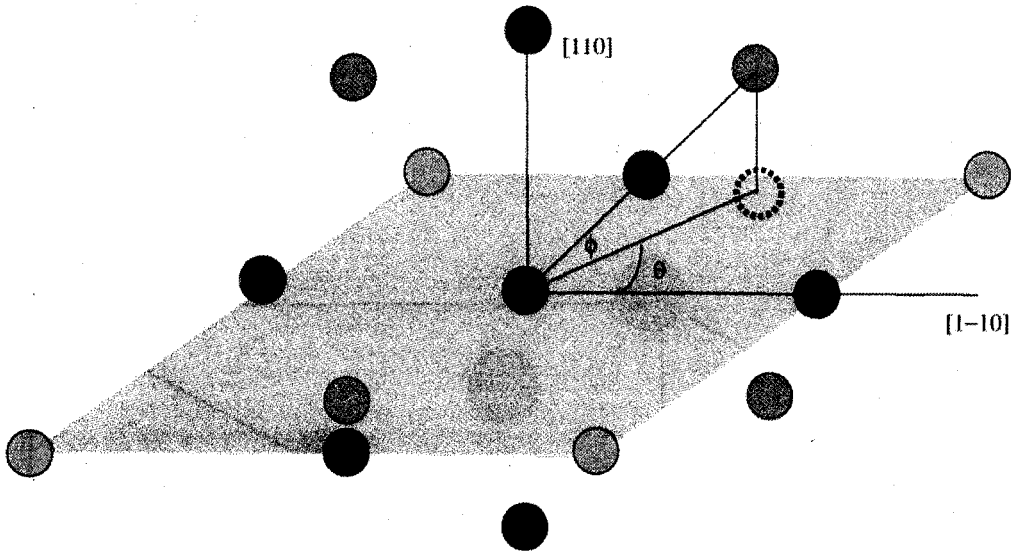

Figure 4.5: FCC structure, object particle is the red particle in the center; blue plane is the FCC (110) plane passes through the object particle. The other particles are colored in the same way shown in Figure 4.4.

orientation are inside the FCC (110) plane, this is a 2D problem in a 3D structure. Therefore, to simplify the problem and increase the calculation speed, we project all neighbor particles to the (110) plane that passes through particle A (the red particle), the blue plane in Figure 4.5. The projected particle is marked by the dashed line in Figure 4.5. We calculate the angle between the projected particle and the reference plane, which is marked by ϕ. We assign a weight value to the this particle according to the value of ϕ. In kSan, we compare ϕ with a value called **Acceptance Angle** with default value equal to 30 degrees. If ϕ is bigger than the acceptance angle, we set the **Weight of Angle from Plane** to 0; if ϕ is equal to 0, then we set the **Weight of Angle from Plane** to 1; and in between 0 to the **Acceptance Angle**, we will fit the weight value of the **Weight of Angle from Plane** in a linear function which equals to ϕ/"**Acceptance Angle**". Then we compare the distance between the projected particle and the object particle. In Figure 4.5, the distance is marked as a. Nevertheless, we assign a weight value to the particle according to the value of

a, which is called **Separation Weight** in kSan. We compare the value of a with an upper limit value (default is 3.5 angstroms), and a lower limit value (default is 2.5 angstroms). If a is less than the lower limited value, the separation weight is 1; if a is bigger than 3.5, the separation value is 0. If $2.5 < a < 3.5$, the weight is equal to $(3.5 - a)$ angstroms.

The second function is designed to find the variable that determines the angle of orientation in the FCC (110) of the grain. In this step, we use a vector (OA) to connect the object particle and the projected particle. We also assign a reference vector that is called **'Zero vector'**. This **'Zero vector'** is in the FCC (110) plane. In our example shown in Figure 4.5, it is parallel to the [001] direction. This angle is the θ for the projected particle in Figure 4.5.

So far we have a list of angle values with the angular weight and separation weight for all neighboring particles of the object particle. We now need one variable to determine the arrangement of the surrounding particles. In this step, for each neighbor particle of the object particle, we determine its orientation value according to **Weight of Angle From Plane**, **Separation Weight**, and the angle between the projected vector and the **'Zero vector'**. We call this orientation value **Axis Angle**, and the function '**Axis Angle Tracker**' function in kSan.

In **Axis Angle Tracker**, we first divide the **Symmetry Angle** by 6. Here **Symmetry Angle** is 360 degrees divided by the highest symmetry axis in the plane of interest. For example, if the structure has four-fold symmetry in the discussed plane (such as the FCC (100) plane), the symmetry angle is 90 degrees. For the FCC (110) plane, the **symmetry angle** will be 180 degrees. After dividing **Symmetry Angle** by 6, we make an array with 6 slots, which corresponds to 1/6 of **Symmetry Angle**, **2/6 of Symmetry Angle**, 3/6... and 6/6 of **Symmetry Angle**. For FCC (110) plane, each slot of the array corresponds to 30 degrees, 60 degrees, 90 degrees, 120 degrees, 150 degrees, and 180 degrees.

For each **Axis Angle**, we calculate the difference between the **Axis Angle** and

the $i/6$ of **Symmetry Angle** and set this difference to **DiffAngle to i/6 of the Symmetry Angle**. Then we use a function to fit 6 **DiffAngle to i/6 of the Symmetry Angle** into a curve that has a bell shape. This function is called **Splat Function**. The steps of **Splat Function** are:

- Set $\mathbf{DiffAngle_i} = axisAngle - i/6 \times \mathbf{SymmetryAngle}$.
  If $\mathbf{DiffAngle_i} > 90$, then
  $\mathbf{DiffAngle_i} = \mathbf{DiffAngle_i} - 90$;
  If $\mathbf{DiffAngle_i} < -90$, then
  $\mathbf{DiffAngle_i} = \mathbf{DiffAngle_i} + 90$;

- Then, we use each **DiffAngle** over the symmetry angle and times 3:

$$\alpha = 3 \times \frac{\mathbf{DiffAngle_i}}{\mathbf{SymmetryAngle}} \tag{4.2.1}$$

  Since $\mathbf{DiffAngle_i SymmetryAngle}$ is between -0.5 to 0.5, the value of α is between -1.5 to 1.5.

- After that, we used **Splat Function** to turn α into a value between 0 to 0.75. Figure 4.6 shows the plot of this function. if $-0.5 < \alpha < 0.5$, then

$$y = 0.75 - \alpha^2 \tag{4.2.2}$$

  if $|\ \alpha\ |$ is between 0.5 and 1.5, then

$$y = 0.5 \times (|\ \alpha\ | - 1.5) \tag{4.2.3}$$

- Finally, we multiply y with two weight values:

$$P_i = y \times weightofAngle \times weightofSeparation \tag{4.2.4}$$

- P_i will be added into the i^{th} element of the tracker array.

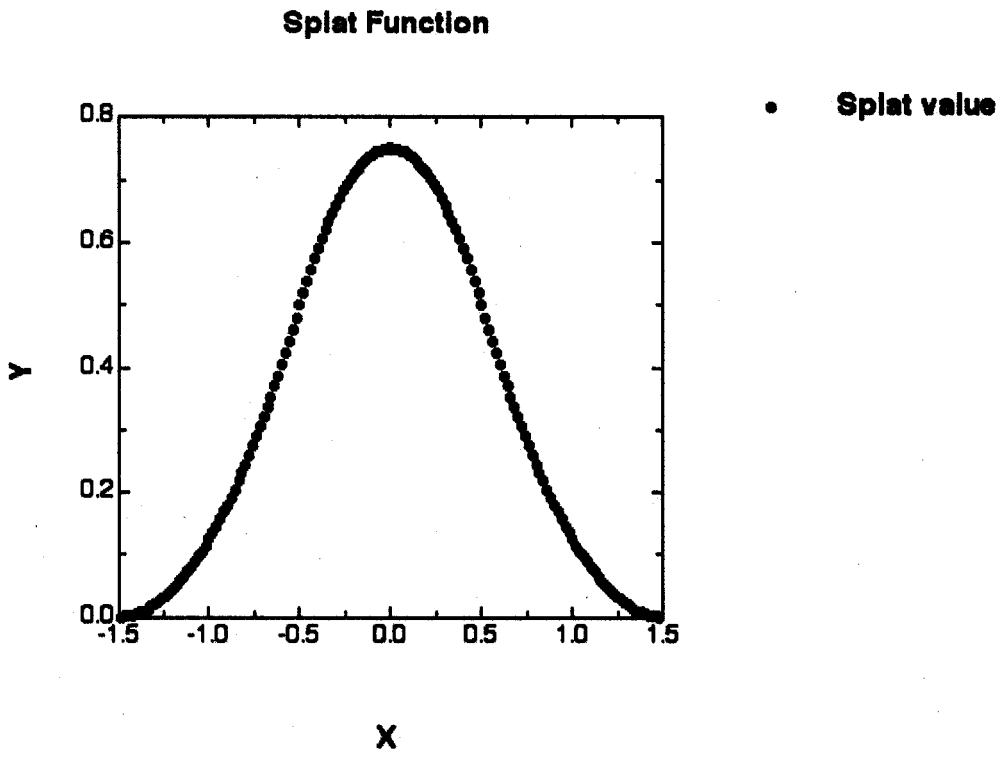

Figure 4.6: Splat function, which assigns values between 0 to 0.75.

We calculate all neighbor particles around the object particle and splat them into 6 values. These values will be added into the 6 elements of the array. Because we put weight values into the elements of the tracker array, the particles that are far from the object particle have less weight and, are less important to the value of the elements in the array. By using different **Acceptance Angles**, upper limit values, and lower limit values for the separation weight calculation, we are able to change the number of the particles that contribute to the final values. After we have the final values for all 6 elements in the array, we search for the maximum value among these 6 values. If $Array[i]$ has the biggest value, we will fit the values of $Array[i-1]$, $Array[i]$, and

$Array[i+1]$ into a quadratic curve. The Y axis is the value of the elements in the array, and the X axis are the values of the angle corresponding to these elements. On this curve, we will find the extremum where the slope of the curve is equal to zero, and choose the angle value that corresponds to this value on the X axis to be the orientation value for the object particle. By this means, we are able to average the orientation of one particle's surrounding particles while considering their symmetry relationship. For the last step, we assign a particle's color property according this is orientation value the completion step for this "**color by angle**" function.

In Figure 4.7, we plot all the **Axis Angle** related to different orientation; here we still use direction [001] as the reference '**Zero Vector**', the X axis is the orientation angle of the grain to which the particle belongs, and the Y axis is the Axis angle value kSan calculated by using this algorithm. This shows that our calculation is successful, and the angle value ranges between 0 to 1. Figure 4.8 is the snapshot taken for the same structure as the one in Figure 4.1, but with this new colorizer. In our study, we observed some new phenomena that are hard to distinguish without the help of this new colorizer. These interesting results will be explained in the following chapters.

4.3 Pressure of the simulations

For all our simulations, we used constant volume and constant temperature conditions. However, since we used equilibrium lattice constants for all the simulations, the pressure of the structure should not introduce extra stress to the system. We calculated the values of the pressure at different simulation steps to test if the pressure of the system changed significantly during the simulation. We found that the pressure in our simulations is very low and its influence on the simulation results can be neglected. Take simulation 3526-060906 with $R_o = 35.26$ as an example. The average total energy after 3ps simulation was -12858eV, with standard deviation equal to 2.2026eV. We then expanded the simulation cell size in the x direction from 51.81A to 51.82A, which increased 0.2% of the simulation cell size in x direction. We also

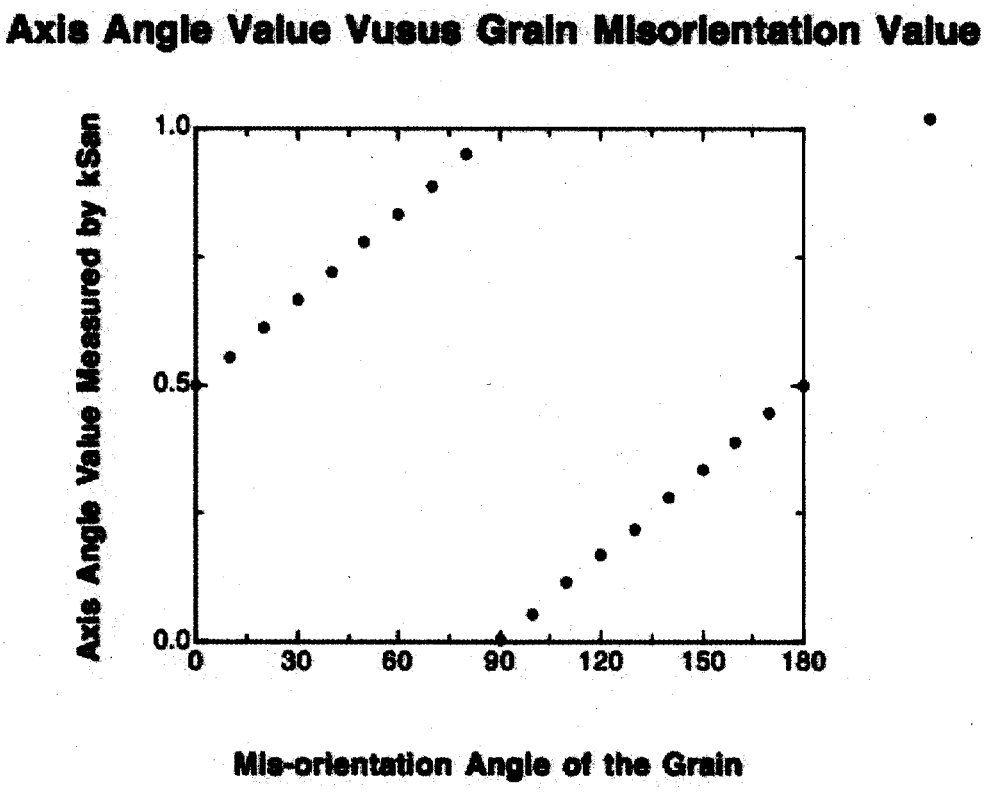

Figure 4.7: Calculated axis angle value versus orientation value of the grain to which the particle belongs.

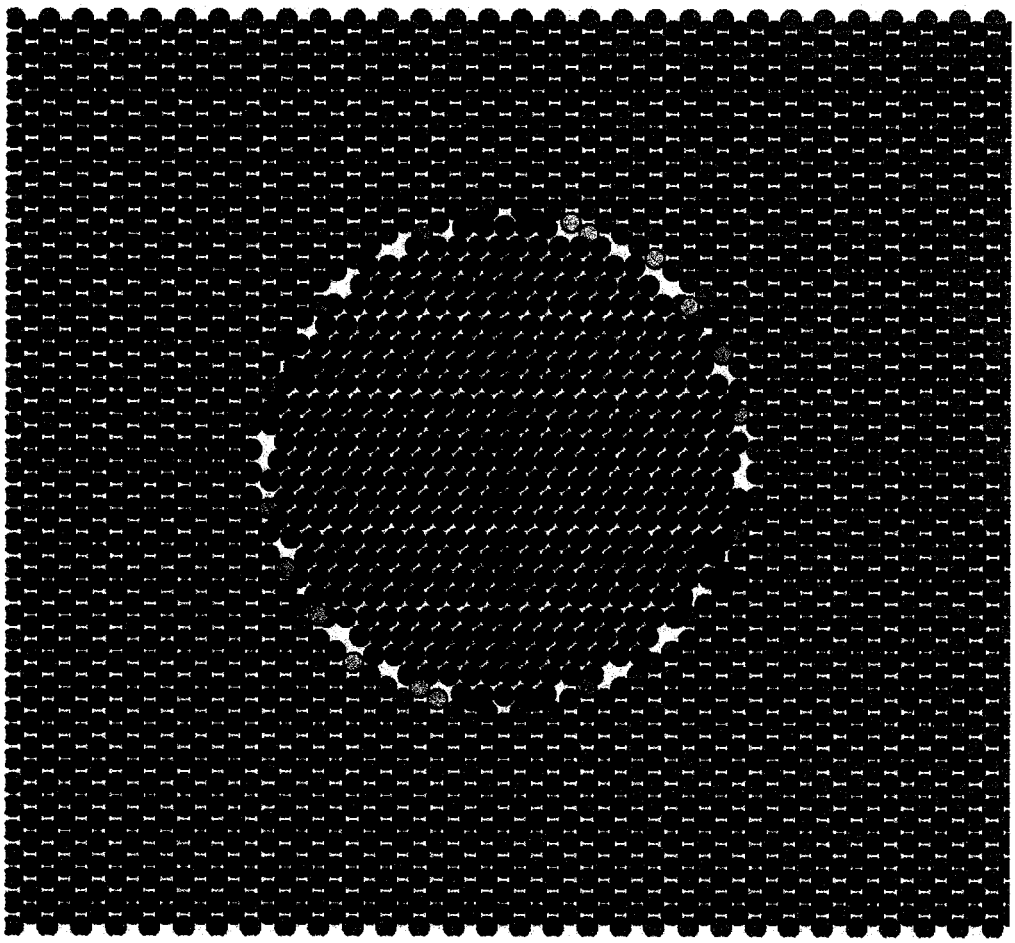

Figure 4.8: Color particles by using each particle's axis angle, before we started simulation. R_o=35.26

increased each particle's x position by 0.2%, and let the simulation run for 3000 steps, which is 3ps. The total energy is -12858eV, and the standard deviation is 3.0747eV. Pressure is proportion to the change of the energy over the change of the volume. $P \propto \frac{\triangle E}{\triangle V}$. Since total energy is not changing, the pressure of the system at this simulation time is very low. Then we take the total energy at 26ps of the simulation and

Table 4.1: The energy values before and after changes of system volume at different simulation steps.

Samples	Total Energy(eV)	Standard deviation(eV)	$\triangle E(eV)$	$\triangle V(\AA^3)$	Pressure(eV/$\AA^3$)
after 3ps	-1.2858E4	2.2026			
expand after 3ps	-1.2858E4	3.0747	0	19	0 ± 0.14
after 26ps	-1.2857E4	2.1888			
expand after 26ps	-1.2857E4	2.066	0	19	0 ± 0.11

record the total energy again. We still did not observe significant changes in the total energy. Therefore, the pressure of the system at this simulation time is still very low. We list all the data in Table 4.1. In all the energy measurements, we take 47 data points as samples. So pressure does not play an important role in the evolution of our system.

Chapter 5

GRAIN BOUNDARY EXCESS ENERGY AND SIMULATIONS WITH EMBEDDED GRAINS

5.1 Grain Boundary Excess Energy

5.1.1 Simulation structure and method of measuring grain-boundary excess energy

Before we used MD simulation to study the morphology of the grains and the mechanisms of grain growth, we needed to obtain the excess energy values of grain boundaries of FCC systems with different geometrical parameters. We first need to have a structure to measure the excess energy of the grain boundaries. Our goal is to obtain a grain boundary system that has a grain boundary with particular geometrical parameters. Then, after we structure the simulation system, we need to know: (1) the total area of the grain boundary in the grain boundary system, A; (2) the total energy of the system with planer grain boundaries at equilibrium, E_{total}; and, (3) the number of particles in the system, n. We also need the energy of each particle inside an FCC single crystal as the reference: $E_{ref/particle}$. Here, we need to obtain all energy informations at same temperature. Then we can express the excess energy of the grain boundary by equation 5.1.1 [76]:

$$E_{gb} = (E_{total} - n \times E_{ref/particle})/A \tag{5.1.1}$$

However, it is difficult to achieve a structure that only includes one type of grain boundary. As we explained in Chapter 2, we used periodic boundary conditions for our MD simulation to eliminate surface effects. Although periodic boundary conditions will not influence the conservation of the energy and the velocities, they impose constraints on the structure. kSan's properties require that all simulation cell boxes

be orthorhombic. With the image cells at each side of the primary simulation cell, the whole system is periodic in three directions along each boundary of the primary simulation cell. This is the periodicity of the entire simulation structure, with the primary simulation cell as the periodic unit. However, the crystal structure we studied has long-term periodicity. Therefore, to represent the infinite periodicity of the crystal structure in our simulation structure including image cells, we need to fit our crystal periodicity into the periodicity of the simulation cell. Thus periodic directions of the crystal must be parallel to the boundary direction of the primary simulation cell. This is not hard to attain for a FCC single crystal because of its cubic structure. We simply need to ensure that each periodic direction of FCC is parallel to the boundary direction of the simulation cell, and let the size of the cell be integral multiples of the FCC lattice unit structure. However, for bicrystalline and polycrystalline structures, it is hard to obtain a structure free of distortion at simulation cell boundaries because at least one crystal's periodic direction will not be parallel to the boundary of the simulation cell.

In our first design, the structure included two equal-sized grains, as shown in Figure 5.1. For this structure, we need to slightly change the lattice parameters of the FCC structure so the whole structure can fit into the orthorhombic cell box of the simulation. However, in most cases, the structure will no longer be cubic due to the change of the lattice parameters and inclusion of more periodicities along the boundary of the simulation cell. Thus, the symmetry of the crystal is reduced (not a cubic structure). Sometimes, with both grains rotated, it is impossible to have the structure periodic in the direction of the simulation cell boundaries within reasonable simulation scales. Consequently, we developed another design for our simulation structure.

In our second design, one side of the simulation cell box is much longer than the other two. We put one of the two grains in the middle of the simulation cell box surrounded by the other grain, with the grain boundary plane we want to study parallel

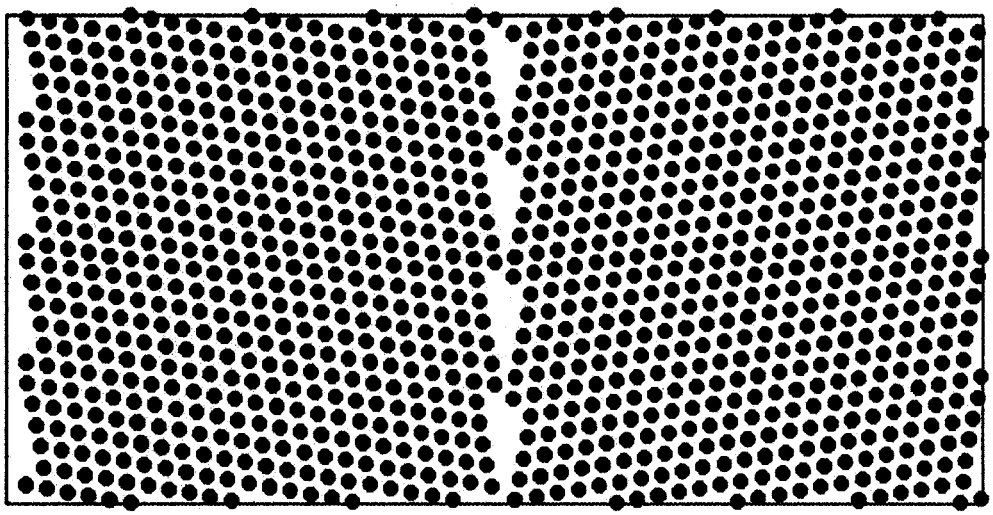

Figure 5.1: The structure used in studying the grain boundary excess energy.

to the elongated boundary of the cell box as shown in Figure 5.2. In this structure, the distance between the grain boundaries, and between the grain boundaries and the simulation cell boundaries, needs to be big enough so that the interactions between the boundaries are small enough to be neglected. After the structure relaxes to a local equilibrium state, instead of determining the sum of the energy of every particle in the system, we only determine the energy of the n particles that are inside the area outlined by dashed lines in Figure 5.2. We still use equation 5.1.1 to calculate the excess energy of the boundary. However, with this structure, area $A = 2 \times l \times d$; here l is the length of the rectangular shape marked by the dashed line, and d is the thickness of the simulation cell. By using this method, we involve more grain boundaries and interfaces in our simulation system, but calculate only the excess energy associated with the grain boundaries of interest. We successfully eliminate the interface effects and determine the energy of grain boundaries of FCC system with arbitrary geometric parameters at relatively low temperature with this simulation structure. However, we found that at relatively higher temperatures, such as 800 degree Kelvin, the grain

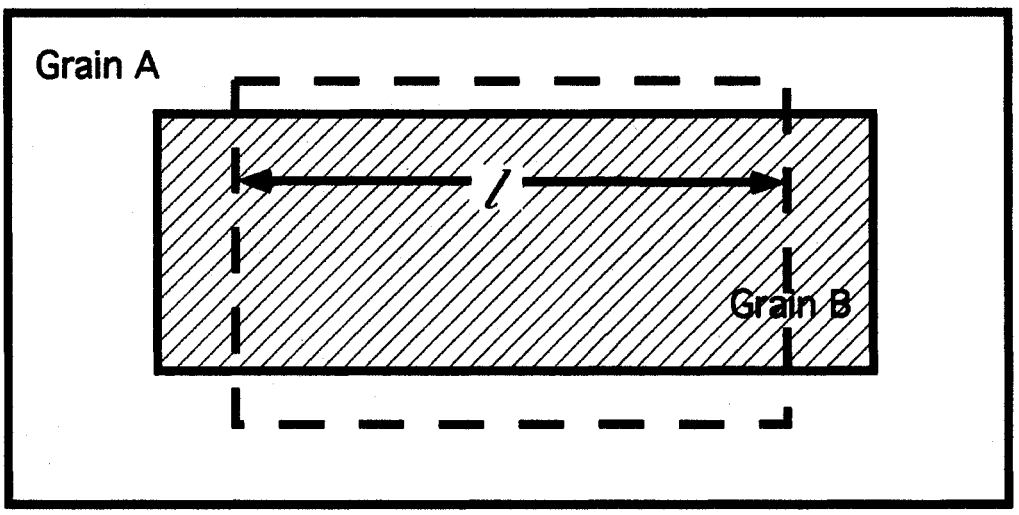

Figure 5.2: The structure used in studying the excess energy of the grain boundary: the E_{total} only included the energy of the particles in the dashed lined rectangular area.

boundary excess energy measured with this structure is not consistent if we change the calculation scope. Here, by calculation scope, we mean the dashed the size of the lined box drawn in Figure 5.2 in which the energy of the particles are added up as E_{total} in equation 5.1.1. And the data we achieved by using this method at higher temperatures are not reliable. The following paragraphs describe the method we used to test the reliability of this structure for measuring grain boundary excess energy.

We tested several parameters that might influence the results of the measurement: simulation duration, simulation size, and calculation scope, which is the area outlined by the dashed line in Figure 5.2, both in length and width. We also decrease the calculation scope so that it only includes one grain boundary and compare the results with those that include two grain boundaries in the calculation. Figure 5.3 shows the calculation scope that only includes one grain boundary instead of two. Table 5.1 gives the data we achieved for one particular grain boundary, the color grain boundary with 60-degree misorientation between the two grains at 800 degree Kelvin. Data has

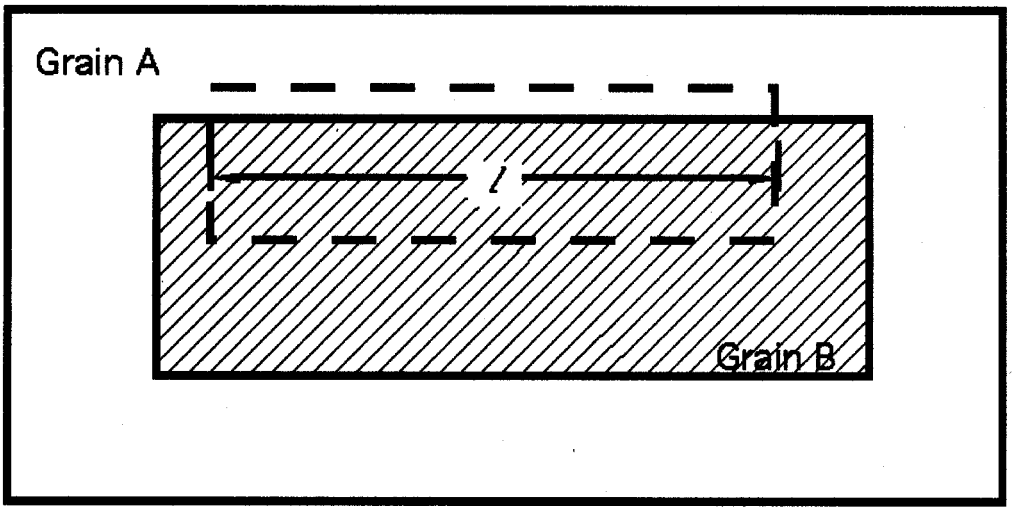

Figure 5.3: The structure used in studying the energy of the grain boundary with only one grain boundary included into calculation: the E_{total} only included the energy of the particles in the dashed lined rectangular area.

been obtained at 8000, 8020, and 8040 simulation steps. In column one, we calculate all the particles inside of the dashed line boxes as shown in Figure 5.2, with the size in the X direction equal to 123 $\mathring{A}$, which is about 50% of the size of the surrounding grain in X direction, and 75% of the embedded grain; with size in the Y direction equal to 100 $\mathring{A}$, which is about 70% of the Y direction size of the surrounding grain, and 117% of the embedded one. In the second column, we decrease the number of particles calculated in 5.1.1 by decreasing the size in the X direction of the dashed line box by 3.4 $\mathring{A}$, while in the third column we increase it by 3.45$\mathring{A}$. For the fourth column, we decrease the calculation scope in the Y direction so that only one grain boundary is included in the calculation, as shown in Figure 5.3. In the fifth column, we keep the calculation size the same as the original measurement in the first column, but increase the simulation size by 2$\mathring{A}$ in the Y direction. All energy values have units of eV/nm^2.

The results show that the grain boundary excess energy obtained at this tem-

Table 5.1: The energy of the color mirror plane grain boundary with 60-degree misorientation between two grains with different simulation sizes, calculation scopes, and simulation steps.

Simulation Steps	Original sim Size and Scope,	Cal scope-3.45Å	Cal scope+3.45Å	Include one grain boundary	Cell size in Y direction +2Å
8000	4.45	4.11	4.84	3.64	5.94
8020	4.40	4.50	4.91	3.75	5.78
8040	4.24	3.91	4.58	3.94	5.69

perature is very sensitive to the simulation size, or in the other words, the distance between the grain boundary and the simulation cell boundary. By letting the simulation run another 2000 steps using the same geometric conditions as in column one, we obtained the $energy/area = 2.815eV/nm^2$, which is only 65% of the data produced at 8000 simulation steps. We tested different grain boundaries and different simulation sizes, and again concluded that our simulation size is not big enough to eliminate the influence of the simulation cell interfaces caused by periodic boundary conditions at high temperatures. Hence, we needed another simulation structure to obtain the grain boundary excess energy at this temperature. We illustrate this problem in Figure 5.4. The periodic boundary conditions will influence the area outlined by red lines in Figure 5.4, which is equivalent to bringing one more grain into the simulation system at each side of the simulation box.

Since our simulation size is reaching the limit of kSan, which is around 30,000 particles in one simulation, the only way for us to calculate the grain boundary excess energy at high temperature is to keep the FCC unit cell's [110], [100], and [001] direction of the outside grain parallel to the x, y, and z direction of the simulation cell box. Therefore, to obtain the energy of an arbitrary grain boundary, instead of rotating both grains, we need a method that only rotates the embedded grain but tilts the grain boundary planes, as shown in Figure 5.5. Using this structure, we need to

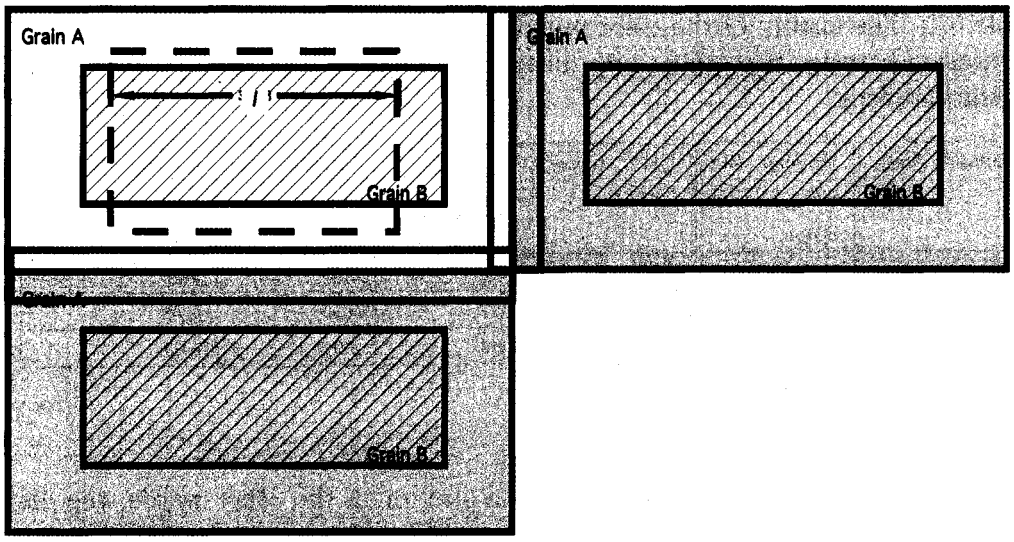

Figure 5.4: This illustration shows the area that will be influenced by the periodic boundary conditions for the second structure design of the grain boundary excess energy measurement simulation.

tilt both grain boundaries and the dashed line box in which the particles' energy are added up as E_{total} in equation 5.1.1, as shown in Figure 5.6. We use vector $P(px, py)$ to represent the direction of the grain boundary in the X-Y plane, which is also the (110) plane for both of our grains. In the following paragraphs, we explain how to script the structure and how to structure the scope for calculation.

In our structuring script, before we generate an particle in the simulation, we import X parameter and Y parameter of a chosen position and use these coordinator parameters in vector $V(x, y)$. Then, we project $V(x, y)$ to the $T(tx, ty)$ direction, which is perpendicular to the $P(px, py)$ direction and the grain boundary plane. Then, we compare the absolute value of it (the distance of the point V to vector $P(px, py)$) with d, which is the thickness of the grain B in T(tx,ty) direction. We make a particle at V belonging to grain B if the distance between point V and $P(px, py)$ is smaller than d, and distance between V and origin is less than L. Otherwise we make a particle at V belonging to grain A. This will give the tilted embedded grain the FCC

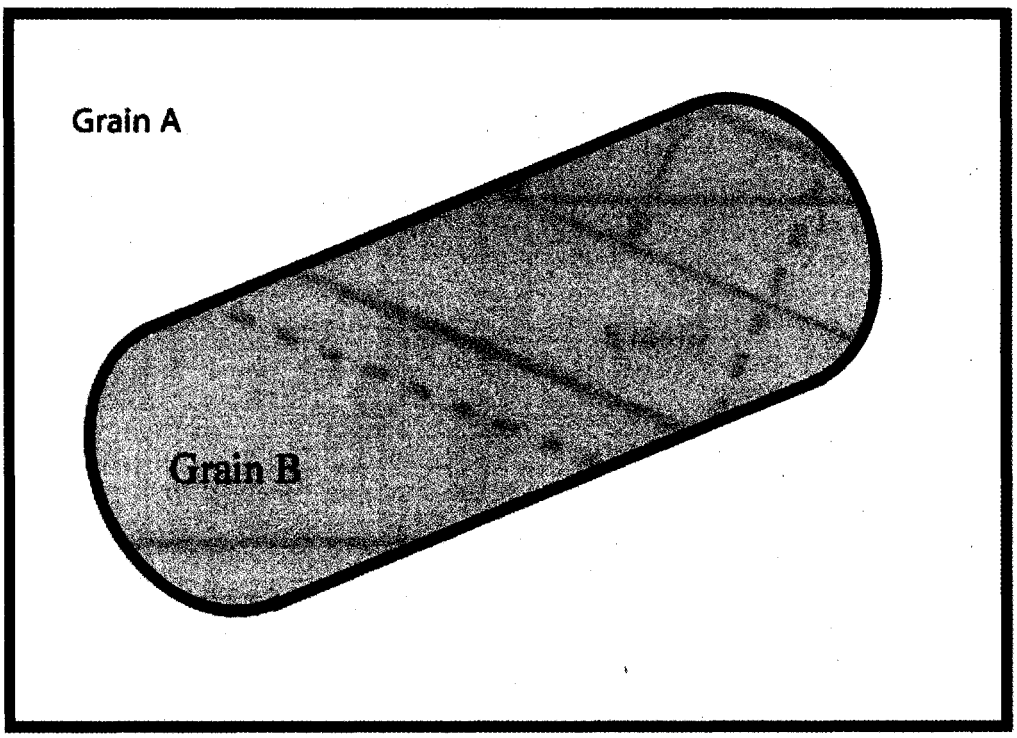

Figure 5.5: The simulation structure that we need to use for higher temperature.

common (110) plane as shown in Figure 5.6. Grain A and grain B both have FCC structure, but their grain orientations differ. With this structure, we calculate the

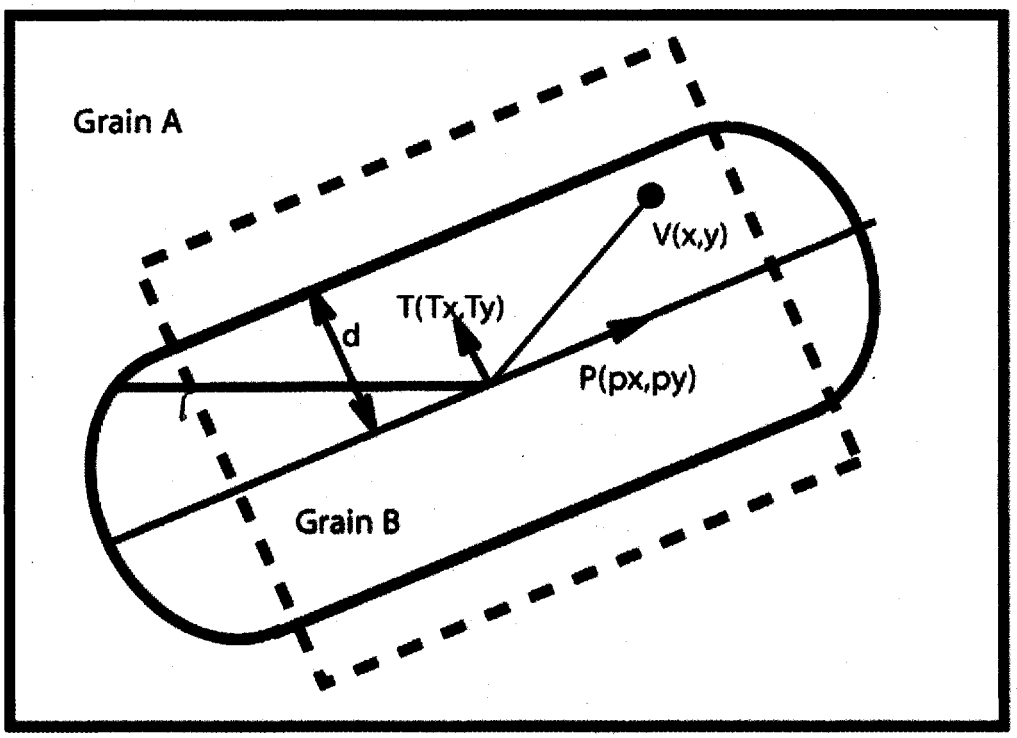

Figure 5.6: The simulation structure that we need to use for higher temperature.

energies of the particles inside the area outlined by dashed lines in Figure 5.6 as E_{total} in equation 5.1.1. Figure 5.7 gives a snapshot of the structure of these simulations. We tested this simulation structure and obtained consistent and reliable simulation results for the excess energy of the grain boundaries. We also tested the simulation results with different simulation sizes, simulation scopes both in width and length, and simulation steps. Table 5.2 lists part of the test results for the color mirror plane grain boundaries with misorientation between two grains in the common FCC (110) plane, R, equal to 90 degree. Here the unit for energy is eV/nm^2.

This table reveals that the data we collected around 12000 simulation steps are

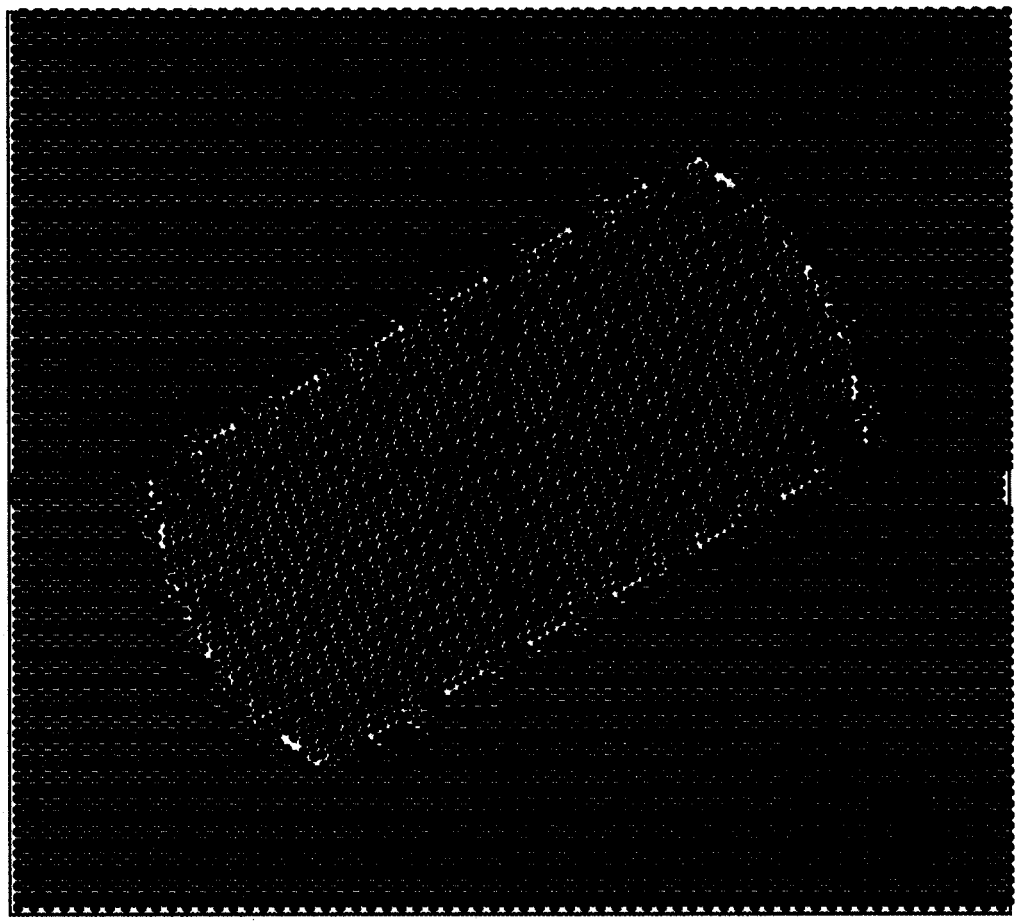

Figure 5.7: The simulation structure that we need to use for higher temperature.

Table 5.2: The average grain boundary excess energy of color mirror plane grain boundary measured by using different sampling size in width and length with different simulation duration.

t=70Å, l=	30	32	34	36	38	40	45	50	60
after12000	7.706	7.636	7.773	7.589	7.215	7.236	7.392	7.394	7.715
after12200	7.001	7.6.794	6.831	6.480	6.877	6.191			
after12400	6.738	6.474	6.274	6.312	6.344				
after22400	5.537	5.803	5.969	5.198	5.696	5.798	5.918	5.903	5.311
after22600						5.951			
after22800						5.578			

too scattered. But after 22400 simulation steps, which is about 22.4 ps in simulation time, the results are constant and do not depend on the size of the simulation, and number of particles involved in the calculation. Therefore, to obtain reliable data, we need to simulate the structure with longer simulation duration, and to collect more data by using a different calculation scope and calculate the average. For the color grain boundary of 45-degree misorientation between two grains, the average grain boundary excess energy of the data we collected around 22400 simulation steps is $5.696 eV/nm^2$.

5.1.2 Results

In our study, we obtained the excess energies of many grain boundaries. In our simulations, we observed the embedded grain simultaneously faceting into grain boundaries which allows one grain's $(1\bar{1}\bar{1})$ to be parallel to another grain's (001) plane, and one grain's $(1\bar{1}\bar{2})$ to be parallel to the other grain's $(1\bar{1}0)$ which are neither SDE grain boundaries nor CSL grain boundaries. These grain boundaries both exist at $R = 35.26^o$. So we calculate the excess energies of the color mirror plane grain boundaries with R=35.26 degree and these two boundaries at this misorientation besides all the other SDE grain boundaries. Some of the excess energy values of the grain boundaries are listed in Table 5.3 in the unit of eV/nm^2 for the low temperatures. In Table 5.3, we list the excess energies of the grain boundaries located on top of the color-mirror planes and the classical-mirror plane of $R = 90^o$; the energy of color-mirror plane grain boundary with $R = 45^o$, the grain boundaries that make one grain's $(1\bar{1}\bar{1})$ parallel to another grain's (001) plane; the grain boundaries that make one grain's $(1\bar{1}\bar{2})$ to be parallel to the other grain's $(1\bar{1}0)$; the grain boundary on top of the color-mirror planes with $R = 35.26^o$ which is the misorientation allows these index planes to be parallel to each other; and average excess energy of grain boundaries at two temperatures: T equal to 15, which is approximately 1/10 of the melting temperature, and T equal to 500, which is approximately 1/3 of the melting

temperature. We used the second method described in the earlier section to obtain the energy of the grain boundary, which rotate both enclosed and embedded grains, but have grain boundary parallel to the simulation cell boundary. All the SDE grain boundaries are not coincident site lattice grain boundaries for the FCC structure. Figure 5.8 shows the data.

Table 5.3: The energy of grain boundaries with different geometrical parameters of fcc system taken at T=15K and T=500K. The unit of the grain boundary is eV/nm^2.

Energy(ev/nm^2)	T=15 (K)	T=500 (K)	Energy(ev/nm^2)	T=15 (K)	T=500 (K)
classical R=90	8.974	3.579	$(1\bar{1}\bar{1})//(001)$	7.175	5.828
color R=90	10.807	7.890	$(1\bar{1}\bar{2})//(1\bar{1}\bar{1})$	9.260	7.771
color R=35.26	4.791	4.320	color R=60	10.257	6.406
color R=45	11.960	9.878	Arbitrary GB	13.839	10.431

Using the grain boundary excess energy values, we constructed approximate possible Wulff plots for the fcc (110) bicrystalline system with different misorientation, R. We gave two Wulff plots for the systems with R equals to 35.26^o and 90^o in Figure 5.9. The length of the red solid lines corresponds to the measured values of the grain boundary excess energy, the other values on the plot are approximated values. The Wulff plots are outlined by the purple lines, and the Wulff forms which correspond to the equilibrium shape of the embedded crystal growing in a crystalline environment are outlined by the blue solid lines.

For 800K, using the third structure mentioned in Section 5.1.1. We let the simulation run for over 25000 steps and average the total energy of the last 60 simulation steps. Table 5.4 lists partial results of grain boundary excess energy. Figure 5.10 shows the excess energy values of the grain boundaries.

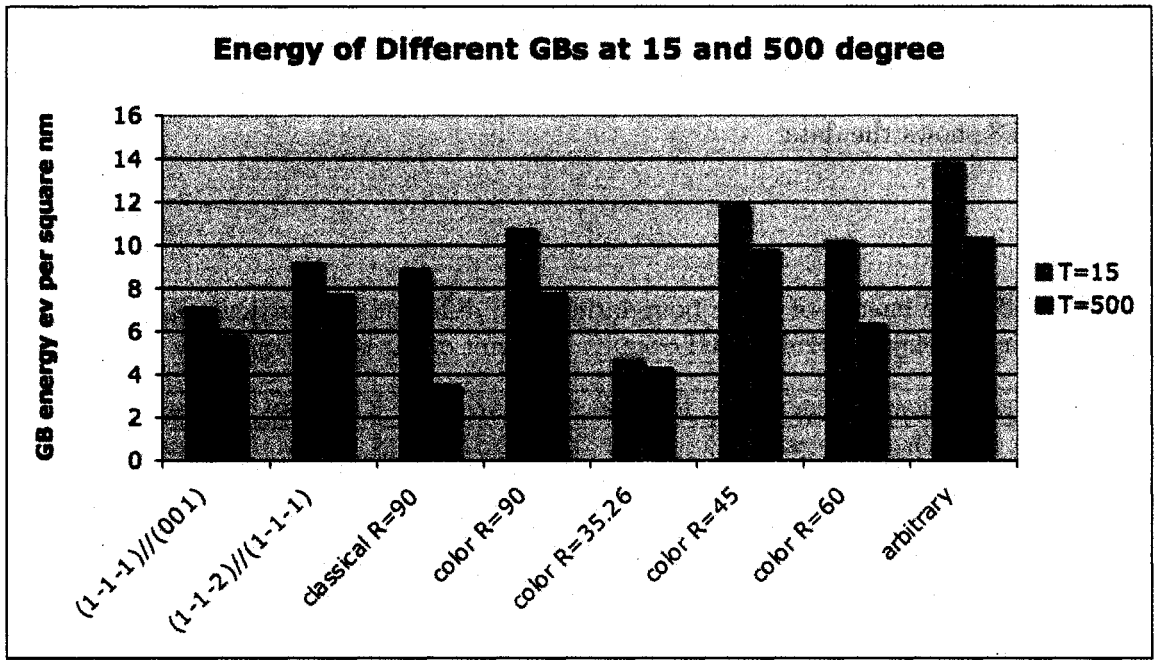

Figure 5.8: The excess energy of the grain boundaries in the fcc structure at 15 K and 500 K.

Table 5.4: The excess energy of grain boundaries with different geometrical parameters of the fcc system taken at T=800K. The unit is eV/nm^2.

Energy(ev/nm^2)	T=800 (K)	Energy(ev/nm^2)	T=800 (K)	Energy(ev/nm^2)	T=800 (K)
classical R=90	5.111	$(1\bar{1}\bar{1})//(001)$	4.941	R=35.26, $\theta = 50$	6.101
color R=90	5.498	$(1\bar{1}\bar{2})//(1\bar{1}\bar{1})$	9.7038	R=35.26, $\theta = 60$	5.918
color R=35.26	5.225	R=35.26,$\theta = 20$	8.150	R=35.26,$\theta = 70$	7.153
color R=60	5.944	R=35.26,$\theta = 30$	5.597	R=35.26,$\theta = 80$	6.609
R=35.26, $\theta = 10$	7.589	R=35.26,$\theta = 40$	4.863		

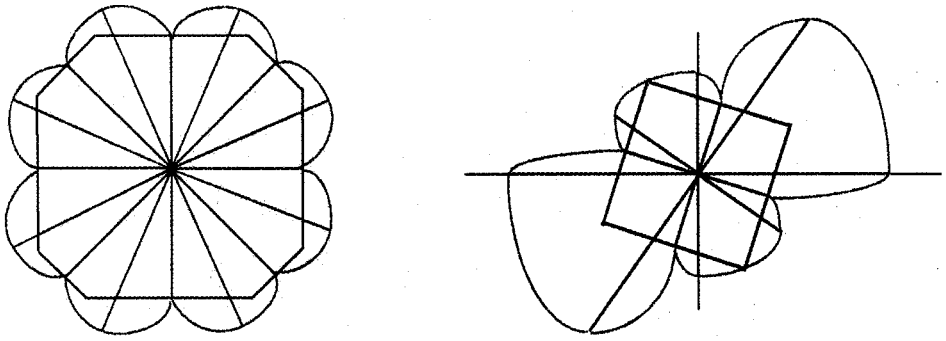

(a) Wulff plot of fcc (110) with $R = 90^o$ (b) Wulff plot of fcc(110) with $R = 35.26^o$

Figure 5.9: The possible Wulff plot of two fcc (110)//(110) systems.

5.1.3 Discussion

From Table 5.3 and Table 5.10, we see that the excess energies for all special grain boundaries are lower than the excess energy of the arbitrary boundaries. The lowest grain boundary excess energies are the boundaries with $(1\bar{1}\bar{1})//(001)$, and the color-mirror plane boundary at $R = 35.26^o$. These grain boundaries all exist in the system with two grains misorientated with each other by 35.26 degrees. Moreover, at temperature equal to 800K, most of the grain boundaries with $R = 35.26^o$ have lower excess energy than the other grain boundaries at other R values. Hence, $R_o = 35.26^o$ should be an energy preferred mis-orientation in (110) plane.

We found that most of the grain boundaries have higher excess energy at lower temperature that at lower temperature, which is to be expected.[77]

As explained in Chapter 2, SDE boundaries are either energy minima or energy maxima. Since we observed that all these SDE boundaries are stable during the simulation and have relatively lower energy than general grain boundaries, we concluded that these SDE boundaries are all local energy minima. Our MD measurements for grain boundary excess energy are consistent with the experimental measurement results which range from 0.01 to 0.3 ev/nm^2. [2] .

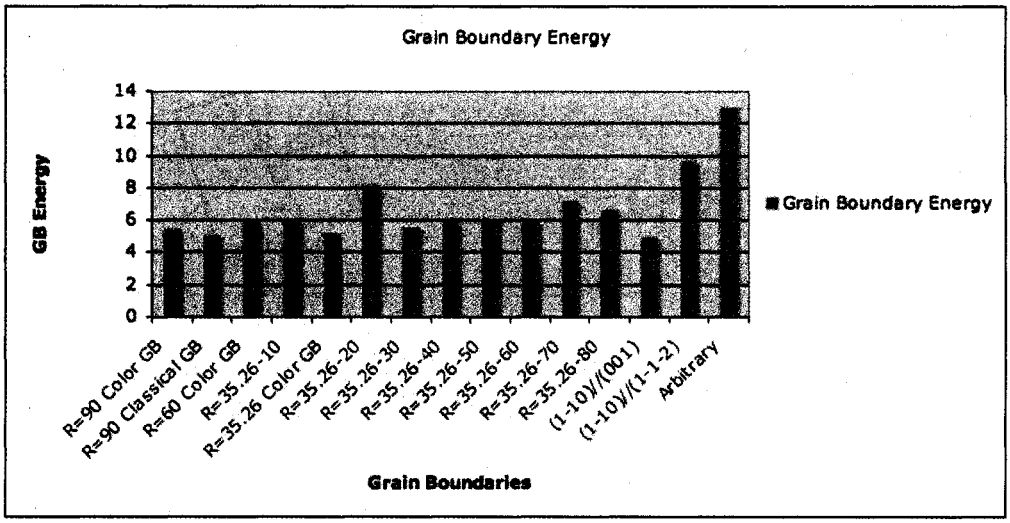

Figure 5.10: The excess energy of the grain boundaries in the fcc structure at 800 K.

5.2 *MD simulations with a columnar grain embedded in a bigger grain*

5.2.1 *Structure and method of simulation with a columnar grain embedded in a bigger grain*

We used a columnar-shaped starting structure for our MD simulations. We made a columnar-shaped hole in a big crystal, and filled the empty space with a columnar-shaped grain, as shown in the schematic drawing in Figure 5.11. Since we are using

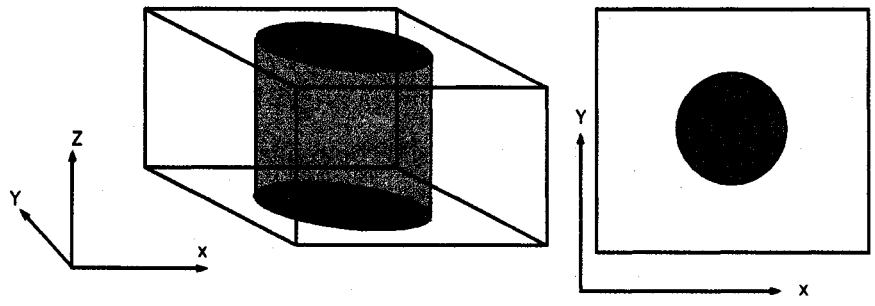

Figure 5.11: The column-shaped embedded grain.

periodic boundary conditions for our simulations, which include simulation cell images on every side of the simulation cell, the columnar-shaped grain has infinite length in the Z direction. Therefore, the embedded grain can only rotate in the FCC common (110) plane. Moreover, the grain boundaries in this system are always perpendicular to the FCC (110) plane, which is the X-Y plane in Figure 5.11. So the only geometric parameters that are free to vary are the misorientation in the (110) plane around the common [110] direction of both grains, which is denoted by R in our earlier discussion, and the grain plane boundary normal orientation in (110) plane, which is denoted by θ in our earlier symmetry discussion.

Our starting structures are scripted by Applescript language with the position of each particle defined by three parameters. The [110],[001],[1$\bar{1}$0] directions of the surrounding grain are parallel to the boundary directions of the simulation cell. For the embedded grain, we first script the position of each particle by the same method used to construct the surrounding grain; then, we give a rotation for each vector that defines the position of the particle. In this way, we have two grains misoriented with each other by a certain degree, with one grain embedded in the other. We define the starting misorientation between two grains as R_o. However, the rotation operation will bring some particles at the boundary area too distant or too close to each other, and sometime, even cause overlap of particles. In these cases, extra stress and unreasonably high energy will be brought into the system at grain boundaries. If we start the simulation at this situation, the system will experience a "blow up" caused by high stress even at very low temperature. To avoid this, we use the conjugate gradient minimization method (CGM) before we start the Verlet iterations for each experiment. The CGM searches for the arrangement of the particles around the boundary area with lower energy. Within less than 10 steps of CGM, we are able to remove the high stress of the system and be ready for MD iterations. This method helps us to solve the problem of overlapping particles without reducing the number of particles in the system. Thus, it is considered to be better than by just deleting

the overlapping atoms.

To conduct simulations within reasonable computational times, we usually did our simulations at relatively high temperatures. To heat up the system, we scaled the velocities of the particles before we iterated the system so that the average molecular kinetic energy of the system is equal to $3/2\kappa T$, here κ is Boltzmann constant, and T is temperature. We re-scaled them every thermal time constant, which was 0.3 pico-second, during the whole simulation to make sure that the simulations were under constant temperature.

We started all simulations with exactly the same scripting method with the same simulation size, and we used similar CGM steps for each simulation experiment. Thus, all our experiments have similar starting conditions and results can be compared. The following sections present the results of some of our MD simulations.

5.2.2 Results

We simulated the bicrystalline structure with embedded columnar grain using different starting misorientations, R_o, at constant temperature. These included the SDE of R with $R_o = 90^o$; the misorientation with lowest grain boundary energy, $R_o = 35.26^o$; and general R with $R_o = 45^o$, $R_o = 60^o$, $R_o = 70^o$, etc. We recorded data of the systems every 20 stimulation steps, including total energy, the kinetic energy, and temperature. Each simulation step is about 1E-15 seconds. Meanwhile, we also took snapshots of the simulation from the [110] direction of both fcc grains every 20 simulation steps. We created movies for each simulation using these snapshots as frames. We also periodically saved the information for each particle's position and velocity. Such information will allow us to observe the simulation through different observation directions besides [110] at several break-points after the simulation is halted.

We plotted the total energy and temperature of the systems as functions of simulation time, corresponding to system simulation steps. As shown in Figure 5.12, the total energy of the system experienced an equilibration at the early stage of

the simulation, syncing with the equilibration of the temperature. According to our observation, every simulation at the same temperature has a similar pattern for equilibration during the first 2000 simulation steps, which is about 2ps in real time. With a starting temperature at 800K, and random velocities for the particles in the simulation system, the system temperature can shoot up to 1600K during the equilibration period.

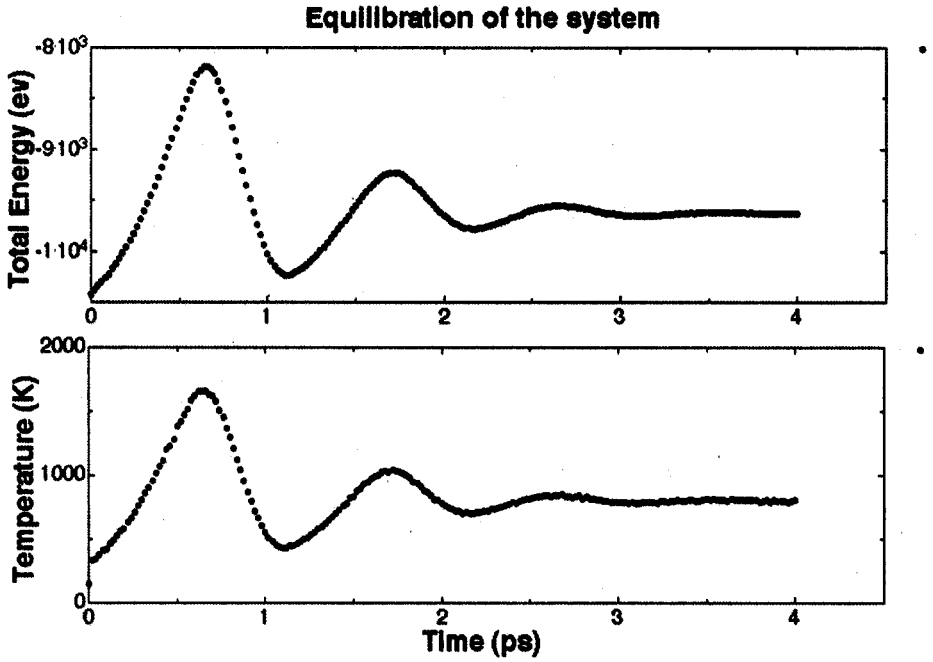

Figure 5.12: Thermal equilibration of the system.

Figure 5.13 gives an example of the total potential energy as a function of simulation steps with longer simulation period, about 100 ps. In this figure the potential energy of the system shows obvious change only at the beginning of the simulation, syncing with the equilibration of the temperature. Later, after thermal equilibration, the total potential energy shows limited changes during the system evolution.

In our two simulations with $R_o = 90^o$ at temperature equal to 800 K, the embedded grains shrank and disappeared. In one of the simulations, the embedded grain

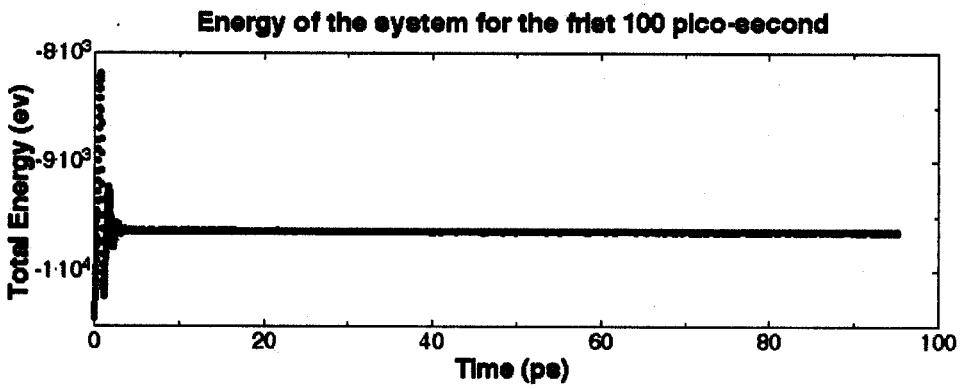

Figure 5.13: Potential energy of the system versus simulation time with longer simulation time.

disappeared at 35952 simulation step, which corresponds to 36ps in real time; in the other, the embedded grain disappeared at 124ps. We plotted the potential energy of the system as a function of simulation steps for both simulations in Figures 5.14 and 5.15.

We conducted five experiments with $R_o = 35.26^o$ at temperature equal to $800K$. We use different names, such as R35.26-1 or R35.26-2, to indicate different simulations. Simulations R35.26-1, R35.26-2, and R35.26-3 used 20 steps of CGM at the beginning of the simulations; simulation R35.26-4 used 40 steps of CGM; and simulation R35.26-5 used 60 steps of CSM. Only in simulation R35.26-1 did the embedded grain totally disappear. Again, we observed the energy drop of the total excess energy curve, as shown in Figure 5.16. All the other simulations with $R_o = 35.26^o$, no matter how many CGM steps we used, had exactly the same potential energy curves, as shown in Figure 5.17. Even the total excess energies at the end of simulation are exactly same for these simulations. Compared with simulation R35.26-1, these simulations reached a metastable state in simulation and did not show further changes. The potential energies at different stages of the simulations are listed in Table 5.5, in which the energy right after equilibration is listed as the energy at "Beginning of simulation";

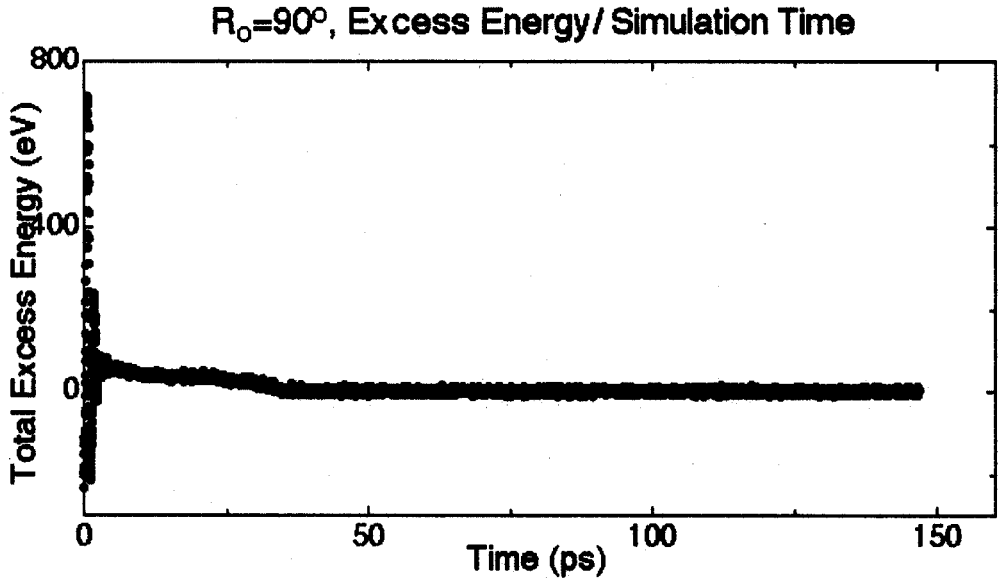

Figure 5.14: Potential energy of the system versus simulation time of simulation with $R_o = 90°$, with imbedded grain disappearing at an early stage of the simulation, around 35ps, which is about 35000 simulation steps.

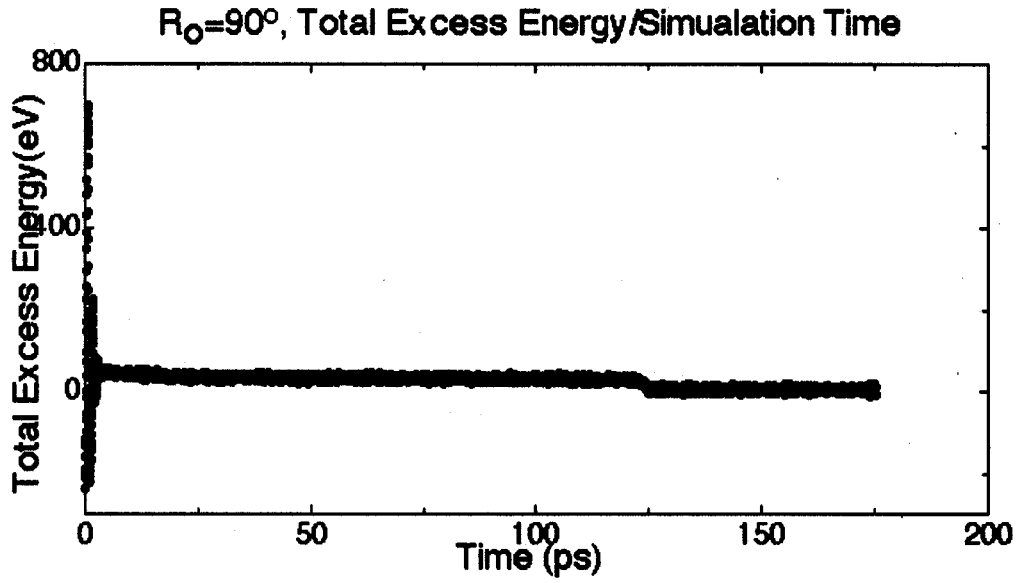

Figure 5.15: Sample plot of total potential energy of the system versus simulation time of simuatlion with $R_o = 90°$, with imbedded grain disappearing at the end of simulation.

energy at the end of the simulation, usually at the 150,000th simulation step, is listed as the energy at "End of simulation". If the embedded grain disappeared during the simulation, the energy before and after the disappearance is listed as "Before grain disappears" and "After grain disappears".

Table 5.5: Table for the average energy at different stages of the simulation for some sample simulations.

Simulation (ev)	CGM step	Beginning of simulation	Before grain disappears	After grain disappears	End of simulation
R35.26-1	20	-1.0375E4	-1.0420E4	-1.0448E4	-1.0448E4
R35.26-2	20	-1.0375E4			-1.0383E4
R35.26-3	20	-1.0372E4			-1.0383E4
R35.26-4	40	-1.0371E4			-1.0381E4
R35.26-5	60	-1.0374E4			-1.0382E4
R90-1	20	-1.0387E4	-1.0421E4	-1.0438E4	-1.0438E4
R90-2	20	-1.0393E4	1.0409E4	-1.0425E4	-1.0433E4
R45	20	-1.0373E4			-1.0376E4

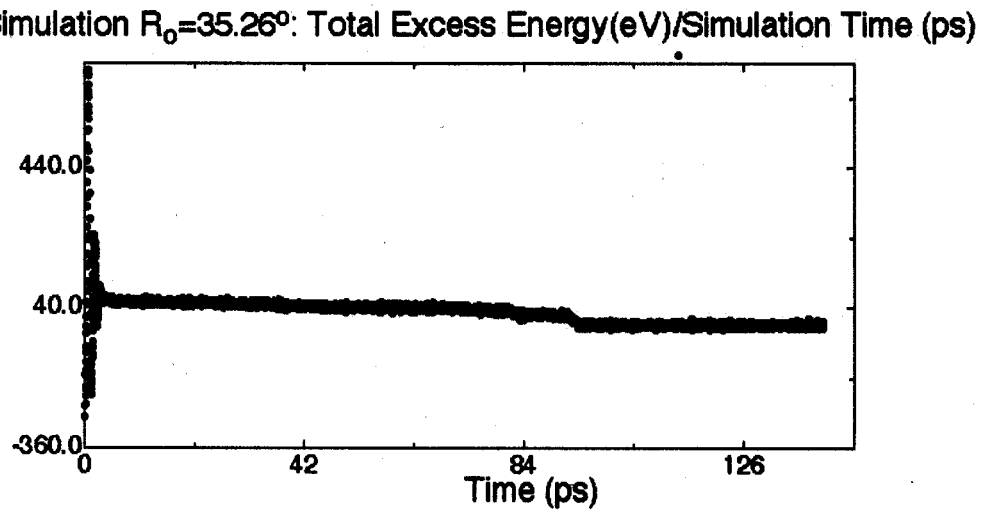

Figure 5.16: Sample plot of total potential energy of the system versus simulation time of simulation with $R_o = 35.26°$, with imbedded grain disappearing around the 94.5ps.

5.2.3 Discussion

All of the simulations experienced equilibration periods because we give random distribution to the velocities of the particles at the beginning of the simulation. However, with pair potential, after equilibration period we do not expect random distribution for the particles' velocities. The neighboring particles have interaction and their momenta are coupled. Therefore, before the momenta are coupled, systems experience equilibration periods.

After equilibration periods, the total energies did not change much. The reason is that only a small portion of the particles belong to grain boundaries in our systems. For example, for a system of 10,000 particles, only approximately 100 particles are located at grain boundaries. Therefore, after thermal balance is achieved, the number of the particles whose energies will change during the simulation is very limited. Moreover, according to our observation, the energy variation of the particles at grain

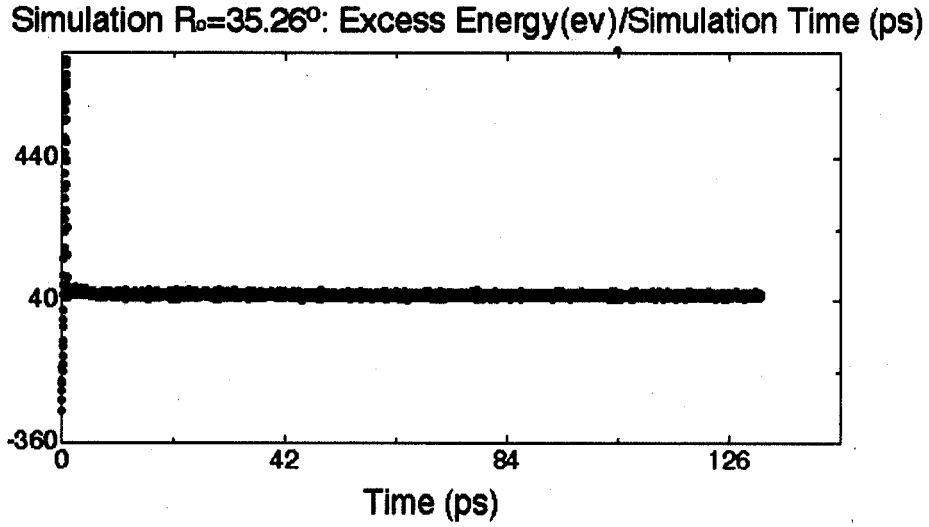

Figure 5.17: Sample plot of total potential energy of the system versus simulation time of simulation with $R_o = 90^o$, with imbedded grain disappearing around the 35ps.

boundaries ranged from -1.623ev to -1.2355ev for simulations at 500 degrees temperature. For a system that includes more than 10,000 particles, with only 100 particles on the grain boundaries whose energy varies within 1/4 of their energy, the variation of the potential energy will be only a small portion, less than 0.25% of the total potential energy. However, the energy variation in the thermal equilibration period is about 6% of the total potential energy. Therefore, compared with to the energy variation during the thermal equilibration period, the variation in the latter part of the simulation is too small to be observed on the diagram, unless the embedded the grain disappeared, and the excess energy of the system become zero, as shown in Figure 5.14 and 5.15. As shown in Table 5.5, the number of starting CGM steps does not have much influence on the simulation results. The simulations that started with different CGM steps had exactly same energy at the end of the simulations. Even the morphologies of the embedded grains are similar for these experiments. Therefore, the number of the CGM steps does not influence the simulation results.

We also found that energies dropped when the embedded grain disappeared. The embedded grains of the simulations with $R_o = 90^o$ disappeared at 36ps and 124ps, which corresponded to the energy drops on Figure 5.14 and 5.15. Similarly, for the simulation 35.26-1, energy dropped when the embedded grain disspeared. Therefore at the end of the grain shrinkage, the excess energies of the simulation change quickly. It takes about 2500 to 3000 simulation steps, which is about 2.5ps to 3ps, and the energy variation during this period is about one third of the total energy change. In the following chapter, we will explain more about what happened in our simulations when the energy dropped in the discussion of faceting and rotating of the grain, and the interaction between faceting and rotating of the grain.

5.3 Quantifying the excess energy associated with GBs

5.3.1 Results

In our simulations, we found that most of the embedded grain faceted to form planar grain boundaries. In our study, we calculate the contribution of the grain boundary excess energy to the total excess energy. Figure 5.18 shows a snapshot taken after 76000 simulation steps (76ps) of a simulation started with $R_o = 35.26^o$. Various grain boundaries are indicated with different colors. The red ones are the color grain boundary with $R = 35.26^o$; the blue ones are the grain boundaries with $\theta = 125^o$, $R = 35.26^o$; and the black ones are the grain boundaries with $\theta = 70^o$, $R = 35.26^o$. We measured the length of these grain boundaries in the fcc (110) plane and multiplied the thickness of the simulation cell, which is 9.7665 Å. We have already measured these grain boundary excess energy values: red grain boundaries have excess energy 5.225 ev/nm^2, area equal to 5.41 nm^2; blue grain boundaries have excess energy 5.758 ev/nm^2, area equal to 5.311 nm^2; and the black grain boundaries have excess energy 7.153 ev/nm^2, area equal to 2.823 nm^2. So the expected total grain boundary excess energy in this system at this moment is 79.05 ev. We also calculated the exact total

excess energy at this moment. We subtracted the energy of the single crystal with same volume from the measured the total energy of the system with grain boundaries, and got the excess energy of the grain boundaries equal to 80.9616 ev.

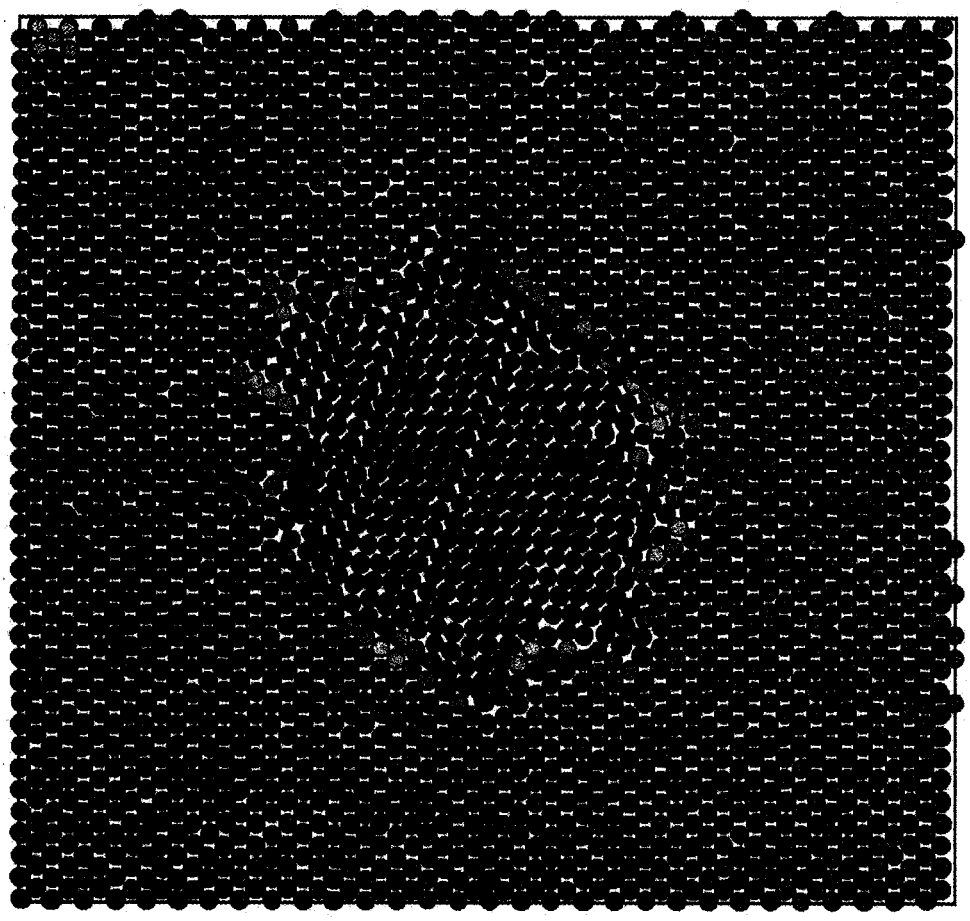

Figure 5.18: Snapshot of one simulation with original $R_o = 35.26^o$ taken after 76ps, with grain boundaries marked by color lines.

5.3.2 Discussion

In a system with a faceted embedded grain, the excess energy associated with the cylindrical grain boundary will be replaced by the sum of the energies of the planar boundaries and the sum of the energies of edges of each planar boundary as illustrated in equation 5.3.1

$$E_{excess} = \Sigma_i E^i_{GB} A_i + \Sigma_j E^j_{edges} \tag{5.3.1}$$

The edges in this bicrystalline structure are different from trijuntions in a polycrystalline system which involve three grains instead of two. It will be useful to find out the influences of these kinds of edges on the morphology of the bicrystalline structure. According to equation 5.3.1, the energy associated with such edges are not size dependent. For a big grain, with large grain boundary area, the energy of the edges contribute only a small portion of the total excess energy. Therefore, grain boundary excess energy dominates the total excess energy of the system, and the influence of edges on the morphology of the grain can be neglected. For a small grain, the energy of the edges might influence the morphology of the grain.

In our example, since the expected excess energy of the grain boundaries, calculated by equation $\Sigma_i E^i_{GB} A_i$, is approximately equal to the system excess energy calculated by $E_{gb} - E_{bulk}$, we can conclude that at least with this chosen embedded grain size, the excess energy of the system is approximately equal to the total grain boundary excess energy. Therefore, with embedded grain radius equal to 2.5nm, the contribution of grain boundary energy in total excess energy is almost equal to 100%. Thus any contribution of the excess energy of the edges is negligible.

Chapter 6

FACETING, GRAIN ROTATION, AND GRAIN SHRINKAGE MECHANISM

6.1 Results

6.1.1 Faceting of the grain

In our simulations, for the first 2ps after the simulation starts, the system experienced an equilibration period. Facets started to form at the beginning of the simulations, even during the equilibration period of the simulations. Facets changed their normal orientations and areas quickly in the first 2ps. After the equilibration period, the orientations of facet planes did not show quick and obvious changes.

Facets always formed at the locations of the low energy grain boundaries identified in our grain boundary excess energy measurements. Figure 6.1 gives a snapshot of the system with $R_o = 35.26^o$ and its DCP. In these two images, grain boundaries indicated by the same color are equivalent. Although the system did not reach the equilibrium state, and the shape of the grain was not even close to the symmetry shape it should obtain at equilibrium (for this misorientation value, the symmetry shape should include *mmm* symmetry), we found that facets formed mostly at the orientations indicated as SDE in the color symmetry study and at other low energy grain boundaries identified in grain boundary excess energy measurement section. And none of these low energy grain boundaries are CSL grain boundaries. More examples are given in Figure 6.2, which is the simulation of $R_o = 90^o$.

As we have already pointed out in Section 5.2.1, for the simulations with $R_o = 35.26^o$, in one simulation (R35.26-1 in Table 5.5), the embedded grain disappeared after 94500 simulation steps (94.5ps). The embedded grains for the other simulations started with

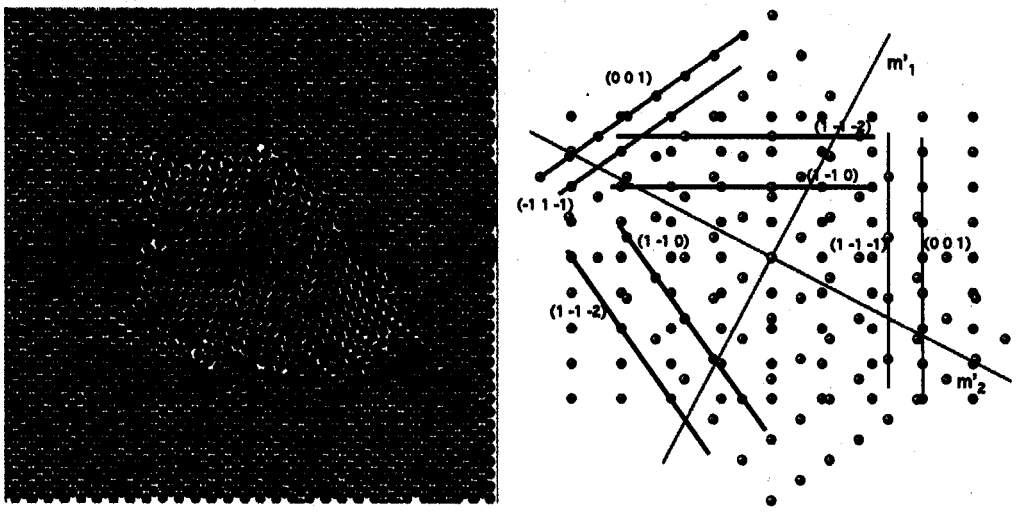

Figure 6.1: The snapshot taken in one of simulations with $R_o = 35.26^o$ and its DCP. Same grain boundaries are indicated by same colors on both the snapshot image and DCP.

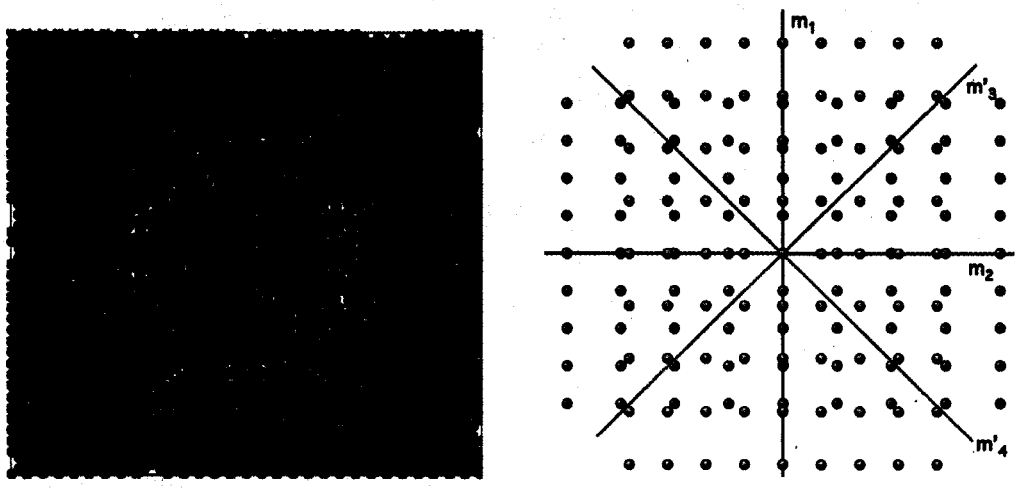

Figure 6.2: The snapshot taken in one of the $R_o = 90^o$ simulations and the DCP of it. We used the same color to indicate the same boundary on the snapshot and the DCP of FCC (110) with $R_o = 90^o$.

the same R_o did not disappear even over 150,000 simulation steps (150ps). For these simulations, we observed that the total potential energies of the system at later simulation stages were similar, as shown in Table 5.5. We also found that after 10,000 simulation steps (10ps), the embedded grains of these simulations were also similar both in volumes and morphology. Their facets even formed in the same orientations. Figure 6.3 shows two snapshots taken at the 10,000th simulation step (10ps) for two of our $R_o = 35.26^o$ simulations in which the embedded grain did not disappear. They were highly similar. Moreover, after these facets formed, the volume and the shape of the embedded grains did not change too much until we stopped the simulations around 150,000 simulation steps (150ps).

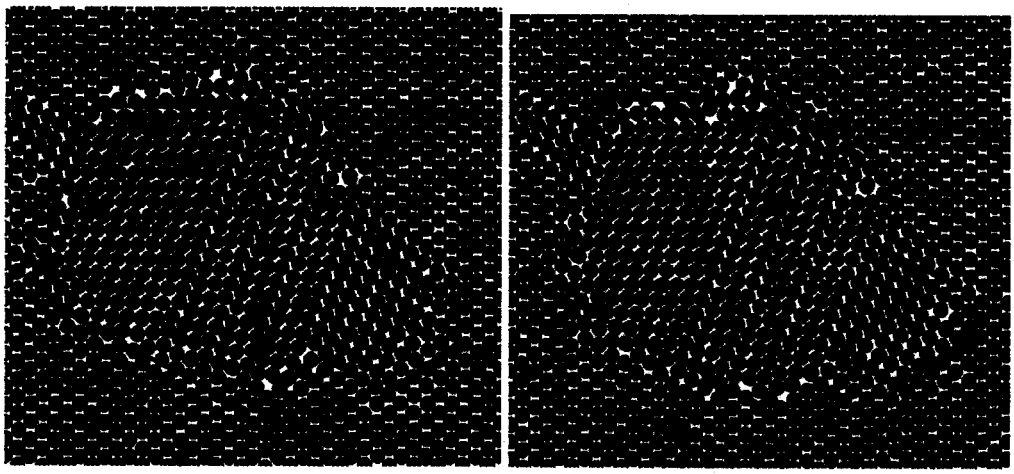

Figure 6.3: Similar shapes were achieved for these two different simulations with exactly same grain boundaries formed.

The results differed for another simulation with $R_o = 35.26^o$, during which the embedded grain disappeared. We also took the snapshot around the 10,000th simulation step (10ps) and marked the facets with colored solid lines as in its DCP pattern shown in Figure 6.4. The facets formed at the 10,000th simulation step (10ps) were quite different from the others. In this simulation, more $(1\bar{1}\bar{2})//(1\bar{1}0)$ grain bound-

aries were formed than in the others. Unlike the other simulations, after these facets formed, the embedded grain shrank continually, and disappeared quickly from the simulation system in less than 95,000 simulation steps, which was 95ps.

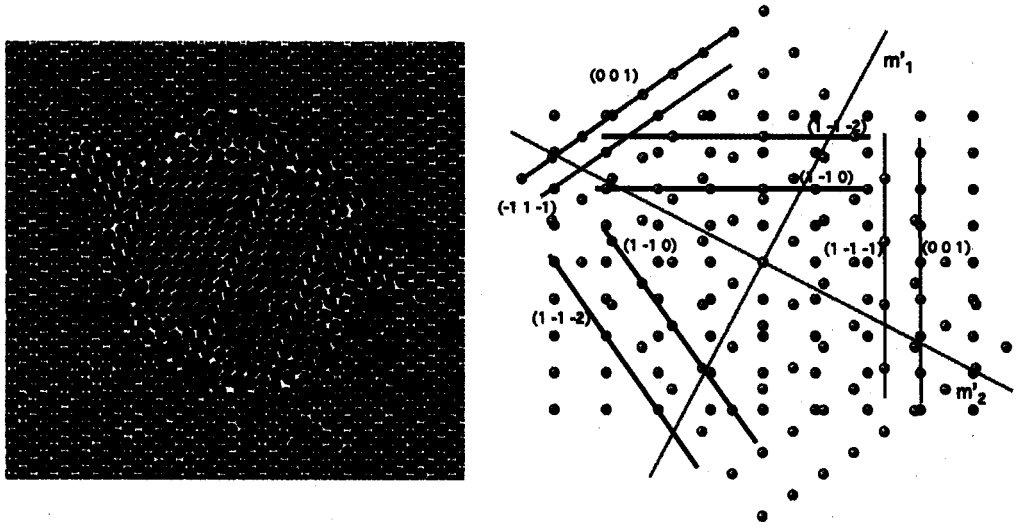

Figure 6.4: A snapshot also taken around the 10,000th step (10ps) for the simulation with continual shrinkage, compared with the DCP pattern of $R_o = 35.26^o$.

6.1.2 Interaction between stacking faults and grain boundaries

After we created the new colorizer of kSan, "**Color by Axis Angle**," we were able to distinguish the defects of the system more easily. We found many interesting phenomena by using this new visualization method. One of our main discoveries was that stacking faults formed during the evolution of the system, and that they were not independent defects, but influenced by the existence and the normal orientation of the grain boundaries. They were usually combined with dislocation or grain boundaries at the ends of the stacking faults.

Figure 6.6 is a snapshot taken at the 1000th step of a simulation with $R = 35.26^o$, which used constant temperature at 800 degrees. The particles are colored by the

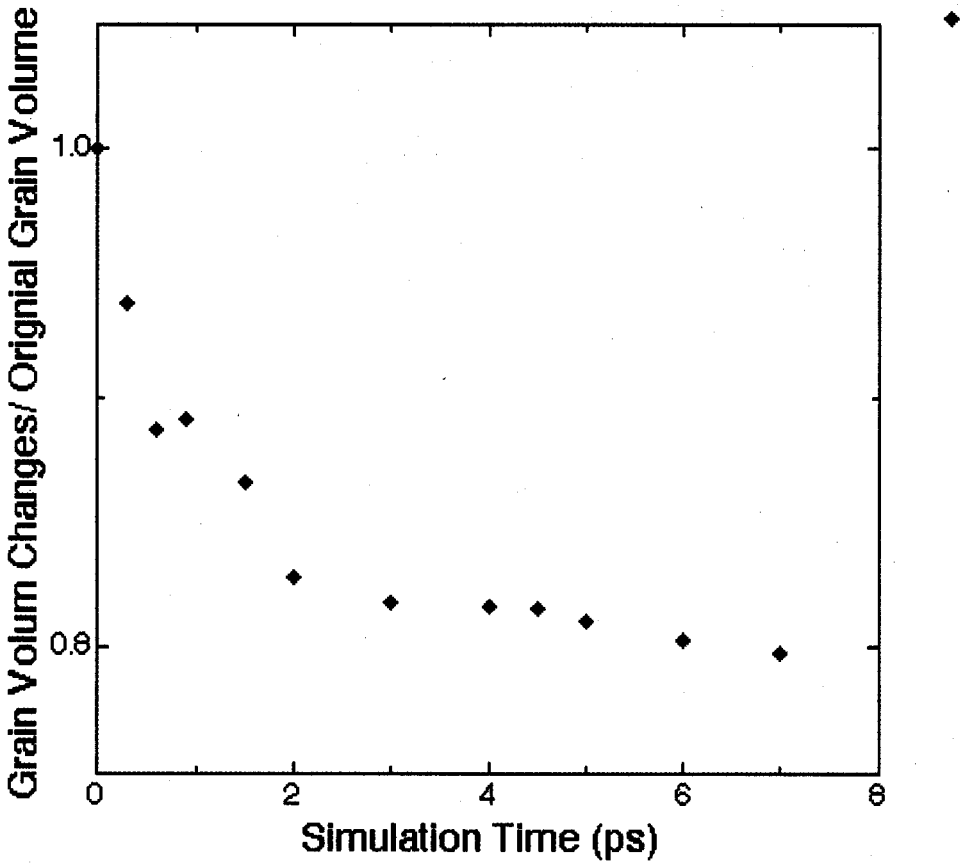

Figure 6.5: Volume percentage changes of the embedded grain during simulation.

"**Axis Angle Value**" function. As shown in Figure 6.6, it is much easier to identify the location and the type of the defects of the system by using this new colorizer. In Figure 6.6, facets have already formed at locations of low-energy grain boundaries. Shown in Figure 6.6, the one in the embedded grain is colored in blue and passes through the whole grain, and the other two in the enclosed grain are colored in green and only extend a short distance into the grain with dislocations at the end of them. All these stacking faults are along $< 112 >$ directions on the FCC (110) plane, which is in the (111) planes, and have at least one end attached to the grain boundaries. Compared with the snapshots taken at a later stage of the simulation, as shown in Figures 6.7 and Figure 6.8, we found that these stacking faults did not disappear during the evolution of the simulation; the number of stacking faults increased while the excess energy of the system decreased. They first started at the grain boundary with a dislocation at the end of each stacking fault, and grew with the dislocation moving across the embedded grain. Each dislocation has Burger's vector equal to $\frac{1}{2} < 112 >$. In simulation, we could clearly see the growth of the stacking fault. In Figure 6.7, a snapshot taken in the middle of the simulation, a second stacking fault in the embedded grain starts to form at the upper part of the embedded grain. Figure 6.8 is another snapshot showing the second stacking fault fully grown and approaching the other side of the embedded grain.

We also did a simulation with a much bigger embedded grain and let it have a capsule shape instead of a circular one in the common (110) plane. Figure 6.9 is a snapshot taken after 25000 simulation steps. The longest grain boundaries are those that let the inside grain's $(1\bar{1}\bar{2})$ plane to be parallel to the surrounding grain's $(1\bar{1}\bar{0})$. We can see that this time, both the embedded grain and the surrounding grain lack stacking faults that extend across the whole grain. With this structure, we also clearly observe that stacking faults only form at certain grain boundaries. In this system, even though $(1\bar{1}\bar{2})//(1\bar{1}\bar{0})$ grain boundaries cover a large area, only the color symmetry grain boundaries located at the corner of the embedded grain are able to

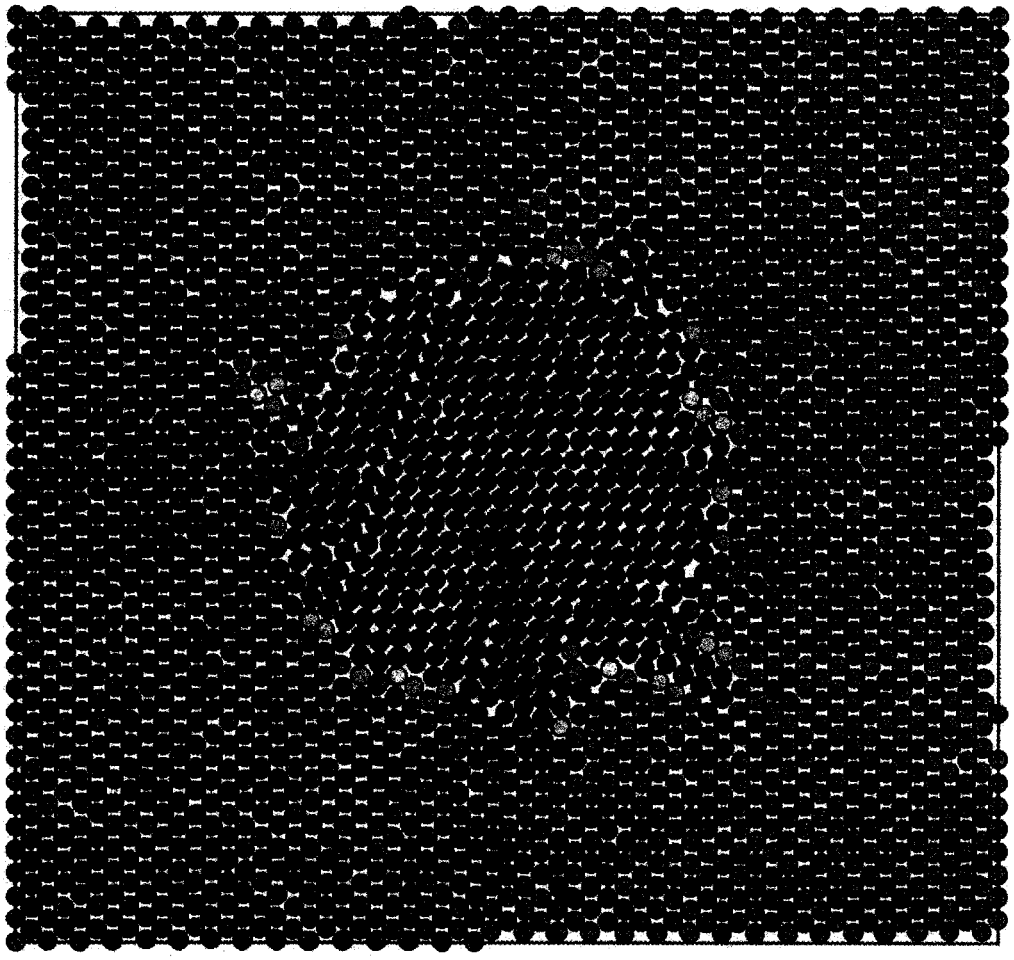

Figure 6.6: A snapshot taken after 1000 steps for the rotation with $R_o = 35.26^o$; the stacking faults exist both in the embedded grain and the enclosed grain, with only one direction for each grain.

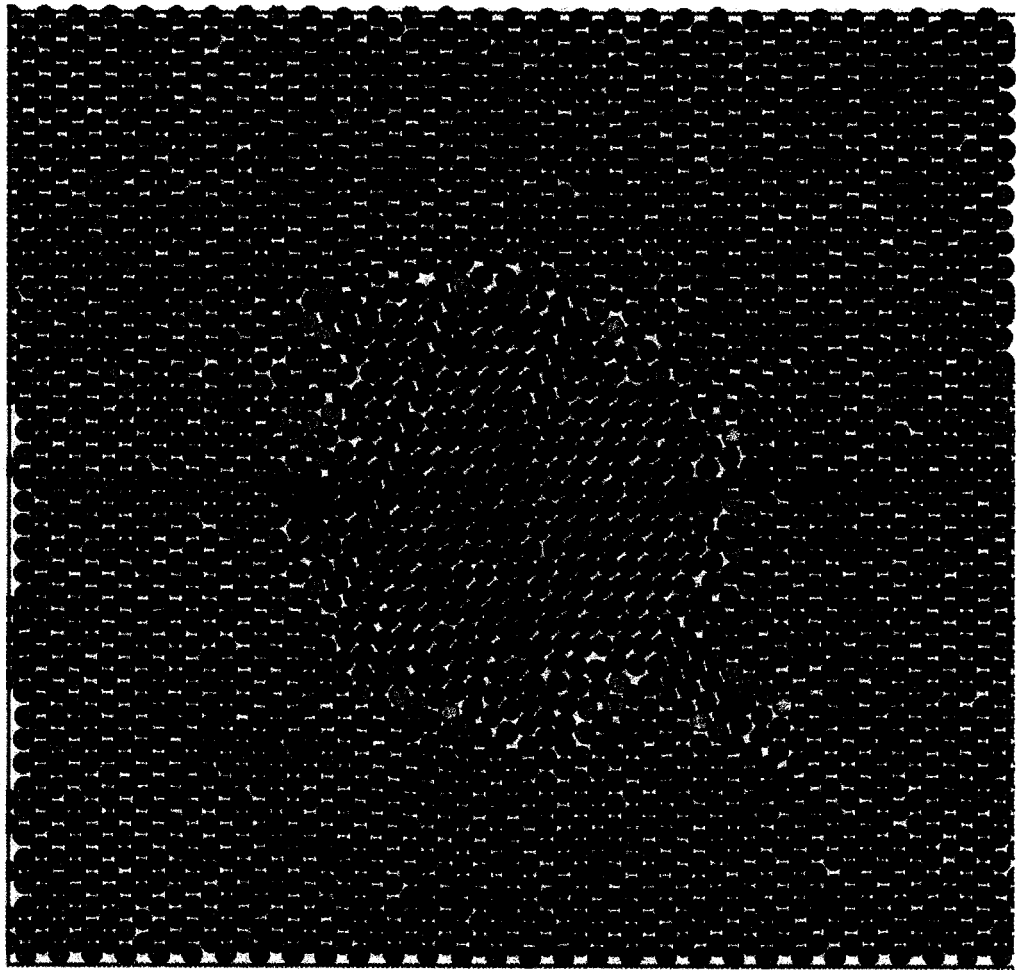

Figure 6.7: A snapshot taken after 5000 steps for the simulation with $R_o = 35.26°$; Another stacking fault with a dislocation at the end starts forming and grow through the movement of the dislocation

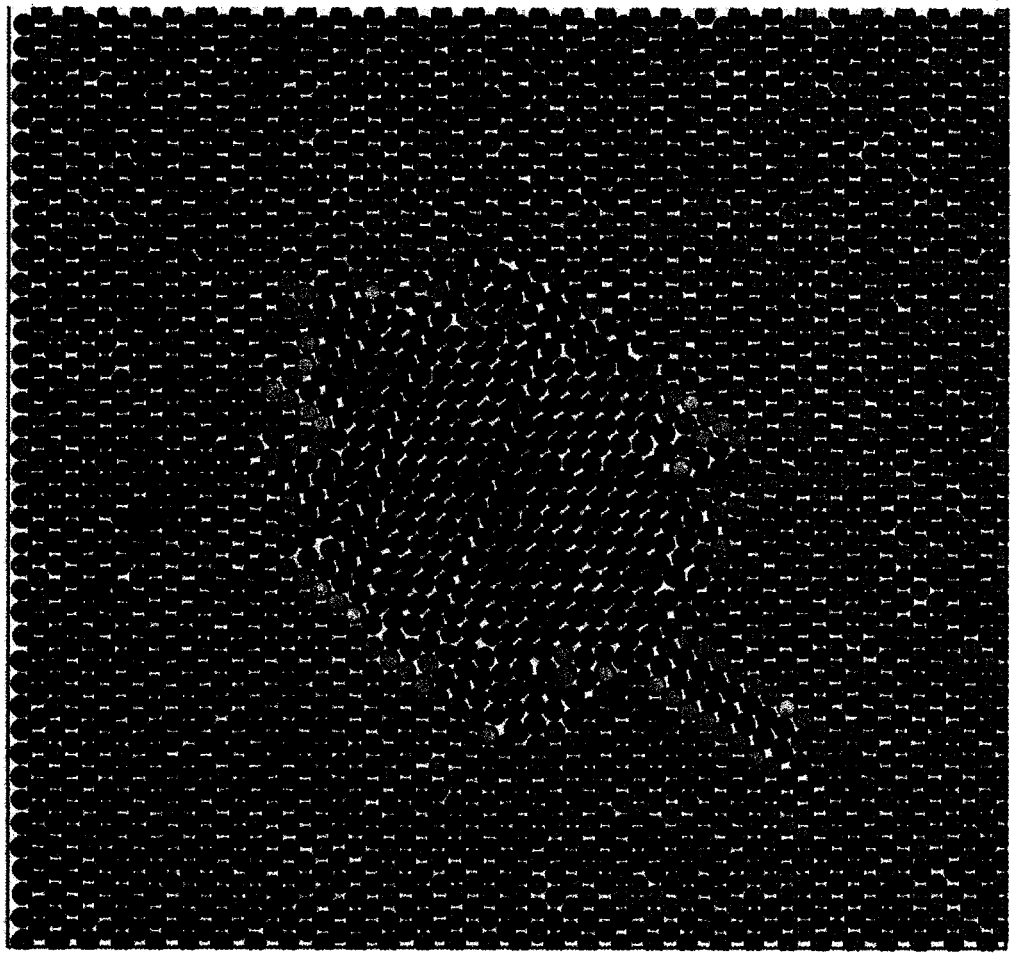

Figure 6.8: A snapshot taken after 26000 steps for the simulation with $R_o = 35.26^o$; the stacking faults exist both in the embedded grain and the enclosed grain, with only one direction for each grain.

initiate the formation of stacking faults.

We manually selected the particles and calculated the average energy per particle at four locations: inside the grain far from the grain boundaries, inside the stacking faults, on the grain boundary that is not attached to a stacking fault, and on the grain boundary that is attached to a stacking fault.

Table 6.1: The average energy per particle in different areas of the structure with stacking faults attached to the grain boundaires.

ev/particle	Inside Grain	In Stacking Fault 1	Inside Stacking Fault 2	On grain boundary without Stacking Fault	On grain boundary with Stacking Fault 1	On grain boundary with Stacking Fault 2
energy/particle	-1.3219	-1.3438	-1.3157	-1.2591	-1.3628	-1.3058
number of particle	50	13	16	27	25	21
variance	9.51E-3	7.94E-3	1.96E-2	1.67E-2	1.67E-2	7.65E-3

As shown in Table 6.1, the energy/particle in the stacking fault was almost equal to that obtained inside the grain and distant from the grain boundary, and the energy/particle on the grain boundaries with stacking faults was lower than the one without stacking faults. In one case we even found that the energy/particle was lower than the one we obtained inside the grain.

In some cases, these stacking faults connect with each other and make the misorientation of part of the grain change as shown in Figure 6.10. This simulation started with $R = 45^o$, and part of the embedded grain changed its color to green with increasing of the number of the stacking faults.

6.1.3 Grain rotation

Grain rotation occurred in most of our MD simulations. Some grains rotated more than others. Simulations with $R_o = 35.26^o$ and $R_o = 90^o$ are the most stable initial misorientations, while the simulations that started with other R_o values, such as $R_o =$

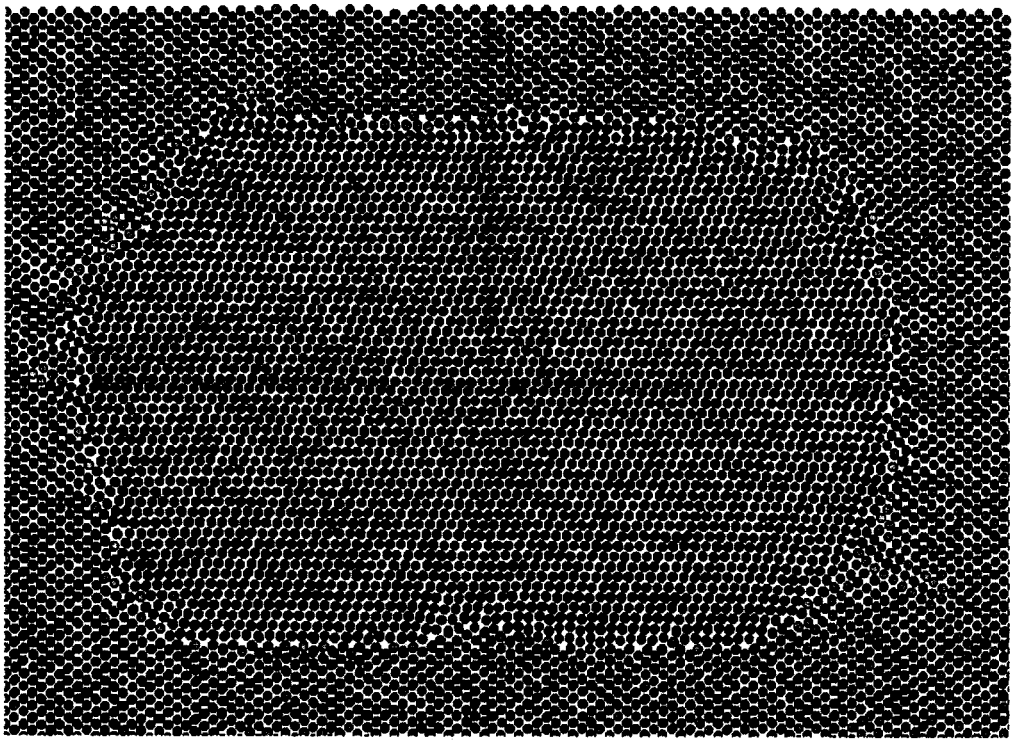

Figure 6.9: A snapshot taken after 25000 steps for the simulation with $R_o = 35.26^o$; the embedded grain has a capsule shape in the cutting face, instead of a round one. The stacking faults exist both in the embedded grain and the enclosed grain, still with only one direction for each grain.

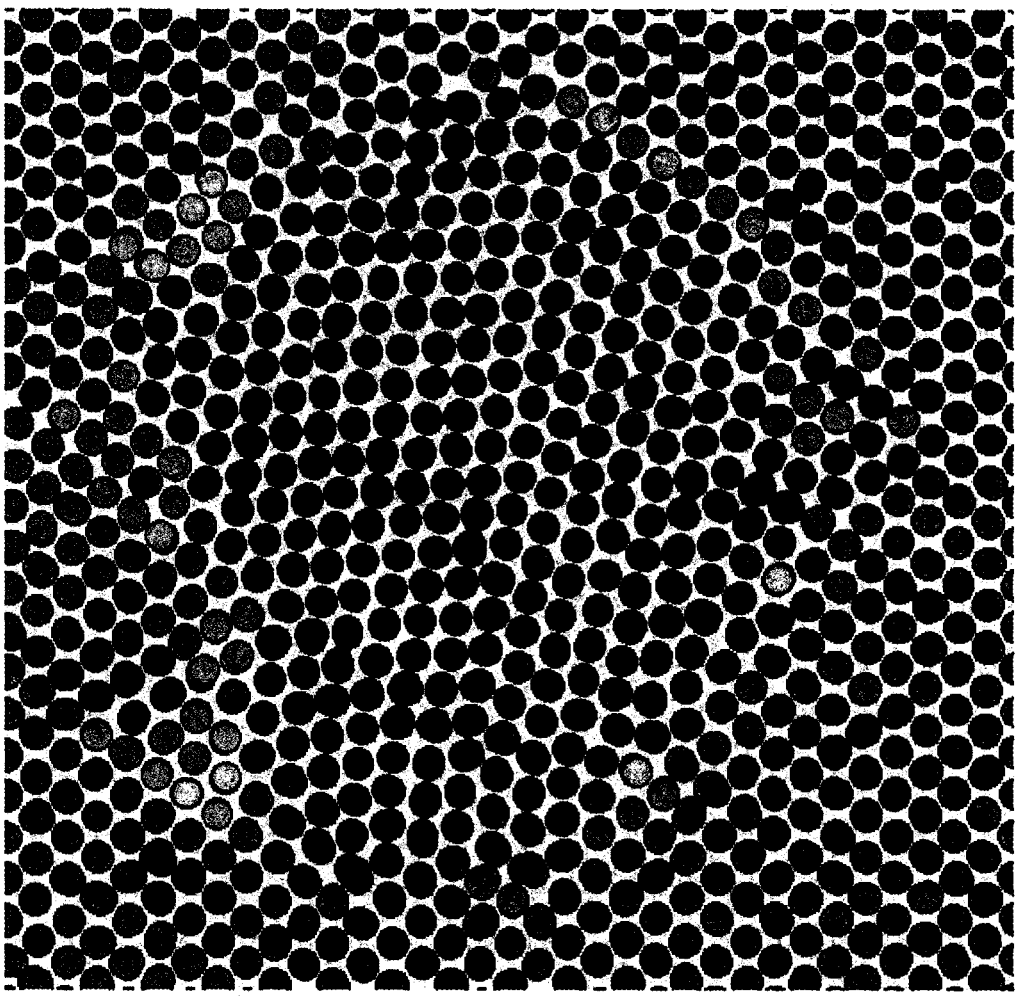

Figure 6.10: A snapshot taken after 53000 simulation steps of a simulation with $R_o = 45^o$.

60^o, $R_o = 70^o$, and $R_o = 45^o$, showed more rotation, especially in the early stages of the simulations. We observed that the rotation usually had an oscillating pattern; we rarely observed continuous rotation towards one direction, but rotation alternated clockwise and counterclockwise. We call this type of rotation oscillating rotation.

After we developed the algorithm for calculating the misorientation of the grain to which a particle belongs, we were able to quantitatively record the rotation angle of the embedded grain. We selected particles at the center of the embedded grain, and took the average axis angle value of these selected particles at every 20 simulation steps, which was about 0.02ps. Figure 6.11 plots the rotation angle of the embedded grain versus simulation time with $R_o = 45^o$, for the first 17ps. We selected 50 particles in the center of the embedded grain for the data recording and took their average values. Rotation started at the beginning of the simulation. For the simulation starting with $R_o = 45^o$, the misorientation angle, R, varies between 41 to 48 degrees. Figure 6.11 shows that the oscillating rotation of the grain lasted during the whole simulation before we stopped it. Moreover, the magnitude of the rotation angle decreased during the simulation. Even for the first 2ps of the simulation, the initial equilibration in which the total energy and the temperature of the system changed greatly, the rotation pattern and the magnitude of the rotation angle in this period did not differ much from the rotation occurring later. Simulation with $R_o = 60^o$ had similar patterns, with the misorientation varying between 55 and 63 degrees.

Since we call this type of rotation oscillating rotation, we investigate if the changes of the rotation direction is periodical. We counted the simulation time between the adjacent highest point and lowest point for R value, and found that it usually took 0.25-0.3ps from positive peak to the negative peak. The time between peak to peak was almost constant. Therefore, we can say the rotation was oscillating.

In our simulations, we found that the magnitude of the rotation was influenced by the average grain boundary energies of the facets. In our grain boundary excess energy calculations, we found that the energy of the color mirror plane grain bound-

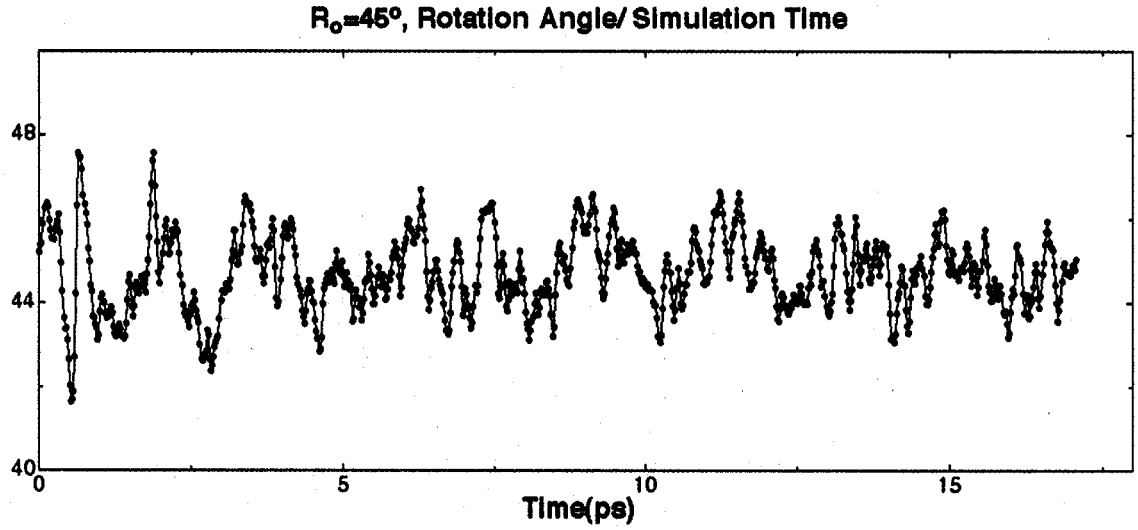

Figure 6.11: Change of the rotation angle with simulation time for the simulation with $R_o = 45^o$; data were taken during simulation at every 0.02ps.

ary of $R = 70^o$ was similar to other color mirror plane grain boundaries in the FCC (110)//(110) system. However, the general grain boundaries at this misorientation have much higher energy; almost two to three times that of its color mirror plane grain boundary. In the simulation with $R_o = 70^o$, we observed that grain boundaries located on color mirror planes are formed quickly in the equilibration period. After 2ps, the embedded grain had a rectangular shape with facets formed all in color mirror planes, as shown in Figure 6.12 and Figure 6.13. We also recorded the rotation angle of selected particles versus simulation time. In this experiment, we selected 60 particles and recorded their average rotation angles for about 30ps, as shown in Figure 6.14. The range of the data was much bigger for this simulation; R ranged between 25 to 70 degree at the beginning of the simulation and between 55 to 70 after 15ps.

However, we did not observe the embedded grain rotating in the movie as large as indicated in our data, which showed rotation of 50 degrees. We plot the distribution

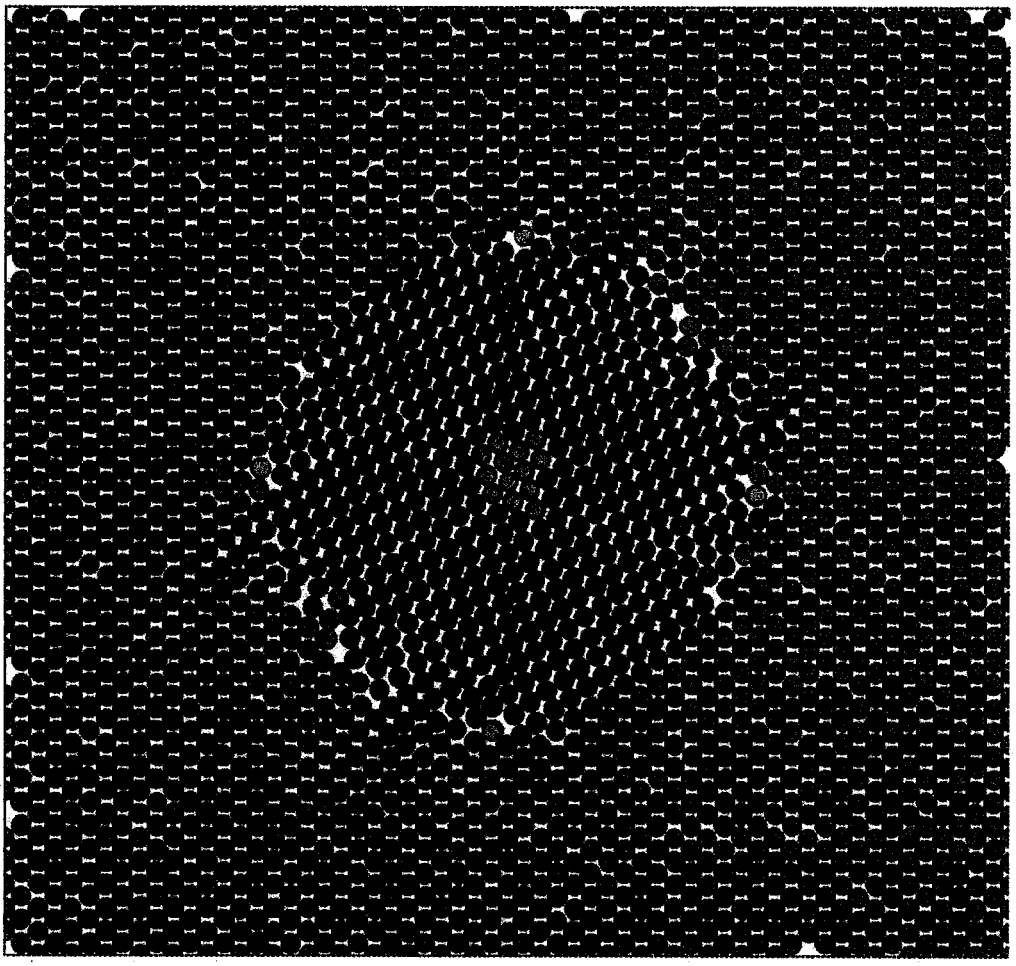

Figure 6.12: Snapshot taken before simulation with $R_o = 70^o$.

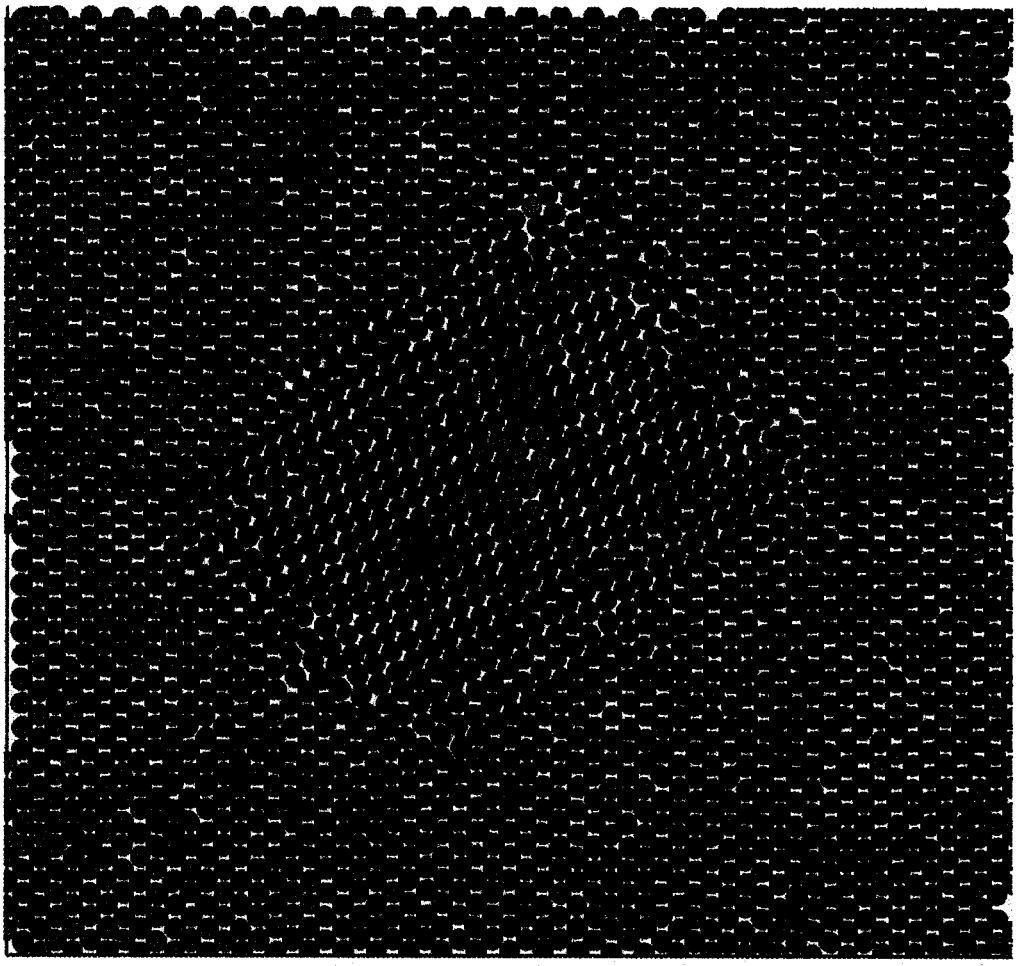

Figure 6.13: Snapshot taken after 2ps of simulation with $R_o = 70°$.

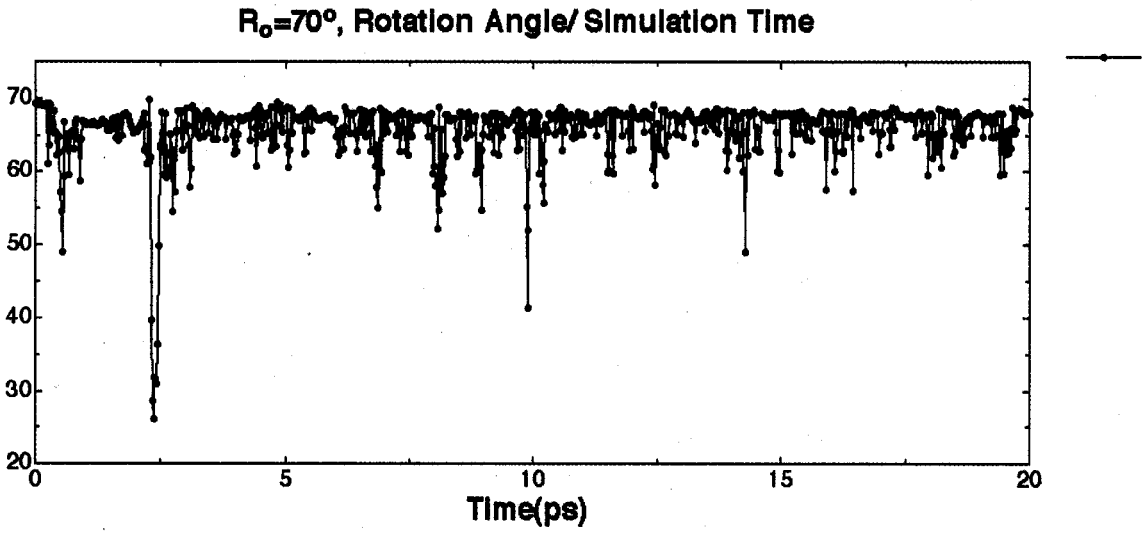

Figure 6.14: Change of the rotation angle with simulation time for the simulation with $R_o = 70°$; data were taken during simulation every 0.02 ps.

data for the selected particles in Figure 6.15. It shows that several particle's rotation angle values are much lower than 70 degrees and give an incontinuity to the average values of rotation angle. The number of these particles are limited. In Figure 6.15, only 10 data points are lower than 50 degrees among a total of 676 data points. This occurs because of our '**Axis Angle Value**' calculation agorithm. We explained in section 4.3 that in our angular value calculation, we give cut off ranges for the distance and angle of the particles which allow us to use the algorithm even at high temperatures. We only calculate particle's axis angle value if the surrounding particles have 2 fold symmetry. However, if particles shift away from their equilibrium positions too far and are out of the cut off range, the neighboring particles do not have 2 fold symmetry, and the particles are not considered to be inside of the structure. Therefore, their axis angle value will always close to zero. The 10 data points in Figure 6.15 which are much lower than 70 degree are from the particles that are too active and lose their 2 fold symmetry in their movements. After eliminating these 10 data points,

the rotation range of simulation with $R_o = 70^o$ is about 12 degrees.

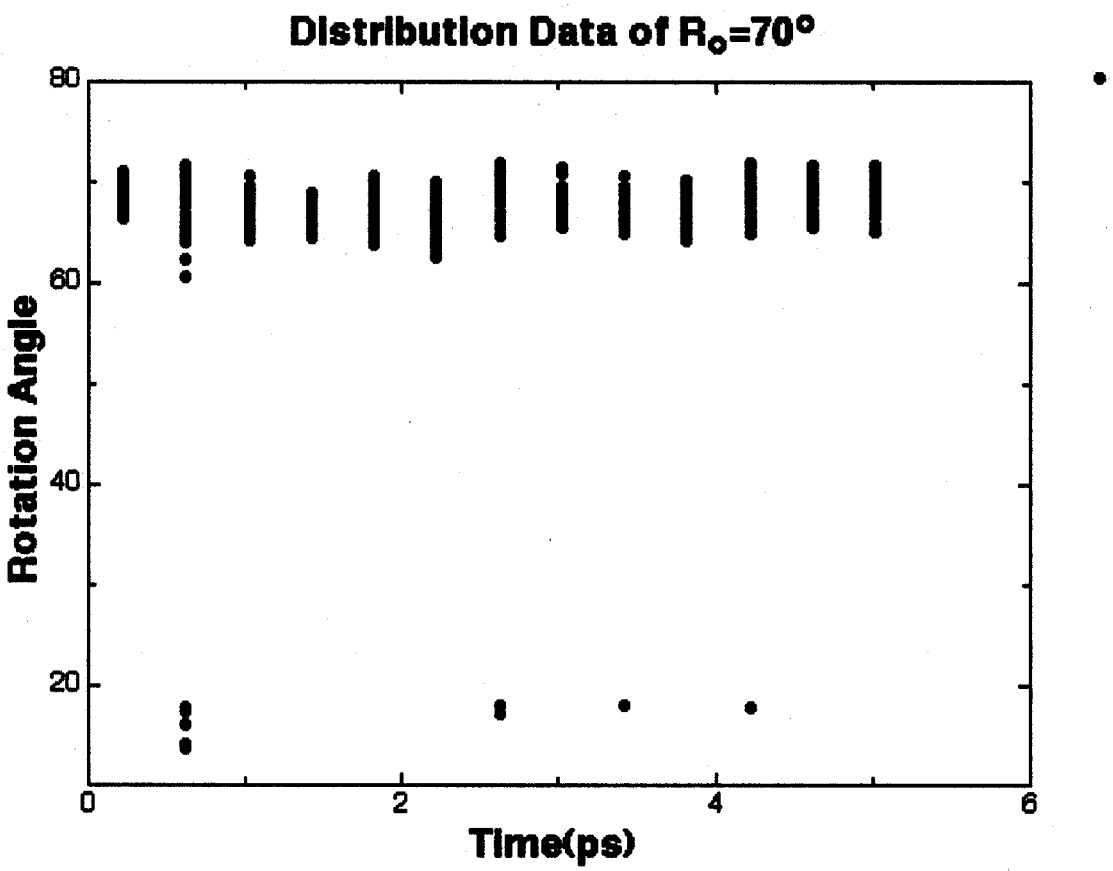

Figure 6.15: Distribution of the angular values taken at every 0.5ps for all selected particles for the simulation with $R_o = 70^o$.

Compared with these simulations, those started with $R_o = 35.26^o$ and 90^o are very stable. We did not observe rotation for the systems with $R_o = 35.26^o$ and $R_o = 90^o$. As shown in Figure 6.16, the rotation angle scale is smaller, only between 34.5 and 37 degrees in the equilibration period and between 34.5 to 36.5 after that. Simulations started with $R_o = 90^o$ ranged between 89 to 92 degrees, as shown in Figure 6.17. Moreover, the magnitude of the rotation did not obviously differ during and after the equilibration period for both simulations started with $R_o = 90^o$ and $R_o = 35.26^o$. The

data points were also roughly symmetrical, which means that rotation angle values were vibrating around the starting misorientation value.

We tested how thermal effects influenced our rotation calculation data by recording the value of R in the simulation of a single crystal, and found that the value of R ranged between 59 and 61 degrees. We also tested the distribution of our angular values during the simulation, and found that the rotation angle distribution at this temperature after equilibration was between 3 degrees. We also tested the angle value distribution for a single crystal by selecting some of the particles in the center of a single FCC structure and recording the average angle value. We found that the R value for single crystal ranged between 59 to 62 degrees, as shown in Figure 6.18. This shows that the precision of R value measurement is about 2 - 3 degrees. Table 6.2 lists the range of rotation for different R_o values.

Table 6.2: The ranges of the rotation after equilibration for simulations started with different R_o

R_o	Rotation Range After Equilibration
90^o	89-92^o
35.26^o	34.5-36.5^o
45^o	$42 - 48^o$
69^o	$55 - 63^o$
70^o	$55 - 70^o$
0^o	$59 - 62^o$

In Figure 6.19 we give the distribution data of rotation angles of all selected particles versus simulation time. We can see that distribution of the angular value at $R_o = 90^o$ does not change much during the simulation.

We marked the time periods during which faceting and rotation occur on a plot of rotation angle versus simulation time in the top image of the Figure 6.20, and marked

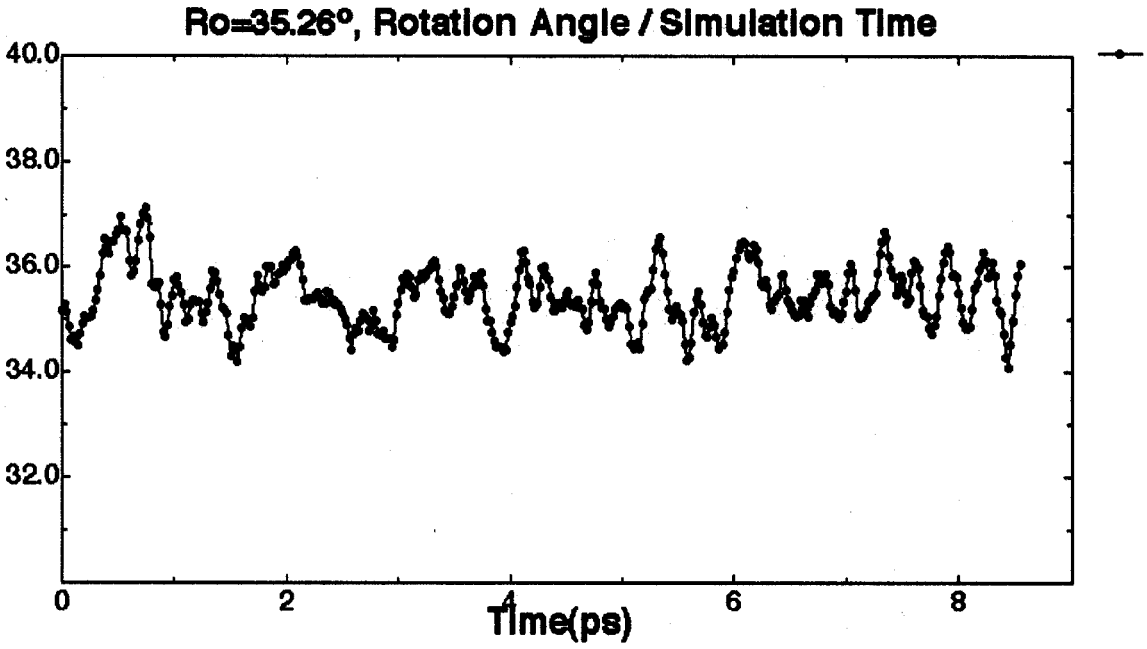

Figure 6.16: Change of the rotation angle with simulation time for the simulation with $R_o = 35.26^o$; data were taken during simulation every 0.02ps.

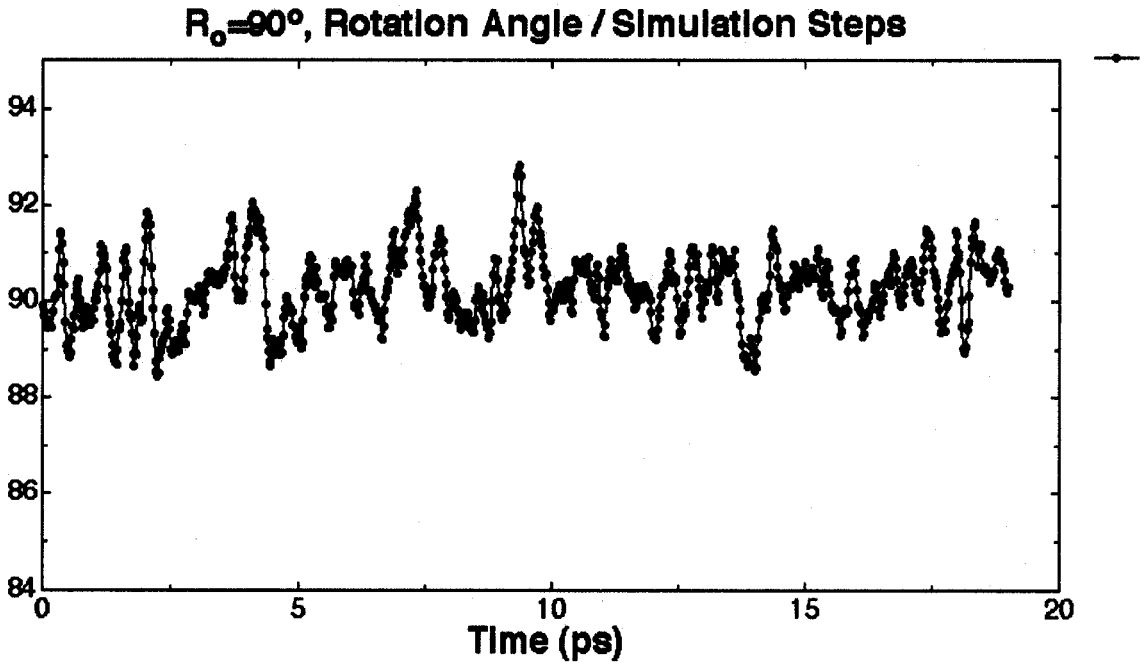

Figure 6.17: Change of the misorientation angle with simulation time for the simulation with $R_o = 90^o$; data were taken during the simulation at every 20 steps.

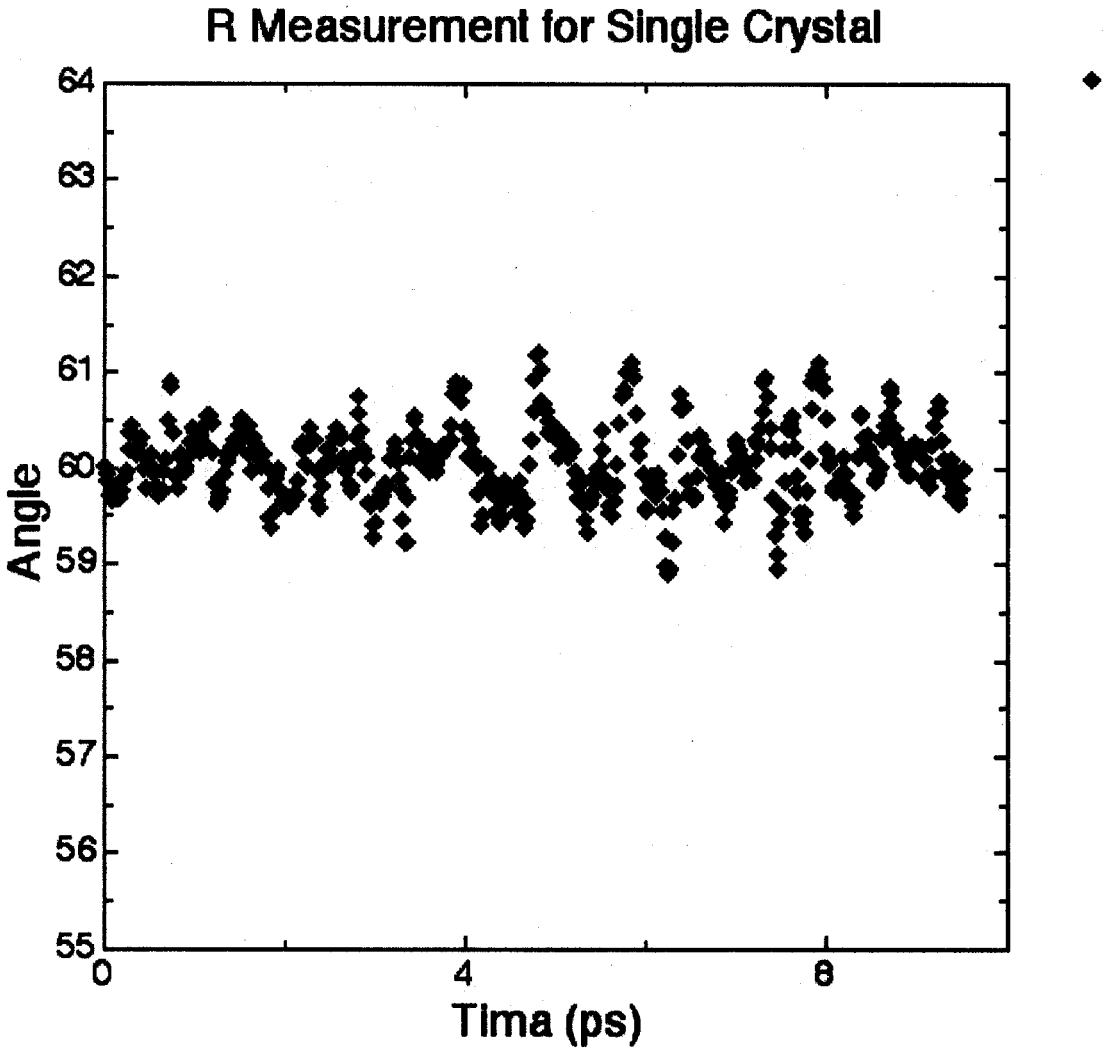

Figure 6.18: R value versus time for single crystal which has no rotation.

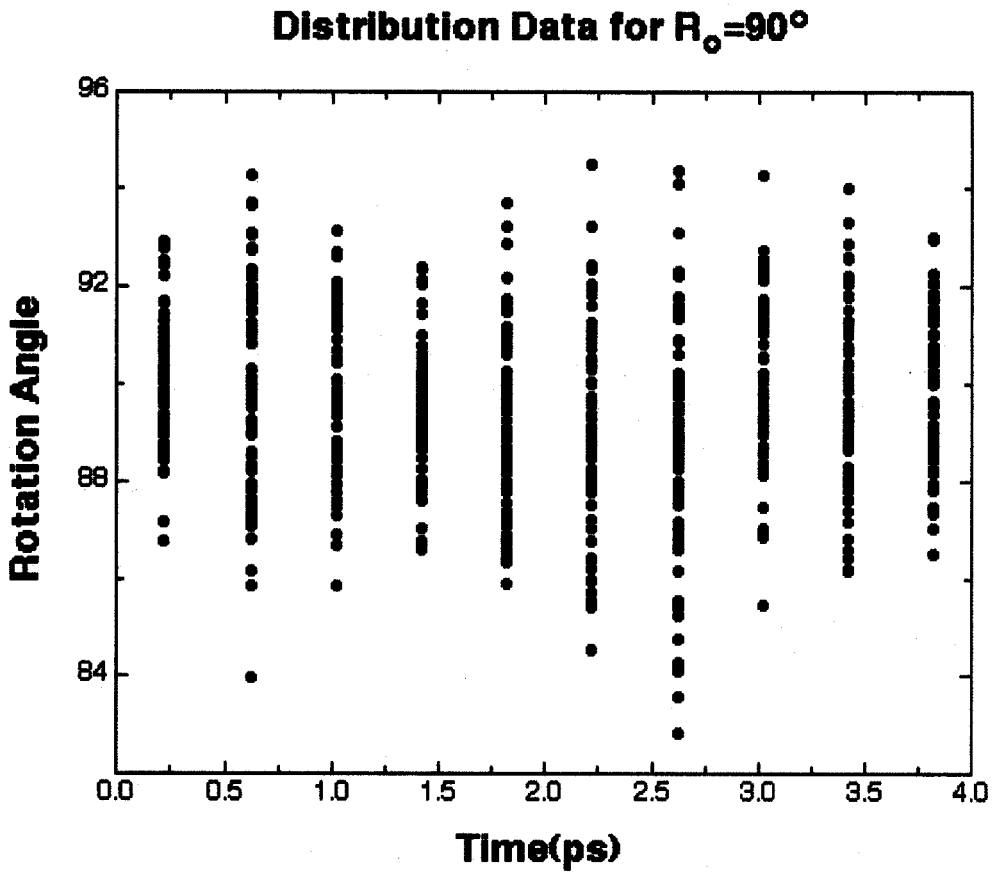

Figure 6.19: Distribution of the angular values taken at every 0.5ps for all selected particles for the simulation with $R_o = 90°$.

the equilibration period on the bottom image. Facets formed in the first 2ps of the simulation while rotation lasted much longer.

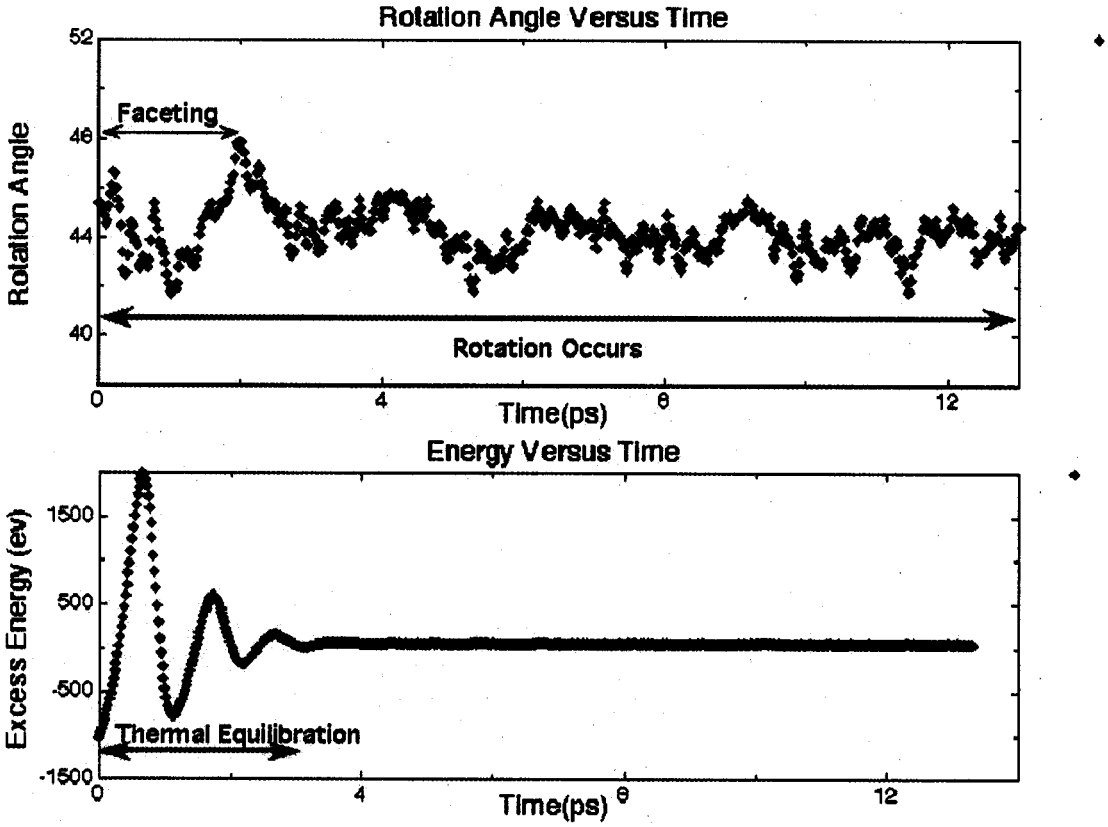

Figure 6.20: Facet formed in 2ps of the simulation while rotation lasts much longer.

In addition to this type of oscillating rotation in the early stages of the simulation, another type of grain rotation was observed in our simulations which had more impact on the energy of the system. Part of the embedded grain changed its misorientation abruptly to achieve the same orientation as the surrounding grain, and the volume of the embedded grain was abruptly reduced. As shown in Figure 6.21, a small portion of the grain suddenly changed its misorientation and became part of the surrounding grain. The change of the part of a grain's orientation occurred in less than 800 simulation steps. We found that the energy drop we discussed in Section

5.3 corresponded to this type of abrupt change in orientation. In simulation R35.26-1 (Figure 5.16), for example, the total energy dropped from about -10400 ev to -10420 ev around the 82000th simulation step. In the movie, the abrupt change in orientation shown in Figure 6.21 occurred right around the 82000th simulation step. After this change of orientation, the grain shrank continuously and quickly, and disappeared after another rotation of the whole grain around the 94500th simulation step, with the total energy suddenly dropping from -10420 ev to -10450 ev. Then, the whole system became a single crystal and the total energy remained stable.

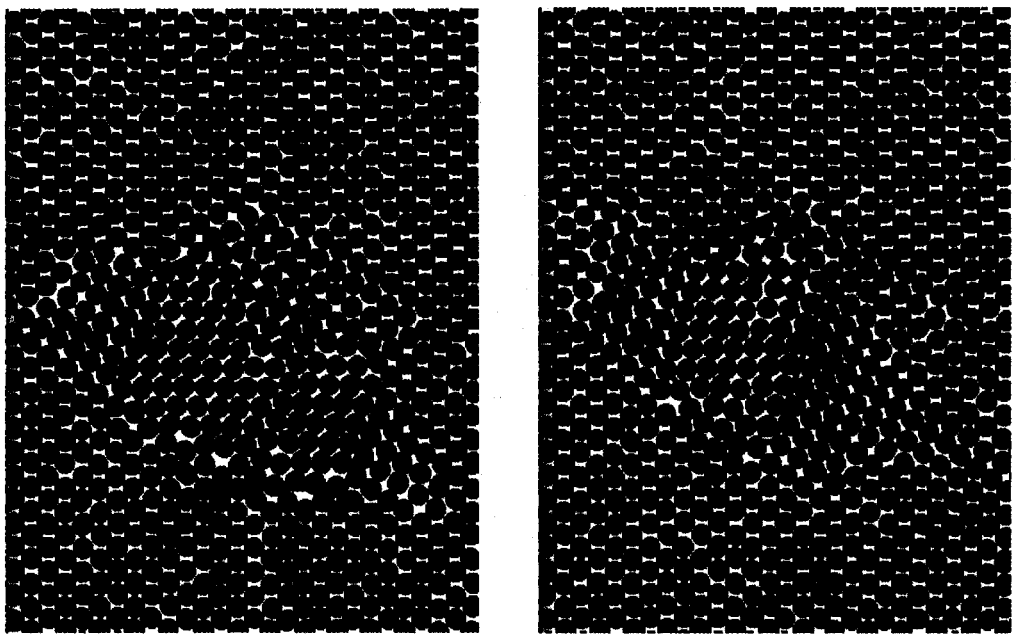

Figure 6.21: These two snapshots were taken right before and after rotation in one of the $R_o = 35.26^o$ simulations, which corresponds to the first energy drop on Figure 5.16.

We always observed this type of rotation happened close to where dislocations existed. During the change of orientation, the particles moved along the glide planes of the FCC system, which were {111} planes. As shown in the left graph of Figure 6.22, two dislocations outlined by red circles were located at the boundary before rotation.

Both dislocation lines were in the [110] direction with Burger's vector $\frac{1}{2}\langle 1\bar{1}0\rangle$. During simulation, the small plane of particles between these two dislocations slid along the $[\bar{1}12]$ as marked on the right graph in red. At the same time, several planes slid down along the $[1\bar{1}2]$ direction as marked by the black arrows, and made the orientation of this part of the grain the same as that of the surrounding grain. We still call it rotation because it corresponds to change of the misorientation between two grains. This type of rotation often occurs at the later stage of the simulations. Most of the systems in which the embedded grain disappeared experienced this type of rotation, which is always associated with an energy drop on the plot of potential energy as a function of time, as shown in Figures 5.15 and 5.14.

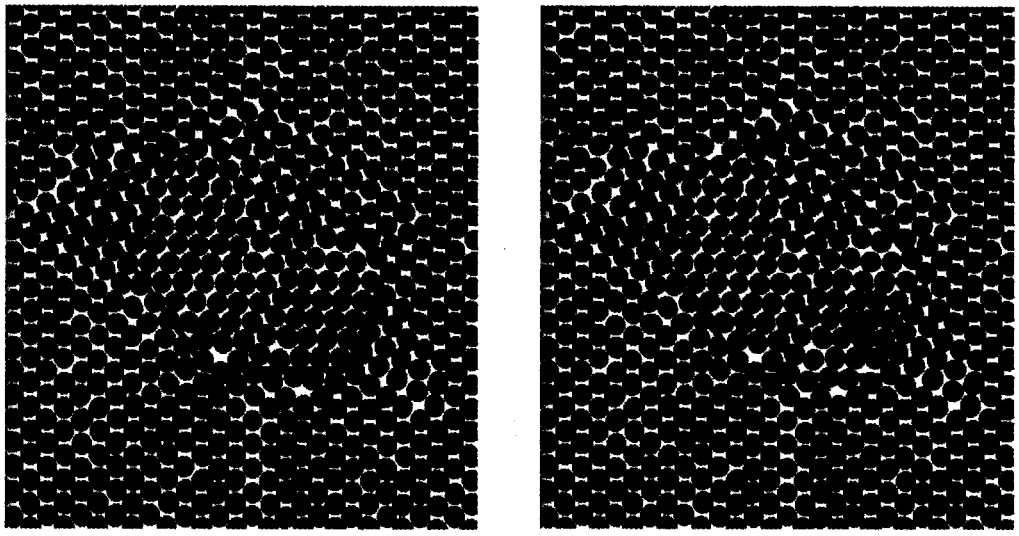

Figure 6.22: Snapshots to show how dislocation interacts with plan glide to change the orientation of part of the grain.

The example given below happened in one of our simulations with $R_o = 45^o$. We found that part of the embedded grain rotated during the later stages of simulation and caused the embedded grain to divide into three grains, as shown in Figure 6.23. Even though the grain boundary area increased as more grain boundaries developed

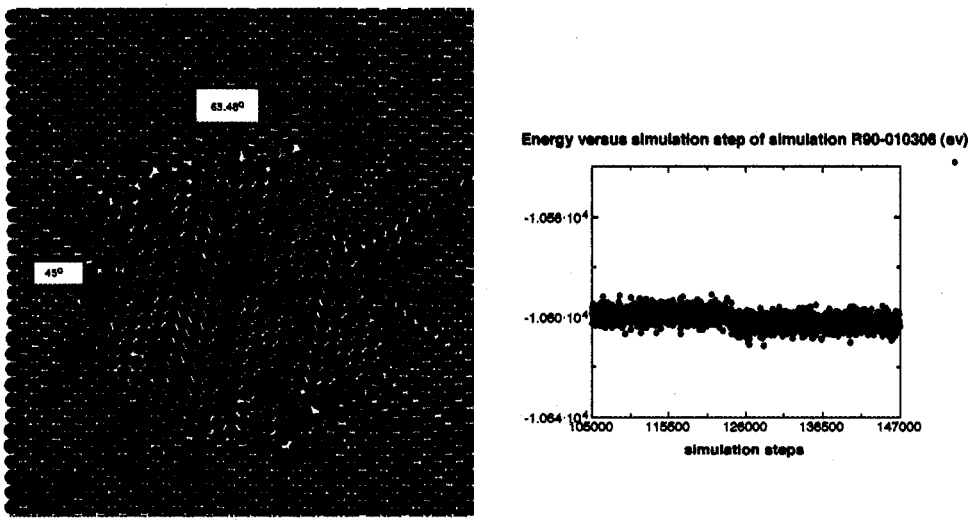

Figure 6.23: At the later stage, the embedded grain of simulation R45-101905 divided into three grains. Even though more grain boundaries were created in the system, the total potential energy decreased, as shown in the plot on the left.

in the system after this rotation, the total potential energy decreased as shown in the plot on the right. The right image of Figure 6.24 gives the DCP with color grain boundaries indicated by the solid red lines. On the left image, we can see that the grain boundaries surrounding the embedded grain are not all low energy. Here, we use yellow color to represent the grain boundaries that are not low energy grain boundaries. On this snapshot, we observed more dislocations and extra atomic space in the area outlined by pink circles. These extra spaces on the grain boundaries made it possible for part of the inside grain to glide down.

After the change of the orientation, the inside grain was divided into three grains: a grain with $R = -63.48^o$ was added to the system, as shown in Figure 6.23. A trichromatic pattern (TCP) illustrates the system with three grains and all special grain boundaries marked, as shown in the right image of Figure 6.25. The left image presents the snapshot taken right after rotation; all the grain boundaries are marked with the same color as the special grain boundaries on the TCP. We measured the area

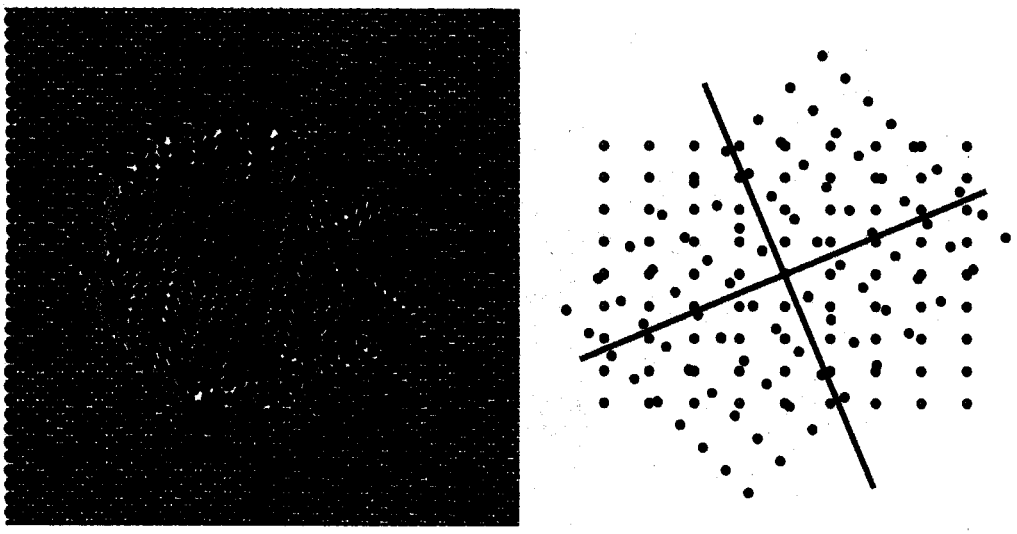

Figure 6.24: Before the rotation, the grain is surrounded by mostly high-energy general grain boundaries; the place where rotation occurred had more dislocations and greater excess volume than did other sites.

of each facet by measuring the length of the facets in the common FCC (110) plane and the thickness of the simulation cell in the common [110] of both grains. Then we used the excess energy of the grain boundaries that we measured earlier, the area of the grain boundaries, and the equation $E_{gb-excess} = \Sigma_i E^i_{GB-i} A_i$ to calculate the sum of the expected grain boundary excess energy before and after this rotation. Here, $E_{gb-excess}$ is the total excess energy of grain boundaries; A_i is the area for the i^{th} grain boundary; E_{GB-i} is the excess energy of i^{th} grain boundary. By these calculation we would expect the total grain boundary excess energy was about 78.5 ev before the rotation, and decreased to 77 ev after the rotation, while the grain boundary area increased from 930 $\AA^2$ to 1317 $\AA^2$. In simulation, as shown in Figure 6.23, the total energy dropped from -10599 ev to -10602 ev. The energy change was consistent with our calculation of the expected change of the sum of grain boundary excess energy.

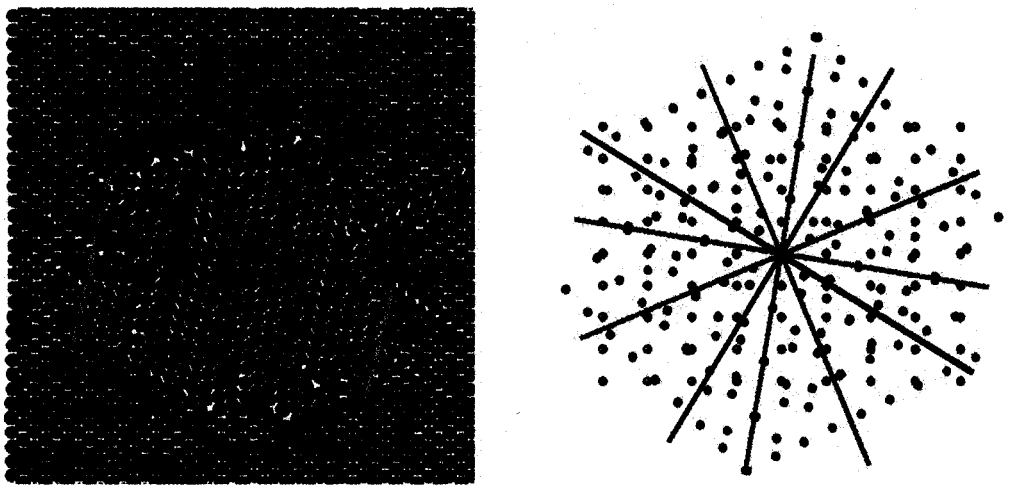

Figure 6.25: After the rotation, the grain is surrounded by mostly low-energy grain boundaries of as shown on the Tri-chromatic pattern.

6.1.4 Grain shrinkage mechanism

During system evolution, grain boundaries migrated towards the center of the embedded grain layer by layer, without changing their orientations. Figure 6.26 gives two snapshots taken in the simulation with $R_o = 35.26^o$ at different stages during the shrinkage of the embedded grain. These two images show that during grain shrinkage the normal orientations of the facets do not change. We observed that the migration was accomplished through the dislocation movement, interaction between stacking faults and dislocations, and plane glide, which will be explained more in the following sections of discussion. From the beginning of the simulation, grain shrinkage used this layer by layer mechanism, and the other grain shrinkage mechanism, sudden changes of grain orientation which caused part of the embedded grain to become part of surrounding grain, was only involved when the embedded grain's volume was small.

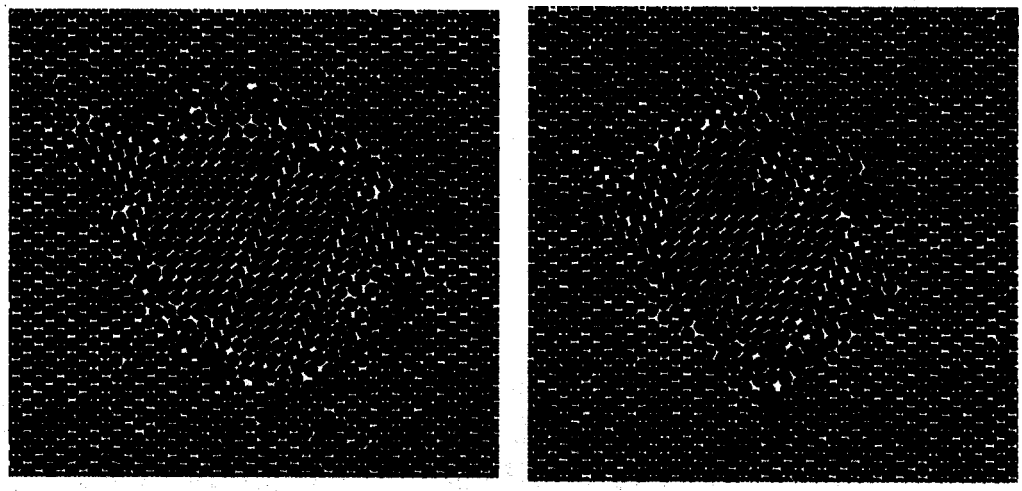

Figure 6.26: Two snapshots taken at different shrinkage stages of a simulation with $R_o = 35.26^o$. From the images we can tell that the although the inside grain's volume was changing, the direction of facets did not change much.

The following example shows how dislocations interacted with stacking faults during our simulations. The snapshots in Figure 6.27 were taken during a simulation with $R_o = 45^o$ and T=500K. As shown in the left image of Figure 6.27 taken before the interaction, a dislocation with Burger's vector equal to $\frac{1}{2}[\bar{1}1\bar{2}]$ existed not far from a stacking fault which ended at the grain boundary, both outlined by red lines. Finally and quickly in less then 160 simulation steps, which was about 0.16ps, the particles slid down along $[\bar{1}1\bar{2}]$ direction, which was the glide direction of the FCC glide system, and the dislocation combined with the stacking fault as shown in the right image of Figure 6.27. After the dislocation and stacking fault combined, the dislocation was still on the grain boundary but connected to a stacking fault. This mode of grain boundary migration occurred in most of our simulations.

In most of the simulations, we did not observe continuous shrinkage in our simulation time scales. We raised the temperature of these simulations to 1500K, which was about 85% of the melting temperature, and continued the simulations at this temperature. At these high temperatures, the embedded grains shrank continuously

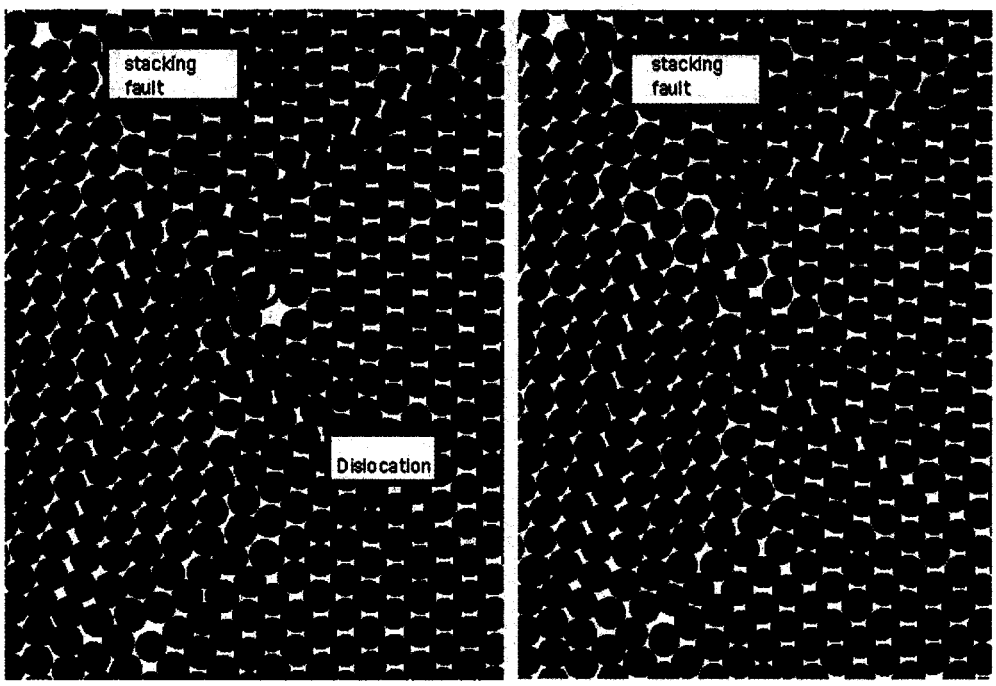

Figure 6.27: These two snapshots illustrate how stacking fault, dislocation, and glide system of the FCC worked together to move the particles around the grain boundaries.

until they disappeared in less than 60ps. Figure 6.28 shows the changes of the total energy during this simulation. The original simulation was started with $R_o = 45^o$ at 800K. 45ps after simulation started, system stopped evolution for 100ps without changing the total energy and the morphology. After 150ps of simulation at 800K, we raised the temperature to 1500K and continued the simulation at this temperature. After experiencing another equilibration period, the total excess energy of the system decreased continuously and the embedded grain shrank. The embedded grain totally disappeared around 195ps. Shrinkage of the grain occurring at this temperature had the same mechanism as the one occurring at lower temperature, such as 800K; the facets of the grain moved towards the center of the grain layer by layer without changing their orientations. Figure 6.29 gives snapshots taken at different times of the simulation when shrinkage was occurring.

6.2 Discussion

Since we used a columnar grain structure and periodic boundary conditions, there were only two geometric parameters free to vary: the misorientation between the grains described by R, and the normal orientations of the grain boundary planes in the common (110) plane, described by θ. Rotation of the grain causes the change of the R, while faceting changes the values of the θ for the grain boundaries. In our simulations, systems try to reduce their excess energy through varying these two geometric parameters. Both rotation and faceting have been observed.

6.2.1 Discussion of faceting

In all our simulations, before there is significant changes in R, facets started to form, even during the equilibration period of the simulations, which is within 2 ps after the start of the simulation. Before we start the simulation, the embedded grain has a cylindrical shape grain boundaries with almost all values of θ exist in the system even the area of each is small. This gives the possibility for the grain faceting into

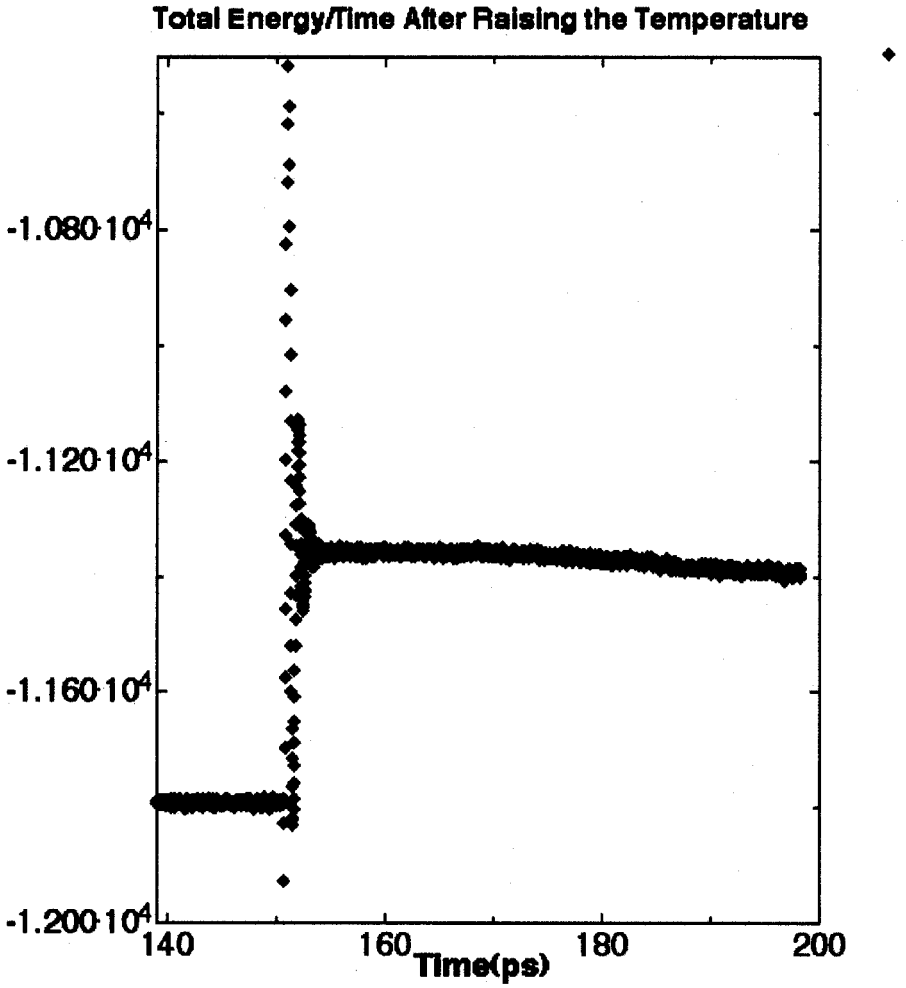

Figure 6.28: Total energy versus simulation time after temperature is raised to 1500K after simulation has been run for 150ps at 800K.

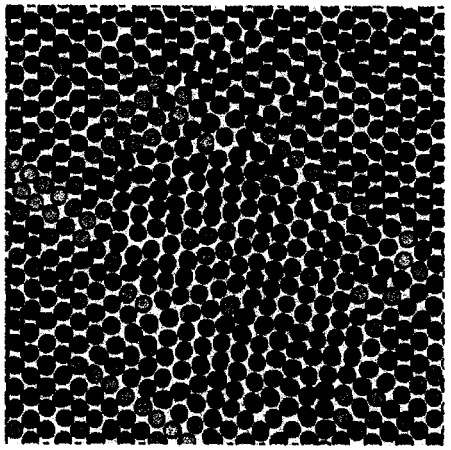

(a) Snapshot taken at 170ps

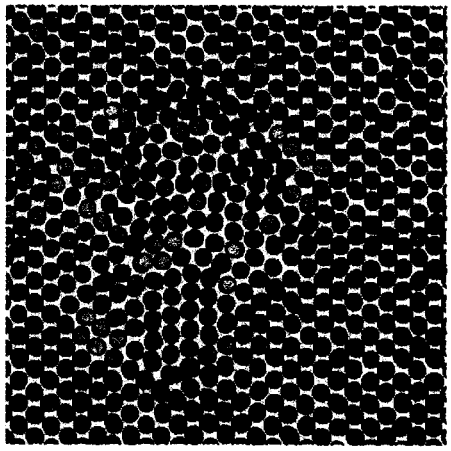

(b) Snapshot taken at 190ps

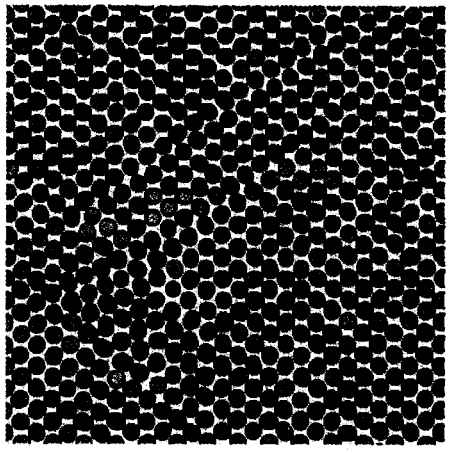

(c) Snapshot taken at 195ps

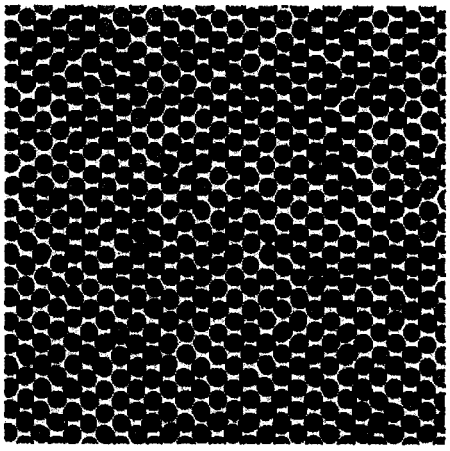

(d) Snapshot taken at 300ps

Figure 6.29: Shrinkage of the grain at high temperature

any grain boundaries. Therefore, facets formed quickly after simulation started, and mostly at the low energy grain boundaries. Most of these low energy grain boundaries are SDE grain boundaries with respect to normal orientation of the grain boundaries, but not all of them. Some are grain boundaries that allow low index planes of different grains to be parallel to each other, such as the one in system with $R_o = 35.26^o$ that allow one grain's $(1\bar{1}\bar{2})$ to be parallel to the other grain's $(1\bar{1}0)$. However, not all grain boundaries formed at equilibration period are special grain boundaries, such as those shown in Figure 6.24. These boundaries have higher mobility than those have low excess energies. However, if the general grain boundaries' energies are too high, only low energy grain boundaries exist. For example, the system with $R_o = 70^o$ only has facets on color mirror plane grain boundaries, and the embedded grain has a rectangular shape in the common (110) plane.

These low energy facets impede the shrinkage of the embedded grain which is shown in our shrinkage speed measurement. Figure 6.5 shows that after facets formed, the shrinking speed is greatly reduced. The examples of simulations with the same starting misorientation, $R_o = 35.26^o$, given in Figure 6.3 and 6.4, show that faceting into different grain boundaries at the beginning of the simulation is the only difference between these two systems with different behaviors in shrinkage. In the images shown in Figure 6.1 and 6.4, grain boundaries indicated by different colors have different geometric parameters: the pink boundaries are the color mirror plane grain boundaries of $R_o = 35.26^o$, the red boundaries are $(1\bar{1}\bar{1})//(001)$ grain boundaries, and the black ones are the $(1\bar{1}\bar{2})//(1\bar{1}0)$ grain boundaries. According to our grain boundary measurements, the excess energy of the pink boundary < excess energy of the red boundary < excess energy of the black boundary. Comparing the facets formed in Figures 6.3 and 6.4, we found that the structures that did not shrink have more low energy grain boundary facets. Most of the grain boundaries for this simulation were pink and red. The only black grain boundary was right in between two pink grain boundaries, and therefore its movement was restricted by two low-energy grain

boundaries on each side. In contrast, the grains that shrank completely during the simulation were surrounded mostly by red and black grain boundaries, which have higher energy than the pink ones. These results show that facets impede the shrinkage, and some low energy facets can pin the system in a local energy minimum state. We also measured grain shrinkage speed before and after facets formed, using simulation with $R_o = 60°$. As shown in Figure 6.5, before facets formed, which is around 2ps of the simulation time, the grain reduces 18% in volume. After 2ps, the grain shrinkage speed greatly decreased. From 2ps to 7ps of the simulation, the grain volume only reduced 3%. This also shows that systems in which grains facet into low energy grain boundaries shrink much slower than those that facet into high energy grain boundaries. For some of the simulations, after grains facet into some extremely low energy grain boundaries, the embedded grain's morphology stops changing, and the total energy of the system stop decreasing for very long times, over 150,000 steps (150ps) before we stop the simulations. Therefore, we conclude that some low energy facets can pin the systems in local energy minimum metastable states. The systems that are pinned at local minimum states do continue to evolve if the temperature of the system is raised.

In some of the simulations, stacking faults were formed to reduce the total excess energy. These stacking faults usually were created by the movement of dislocations. In our simulation, almost all stacking faults had a dislocation at their end and have the other end located at a grain boundary. The stacking faults found in our simulation were mostly in $(1\bar{1}1)$ plane, and the dislocations usually were [110] partial dislocations and their Burger's vectors were $\frac{1}{2}[1\bar{1}2]$. As shown in Figure 6.9, only some of the grain boundaries initiated stacking faults. We found that the grain boundaries that later had stacking faults attached originally had higher energy than the ones that did not have stacking faults attached. Therefore, we believe the driving force for the formation of the stacking faults is to reduce the excess energy of the grain boundaries. However, since the stacking faults initiate and grow though the movement of dislocations, we

believe the crystallography of the grain boundaries is also very important. If there are no appropriated dislocations or other line defects located at the grain boundaries, the possibility for the formation of the stacking faults is low. The stacking faults grow from the grain boundaries with the movement of the dislocation towards or away from the center of the embedded grain. Therefore, stacking faults exist both inside of the embedded grains and the surounding ones. However, the dislocations have difficulties to move across the whole enclosed grain if the grain size is too big. Therefore, we only observed stacking faults extended through the whole grain and have both ends attached on the grain boundaries in the embedded grains, but not in the surrounding grains.

We also found that sometimes, part of grain misorientation was changed while the number of stacking faults inside of the embedded grain was increasing. With many stacking faults added into the embedded grain and connected with each other, sometimes, big part of the grain changed its misorientation. Figure 6.10 shows an example that some connected stacking faults change part of the embedded grain's misorientation.

6.2.2 Discussion of rotation

We observed oscillating rotation both by watching the movies of the simulations and by recording the values of R using our "color by angle" algorithm. According to our data calculated through that algorithm, even for a single crystal system, there is a three degree rotation in R at 800K. Therefore, we believe the precision of the measurement of R is about 3 degrees. Simulations with $R_o = 90^o$, and 35.26^o do not rotate within the limites of our measurement, while simulations with other R_o values rotate during the simulations. According to the data given in Table 6.2, the magnitude of the oscillating rotation ranges between 7 to 10 degrees.

We investigated several factors that might be responsible for the oscillating rotation. We first investigated the possibility that the starting net angular momentum

of the system causes the oscillating rotation. In all of our simulations, we randomly assigned initial velocities to the particles; therefore, the embedded grain could have a net angular momentum before the simulation starts. However, if this is the main reason for the rotation, we should get similar magnitudes of rotation angles for all simulations; rotation magnitude of a simulation with $R_o = 35.26^o$ should not differ much from a simulation with $R_o = 45^o$ or 60^o. After doing simulations at least four times with each R_o value, we found that the magnitudes of the rotations are replicable. Simulations with $R_o = 90^o$, and 35.26^o show no rotation while simulations with other R_o show rotation of at least 7 degrees. Therefore, the net angular momentum is not the reason for the oscillating rotation.

We also investigated the possible connection between rotation and the layer by layer shrinkage. After the GB migrates one atomic layer, the layer of atoms adjacent to the boundary has the identical arrangement of atoms as the previous layer, but identical sites in the plane are shifted in the plane of the boundary. This shift will be different for the structures on either side of the boundary. If registry between equivalent sites on either side of the boundary must be maintained for minimizing the energy of the boundary, then the entire lattice of one side of the boundary must be translated. In our system, such a translation could be accommodated by a rotation of the embedded grain. However, the magnitude of the changes of R correlated with shrinkage in this case should be small. Assuming movement of the particles at grain boundary is not larger than half of the lattice constant of the structure, if grain size in diameter is about fifteen times the lattice constant, which is the initial grain size we usually used, the rotation of the grain should be less than 4 degrees per atomic layer. But this type of rotation should increase with the decrease of the grain size. On the contrary, we observe the magnitude of rotation decreases during simulation as the grain shrinks. Moreover, the rotation should occur only when shrinkage of the grain occurs, which we do not observe in our simulations. Therefore, this is not likely to be the cause of rotation.

Since all of our simulations occur at high temperature, such as 800K, thermal effects are another factor that might influence the rotation. Therefore, we also consider the impact of lattice vibration. For our system, the lattice vibration frequency is on the scale of approximately 1E13 Hz. In our simulation, rotation changes direction in the time scale of $5E13$ to $1E-12$ second. Thus the rotation could relate to lattice vibration. However, that could not explain why simulations with certain R_o values rotate less than the others, such as $R_o = 90^o$, and 35.26^o. Therefore, at least, we do not expect that thermal effects would be the main element influencing the magnitude of the rotation.

We believe rotation has an oscillating pattern strongly related to the facets of the grain. Our systems reduce excess energy through both rotating and faceting, which change the geometric parameters of R and θ of the systems. θ changes faster than R at the beginning of the simulations. We observed that the grains usually facet into low energy grain boundaries with respect to the R_o. Rotation changes the value of R. Although we do not explicitly measure the change of the normal orientations of grain boundaries, we visually observe that grain boundaries stay at the same planes of atoms chosen when the initial facets form and do not change during grain rotation. Thus the crystallography of the facets does not change, which implies that the rotation of the facet planes are limited because of the constraints of the surrounding grain. When rotation occurs, R of the embedded grain changes so that the facets are not low energy grain boundaries any more because they do not rotate with the embedded grain. Thus, the excess energy of the grain boundaries increases after rotation. This explains why the local minimum energy state is pinned to a particular misorientation by the facets, and even through rotation occurs in most of our simulations, the average R values of each simulation do not differ too much with the R_o.

To keep the normal orientations of the grain boundaries in the same directions when the embedded grain is rotating, we observe the particles close to the facets need to glide along facets planes, which we believe generates stress in the regions

close to the grain boundaries and close to the center of the embedded grain. This stress increases with increasing of the rotation angle, and forces the embedded grain to rotate back when the stress is too big. We believe this is the primary cause of the oscillating rotation.

Because facets are not rotating with the grain, unlike the assumption made by Harris and Haslam [44, 39], the oscillating rotation is not a rigid-body rotation.

Because $R_o = 90^o$ is a SDE with respect to misorientation, and no rotation occurs with the system starting with this R_o, it is very likely that $R_o = 90^o$ is a local energy minimum with respect to misorientation in FCC (110)//(110) system. The system with $R_o = 35.26^o$ is not a SDE with respect to misorientation. This misorientation allows the formation of more low energy grain boundaries, and the excess energy of grain boundaries are extremely low compared with the grain boundaries at other R, even though they are not CSL grain boundaries. In the simulations, we observed more facets exist in the system is more than the systems with other R_o values, and therefore, we believe that more stress would be generated along these facets if rotation occurs. Thus, it should be more difficult for the embedded grain to rotate with $R_o = 35.26^o$. On the contrary, for the system with $R_o = 70^o$, as shown in Figure 6.13, only facets at color mirror plane grain boundaries exist in the facets because the general grain boundaries at this misorientation have much higher energy than the color mirror plane grain boundaries. Therefore the magnitude of rotation with $R_o = 70^o$ is bigger, about 15 degrees.

In summary, low energy facets not only impede the shrinkage of the grain, but also impede the grain from rotating continuously and reduce the magnitude of the oscillating rotation.

Another type of rotation observed in our simulations is actually an abrupt change of misorientation of part or all of the embedded grain through plane gliding. As shown in Figure 6.22, several planes slid down along the $< 1\bar{1}2 >$ direction to achieve the same misorientation as that of the surrounding grain. The energy of the system

dropped after this type of rotation. In example showed in Figure 6.23, Figure 6.24, and Figure 6.25, part of the embedded grain change the misorientation which changes some high energy facets to low energy facets while facets did not rotate with the grain. Therefore, we believe this rotation was triggered by those high energy grain boundaries trying to become low energy grain boundaries. Another example in Figure 6.10 shows that sometimes formation of the stacking faults can also change misorientation of part of the grain.

In experiments, to observe grain rotation, researchers take sequential TEM images at the same spot, as shown in Figure 2.1. [44] Harris et al. concluded that rotation had happened by observing the angular changes between twins in adjacent grains. However, there is at least one hour time difference between each image. Thus, because there is no direct observation of the rotation of the grains, it is possible that the grain misorientation changed due to plane glide or stacking faults formation as observed in our simulations.

6.2.3 Discussion of shrinkage mechanism

The embedded grains reduce their volume through two modes in our simulations: grain boundary migration, and rotation of at least part of the embedded grain. For both mechanisms, low energy facets play important roles by impeding grain rotation and shrinkage of the grain. Systems faceting into lower energy grain boundaries take much longer simulation times to shrink and sometime these facets even pin the system into a metastable state in which the shrinkage stops. However, if we raise the temperature, the embedded grain of the system continues shrinking and eventually disappears, as shown in Figure 6.28. Because at higher temperature, it is easier to surmount the energy barrier of the movement of the grain boundaries.

For the systems shrinking continuously, at temperatures of both 800K and 1500K, the grains shrink layer by layer without changing the normal orientations of the grain boundaries. Grain boundaries with higher excess energy show higher mobility in

migration, and therefore help the grain to shrink faster than in the systems with grain boundaries having lower excess energy. Grain boundary migration occurs through local atomic movement enabled by the excess volume around grain boundaries. We observed dislocation motion, interactions between stacking faults and dislocations, and plane glide in our simulations, all associated with grain boundary migration. In shrinkage, particles on the boundaries glide along grain boundary planes using the excess volume on the boundaries. The movement of the these atomic planes will make these particles become part of the surrounding grains. Followed by this plane glide, dislocations usually move towards the center of the grain, and make the adjacent particle plane closer to the center of the grain the new grain boundary. Thus, the grain boundary moves a layer towards the center of the grain.

Even though systems evolve faster at 1500K degree than at 800K, the shrinkage mechanism is the same. So temperature only influences the evolution speed of the systems but not the behavior. Therefore we believe, with much lower temperature, the shrinkage mechanism in our simulations would still be the same and represent what might really occur in the experimental situation.

When the embedded grain has shrunk to a smaller size, sometimes several layers of the particles glide down together and change part of the grain's misorientation abruptly. Although we call this a second type of rotation, this is more of sudden change of misorientation than of rotation.

R. Bullough and et al. concluded in their study that fcc stacking fault energy in Lennard-Jones crystal is low. [78]. In their research, the stacking fault energy is $-0.022erg/cm^2$, which is $-1.372E-4eV/nm^2$, with lattice constant equal to 3.828 $\mathring{A}$, and ϵ equal to $-164E-16$ erg, which means HCP structure is more preferred. We also used kSan to calculate the energy of stacking faults. As shown in Figure 6.30, we constructed a FCC structure with 3 stacking faults in (111) plane. The layer structure has been indicated under the image. The total energy of this system was $-2.0955E4 \pm$ 2.2834 eV, and total energy of the same size the bulk system was

$-2.0955E4 \pm$ 2.1585 eV. The area of the stacking faults was 44 nm^2. Therefore, the excess energy of this system is 0 eV and the stacking faults energy in our simulation is 0 eV/nm^2. Thus, our simulation results may be more similar to what occurs in FCC materials with low stacking faults, such as copper, but not materials with high stacking fault energy, such as aluminum.

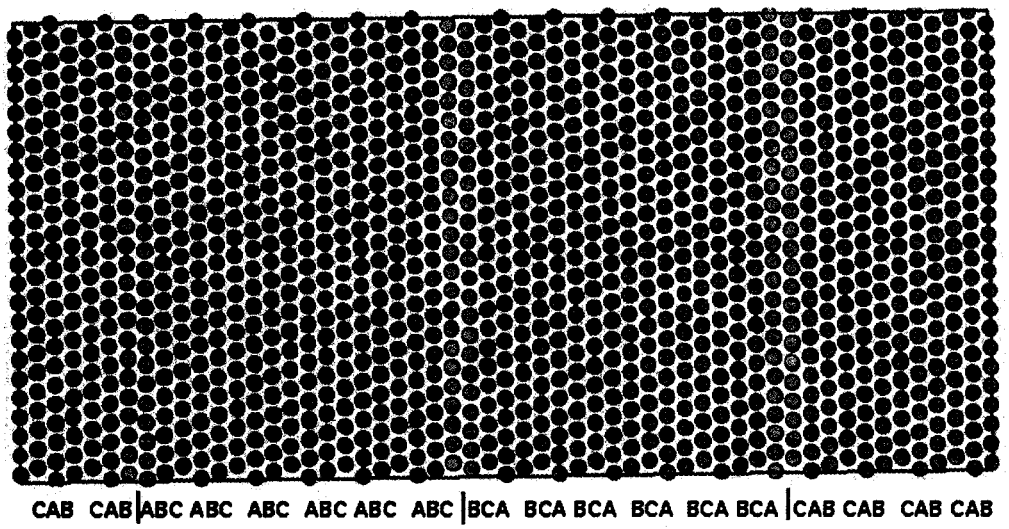

Figure 6.30: The structures we used to calculate the stacking faults in (111) plane. 3 stacking faults are included.

Chapter 7

CONCLUSION

In this thesis, we used two different methods to study grain boundaries in FCC bicrystalline (110)//(110) systems. We first studied our polycrystalline systems using color groups which give us information about the symmetry of the systems, and more importantly, tell us the symmetry-dictated extrema positions of our system, which gives a good starting point for further studies. Then, we used molecular dynamics computer simulations to observe the evolution of the system beginning with special geometric characteristics, which provided information on the relation between the geometric parameters and the properties of the grain boundaries.

To understand the influence of one particular geometric parameter on the properties of the bicrystalline structure, we restricted the degrees of freedom to two geometric parameters. We constrained the (110) directions of two grains to be parallel and only allowed rotation to happen in the common FCC (110) plane for both grains. We define the geometric parameter that describes this rotation by R. We also constrained our grain boundary planes to be parallel to the common [110] direction of both grains, therefore all grain boundaries in our study are FCC (110) tilt grain boundaries. Thus, the other geometric parameter that is free to vary in our system is the normal orientation of the grain boundaries in common FCC (110) plane of both grains, which described by θ in our study.

We first studied the dichromatic patterns of FCC (110)//(110) system with $R = 90^o$, and $R = 45^o$. The color group of the DCP with $R = 90^o$ is $G_{DCP} = 4'/mmm'(mmm)$; and the color group of DCP with $R = 45^o$ is $G_{DCP} = m'm'm(2/m)$. We also found that, since we restricted the rotation to the (110) plane, the DCP with a general R is

$G_{DCP} = m'm'm(2/m)$. So geometrically, $R = 45^o$ is not a special misorientation in the (110) plane of the FCC system, while $R = 90^o$ is. SDE studies with respect to the misorientation revealed that $R = 90^o$ is the only SDE with respect to misorientation for FCC (110)//(110) bicrystalline systems. With $R = 90^o$, grain boundaries on top of the color mirror planes and classical mirror planes are both SDE with respect to grain boundary normal orientation. With the other Rs, grain boundaries located on the color mirror plane are SDE with respect to grain boundary normal orientation. The group of the Wulff plot of our structures is the same as the color group of each of our bicrystalline systems. For the SDE with respect to rotation, $R = 90^o$, $W = 4/mmm$; for the other general DCP with $R \neq 90^o$, $W = mmm$.

To use MD simulation to study these particular research topics, we improved the kSan, the MD simulation software, and developed a new algorithm to better visualize the system. The new algorithm is called "**Axis Angle Value**", which allows us to color particles according to the misorientation of the grain to which the particles belong. By using this algorithm we were able to track the change of the misorientation, R, of the system, and visualize the defects of the system more easily. Although we used constant volume and constant temperature in our simulations, our pressure tests showed limited effects of pressure for the system during the simulations.

In our MD simulations studies, we first calculated the excess energies of the SDE grain boundaries and compared with general grain boundaries. According to our calculations, all these grain boundaries are low excess energy grain boundaries. FCC (110)//(110) system with $R = 35.26^o$ have more low energy grain boundaries than the other systems. It not only has color miorror plane grain boundaries, but also has a grain boundary that allows one grain's $(1\bar{1}\bar{1})$ to be parallel to another grain's (001) plane; and a grain boundary that allows one grain's $(1\bar{1}\bar{2})$ to be parallel to the other grain's $(1\bar{1}0)$. Even though these grain boundaries are not SDE, their excess energy are very low. None of our low excess energy grain boundaries are CSL grain boundaries.

Using color symmetry information as the starting point, we designed our structures for MD simulation, which also let us focus on limited geometric parameters. Our structure has one columnar grain embedded in another bigger fcc grain with both grain's [110] directions to be parallel. In this structure, the geometric parameters that are free to vary are R, the rotation in the common (110) plane, and θ, the normal orientation of the grain boundaries in the common (110) plane. We used conjugate gradient minimizer (CGM) for 40 to 60 simulation steps to get rid of excess stress caused by particles' overlapping at the beginning of the simulations. The number of the CGM steps did not influence the later behavior of the systems. Every simulation experienced an equilibration period during which temperature varied greatly for about 2ps after we started to iterate the system with the Verlet method.

Facets started to form at the beginning of the simulation, even during the equilibration period. Embedded grains tended to facet into low energy grain boundaries. We observed some of the embedded grains shrank continuously and disappeared quickly in less than 10,000 simulation steps, while others were pinned in low energy minimum states and stopped shrinking. Whether embedded grains would shrink continuously or not depended on which grain boundaries they formed at the beginning of the simulations, but not the starting misorientation, R_o. In the early stage of the simulation, grain shrinkage occurred by layer-by-layer movement of planar grain boundaries. High energy grain boundaries have higher mobility than the low energy grain boundaries, and grains which faceted into higher energy grain boundaries shrank faster.

When R of the system was not a local energy minimum with respect to misorientation, we observed rotation from the beginning of the simulation which had an oscillating pattern. Grain did not rotate continuously to one direction, but changed direction alternatively. Facets did not rotate with the embedded grain, thus the particles close to the facets glided along the particle planes to keep grain boundaries' normal orientations and positions unchanged. This increased the stress between the

particles that are close to the facets and those close to the center of the embedded grain, and eventually stopped the rotation and forced it to rotated back. Since these facets formed at the beginning of the simulation and only have low energy when R is close to R_o, they pinned the system into R_o and inhibited it from continuous rotation. No rotation was observed for systems with $R_o = 90^o$ and $R_o = 35.26^o$. $R_o = 90^o$ is a SDE with respect to misorientation and likely to be a local energy minimum state of misorientation. $R = 35.26^o$ allows the system to have more grain boundaries with low energy, such as the grain boundaries with one grain's $(1\bar{1}\bar{1})$ plane parallel to the other grain's (001), and/or one grain's $(1\bar{1}\bar{2})$ parallel to the grain's $(1\bar{1}0)$. Therefore, more low energy facets were observed in the system with $R_o = 35.26^o$, and more stress would be brought into the system if rotation occurred. Thus, these grain boundaries hindered the rotation. On the contrary, the systems with other R_o values, such as $R_o = 70^o$, had bigger magnitude in rotation because general grain boundaries at this R have extremely high energy and only color mirror plane grain boundaries exist.

After grain size decreased, we observed another type of orientation change in the embedded grain, which caused part of the embedded grain to collapse. This abrupt change of misorientation always correlates with sudden drops of the total energy. We still call it rotation because this abrupt change of the system results in the change of misorientation. We found that plane slide is the mechanism of this type of grain rotation. It always requires extra space around the grain boundaries, such as caused by dislocations. In some cases, reducing the embedded grain's volume and the area of the grain boundaries is the driving force for the abrupt change of misorienation; in other cases, the driving force for the abrupt change of misorientation is to change the status of the grain boundary from high to low energy.

All these observations showed strong connection between grain faceting, rotating, and the morphology changes of grains.

We also observed interactions between stacking faults and grain boundaries. After facets formed, some stacking faults also formed. They started at the grain boundary

area and extended away from grain boundaries with the movement of dislocations. According to our measurements, we found that the energy/particle in the stacking fault area was not higher than in the other part of the grain, and lower than in the grain boundary area. We compared the energy of the particles inside the grain boundary with and without stacking faults attached and found that at least in the some cases, stacking faults will decrease the energy of the particles on the grain boundaries. During the evolution of the system, we found that the number and the area of the stacking faults did not decrease, but increased, and decreased the total excess energy of the system. Stacking faults were only found in glide planes of the FCC system, and could only be initiated by certain grain boundaries that have higher energy where dislocation or other line defects are located.

BIBLIOGRAPHY

[1] D.Farkas H.Van Swygenhoven. Grain boundary structure in polycrystalline metals at the nanoscale. *Physical Review B*, 62(2):62, 2000.

[2] S.Yip D.Wolf. *Materials Interfaces, atomic-level structure and properties.* Chapman & Hall, 1992.

[3] W.T Read and W.Shockley. Dislocation models of crystal grain boundaries. *Physical Review*, 78(3):275, 1950.

[4] D.N.Seidman. Subnanoscale studies of segregation at grain boudnaries:simulations and experiments. *Annual Review of Materials Science*, 56(11):150, 2004.

[5] M.Takashima. Correlation of grain boundary character with wetting behavior. *Interface Science*, 9(3-4):265, 2001.

[6] Gretchen Kalonji. Symmetry principles in the physics of crystalline interfaces. *PhD thesis. M.I.T.Cambridge, MA*, page 113, 1982.

[7] H. Seyazaki M. Koiwa and T. Ogura. A systematic study of symmetric tiltboundaries in hard-sphere f.c.c crystals. *Acta metallurgica*, 32(1):171, 1984.

[8] H. Gleiter M. Weins and B. Chalmers. Structure of symmetric tilt boundaries in f.c.c metals. *Scripta Metallurgica*, 4(3):235, 1970.

[9] V. Randle. *The Role of the Coincidence Site Lattice in Grain Boundary Engineering.* The Institute of Materialsl, 1996.

[10] P.H.Pumphrey. *Grain Boundary Structure and Properties.* Academic Press, 1976.

[11] K. Ikeda N.Takata, T. Mizuguchi and H. Nakashima. Atomic and electronic structure of ¡110¿ symmetric tile boundaries in palladium. *Materials Transactions*, 45(7):2099, 2004.

[12] G. Palumbo P.Lin and K.T.Aust. Experimental assessment of the contribution of annealing twins to csl distributions in fcc materials. *Scripta Materialia*, 36(10):1145, 1997.

[13] A.P.Sutton and R.W. Balluffi. On geometric criteria for low interfacial energy. *Acta Matallurgica*, 35(9):2177, 1987.

[14] H. Gleiter G. Herrmann. Investigation of low energy grain boundaries in metals by a sintering technique. *Acta Metallurgica*, 24(4):353, 1976.

[15] H.Gleiter H.Sautter. The effect of solute atoms on the energy and structure of grain boundaries. *Acta Metallurgica*, 25(4):467, 1977.

[16] M.F.Chisholm D.A.Smith and J. Clabes. Special grain boundaries in $yba_2cu_3o_7$. *Applied Physics Letter*, 53(5):2344, 1988.

[17] H.Gleiter H.Sautter and G. Baro. Effect of solute atoms on the energy and structure of grain boundaries. *Acta Matallurgica*, 25(4):467, 1977.

[18] A.M.Donald and L.M. Brown. Grain boundary faceting in cu-bi alloys. *Acta Matallurgica*, 27(1):56, 1979.

[19] K.T.Aust. *Chalmer Anniversary Volume.* Pergamon Press, 1981.

[20] G.Palumbo and K.T.Aust. *Special Properties of* Σ *Grain Boundaries.* Chapman & Hall, 1992.

[21] H.Gleiter. Effect of inclination on gratin boundary. *Acta Matallurgica*, 18(1):23, 1970.

[22] M.McLean. Grain-boundary energy of copper at 1030 degree c. *Journal of Materials Science*, 8(4):571, 1973.

[23] A.K.Mukherjee A.H. Chokshi. Analysis of cavity nucleation in superplasticity. *Acta Metallurgica*, 37(11):3007, 1989.

[24] H. Gleiter V.Y. Gertsman, M. Hoffmann and R. Birringer. Study of grain size dependence of yield stress of copper for a wide grain size range. *Acta metallurgica et Materialia*, 42(10):3539, 1994.

[25] P.M.Hazzledine R.A. Masumura and C.S. Pande. Yield stress of fine grained materials. *Acta Materialia*, 46(13):4534, 1998.

[26] D. Owen S.Ganapathi and A.Chokshi. The kinetics of grain growth in nanocrystalline copper. *Scripta Metallurgica et Materialia*, 25:2699, 1991.

[27] C.Natter M. Krill and R. Birringer. *Grain Growth in Polycrystalline Materials, III.* Warrendale PA, 1998.

[28] T.R.Marlow and C.C Koch. *Synthesis and Process of Nanocrystalline Materials.* Warrendale, PA, 1996.

[29] B.Guenther A.Kumpmann and H.D. Kunze. Thermal stability of ultrafine-grained metals and alloys. *Materials Science and Engineering A*, A168:165, 1993.

[30] R.Z.Valiev V.Y. Gertsman, R.Birringer and H. Gleiter. On the structure and strength of ultrafine-grained copper produced by severe plastic deformation. *Scripta Metallurgica et materialia*, 30(10):2, 1994.

[31] D.Weaire F. Bolton. Rigidity loss transition in a disordered 2d froth. *Physical Review letter*, 65(27-31):3449, 1990.

[32] D. Weaire J.P. Kermode. 2d-froth: a program for the investigation of 2-dimensional froths. *Computer Physics Communications*, 60(1):75, 1990.

[33] H.V Atkinson. Theories of normal grain growth in pure single phase systems. *Acta Metallurgica*, 36(3):469, 1988.

[34] C.V. Thompson. Relative rates of secondary and normal grain growth. *Acta Metallurgica*, 35(4):887, 1987.

[35] M.P.Anderson. Inhibition of grain growth by second phase particles: Three dimensional monte carlo computer simulations. *Scripta Metallurgica*, 23(5):753, 1989.

[36] Grest.G.S. Domain-growth kinetics for the q-state potts model in two and three dimensions. *Physical Review B*, 38(7):4752, 1988.

[37] J. R. Banavar M.G. Sharma S. Kumar, S. K. Kurtz. Properties of a three-dimensional poisson-voronoi tesselation: a monte carlo study. *Journal of Statistical Physics*, 67(3):523, 1992.

[38] M. Marder. Soap-bubble growth. *Physical Review A*, 36(1):438, 1987.

[39] S.R.Phillpot D. Wolf A.J.Haslam, D. Moldovan and H. Gleiter. Combined atomistic and mesoscale simulation of grain growth in nanocrystalline thin films. *Computational Materials Science*, 23(1):15, 2002.

[40] L.S.Shvindlerman G. Gottstein, V. Sursaeva. Effect of triple junctions on grain boundary motion and grain microstructure evolution. *Interface Science*, 7(3-4):273, 1999.

[41] H. Jonsson S.G.Srinivasan, J.W. Cahn and G. Kalonji. Properties of a three-dimensional poisson-voronoi tesselation: a monte carlo study. *Act Materialia*, 47(9):2821, 1999.

[42] W.W. Willigan M.Ke, S.A. Hackney and E.C. Aifantis. Observation and measurement of grain rotation and plastic strain in nanostructured metal thin films. *Nanostructured Materials*, 5(6):689, 1995.

[43] K. Sumimoto T. Shibayanagi and Y. Umakoshi. Grain rotation in ni_3al. *Scripta Materialia*, 34(9):1491, 1996.

[44] V.V.Singh K.E.Harris and A. H. King. Grain rotation in thin films of gold. *Acta Materialia*, 46(8):2623, 1998.

[45] D.Wolf D.Moldovan H. Gleiter A.J. Haslam, S. R. Phillpot. Mechanisms of grain growth in nanocrystalline fcc metals by molecular-dynamics simulation. *Materails Science and Engineering A*, 318(1-2):293, 2001.

[46] Ron Lifshitz. The rebirth of crystallography. *Personal Opinion*, page 342.

[47] A. V. Shubnikov. *Colored Symmtry.* New York, Macmillan, 1964.

[48] D. Gratias L.A.Bendersky J.W.Cahn. A crystalline aggregate with icosahedral symmetry: Implication for the crystallography of twinning and grain boudaries. *Philosophical Magazien B*, 60(6):837, 1989.

[49] H. Jonsson G. Kalonji S.G.Srinivasan, J.W.Cahn. Excess energy of grain-boudary trijunctions: an atomistic simulation study. *Acta Materialia*, 47(9):2821, 1999.

[50] G.Kalonji J.Cahn. Symmetries of grain-boundary trijunctions. *Journal of Physics and Chemistry of Solids*, 55(10):1017, 1994.

[51] Th. Karakostas G.P. Dimitrakoplulos. Symmetry analysis of interface triple junctions. *Acta crystallographica Section A*, 52(1):62, 1996.

[52] Ron Lifshitz. Theory of color symmetry for periodic and quasiperiodic cystals. *Review of Modern Physics*, 69(4):1181, 1997.

[53] J.J. Burchhardt B. L. Van Der Waerden. Farbgruppen. *Z. Kristallography*, 115:231, 1961.

[54] D. Gratias J.Cahn D. Shechtman, I. Blech. Metallic phase with long-range orientational order and no translational symmetry. *Physical Review Letters*, 53(20):1951, 1984.

[55] Niizeki. Special points of (2+1)-reducible quasilattices in three dimensions. *Journal of Physics A*, 23(20):4569, 1990.

[56] Niizeki. Three-dimensional black-and-white bravais quasilattices with (2+1)-reducible point groups. *Journal of Physics A*, 23(21):5011, 1990.

[57] Ron Lifshitz. Lattice color groups of quasicrystals. *6th Intl. Conf. on Quasicrystals, Tokyo, Japen*, page 103, 1998.

[58] J.Cahn G.Kalonji. Symmetry constraints on the orientation dependence of interfacial properties: the group of wulff plot. *Journal De Physique*, 43(6):25, 1982.

[59] A. Lebedev A. Eflimov. Symmetry constraints and epitaxial-growth on non-isomorphic substrate. *Thin Solid Film*, 260(1):111, 1995.

[60] J. Cahn G.Kalonji. The stacking-fault tetrahedron. *Philosophical Magazine A*, 53(4):521, 1986.

[61] W.Graig Carter J.E.Blendell and C. A. Handwerker. Faceting and wetting transitions of anisotropic interfaces and grain boudnaries. *Journal of the American Ceramic Society*, 82(7):1889, 1999.

[62] G.R.Hugo and B.C. Muddle. the morphology of precipitates in an al-ge alloy i. experimental-observations. *Acta Metallurgica et Materialia*, 38(2):351, 1990.

[63] G.R.Hugo and B.C. Muddle. the morphology of precipitates in an al-ge alloy ii. analysis using symmetry. *Acta Metallurgica et Materialia*, 38(2):365, 1990.

[64] U.Dahmen. Evolution of ge precipitate morphology in al. *MRS Bulletin*, 19(6):22, 1994.

[65] R. Pond H. Jiao, M. Aindow. Precipitate orientation relationships and interfacial structures in duplex strainless steel zeron-100. *Philosophical Magazine*, 83(16):1867, 2003.

[66] M.P. Allen and D.J. Tildesley. *Computer Simulation of Liquids.* Clarendon Press Oxford, 1987.

[67] J.M.Haile. *Molecular Dynamics Simulation: Elementary Methods.* John Wiley and Sons, INC, 1992.

[68] G. Ciccotti J.P.Rychaert and H. Berendsen. Numerical integration of the cartesian equations of motion of a system with constratins: Molecular dynamics of n-alkanes. *Journal of Computational Physics*, 23(3):327, 1977.

[69] D. Fincham. Dynamic simulation of molecular and ionic materials. *Journal of Molecular Graphics*, 12(1):29, 1994.

[70] D. DiNola H. Berendsen, J. Van Gunsteren and J. Haak. Molecular dynamics with coupling to an external bath. *Journal of Chemical Physics*, 81(8):3684, 1984.

[71] W.G. Hoover. *Rhelology Via Nonequilibrium Molecular Dynamics (1).* Lecture Notes in Engineering, 1983.

[72] S.A. Teukolsky W. H. Press, B.P. Flannery and W.T. Vetterling. *Numerical Recipes in C: the art of scientific computer.* Cambridge University Press, 1992.

[73] H. Gleiter S.R.Phillpot, D.Wolf. Molecular-dynamics study of the synthesis and characterization of a fully dense, three-dimensional nnaocrystalline material. *Journal of Applied Physics*, 78:847, 1995.

[74] F.D. Di Tolla J. Schiotz, T. Vegge and K. W. Jacobsen. Atomic-scale simulations of the mechanical deformation of nanocrystalline metals. *Physical Review B*, 60:11971, 17.

[75] U.Dahmen. Evolution of ge precipitate morphology in al. *MRS Bulletin*, 19(6):22, 1994.

[76] J.W. Cahn. *Interfacial Segregation.* American Society for Metals, Metals Park, Ohio, 1979.

[77] A.P.Sutton and R. W. Balluffi. *Interfaces in Crystalline materials.* Oxford Science Bulications, 1995.

[78] J.A. Venables R.Bullough, H.R. Glyde. Stacking-fault energy and many-body force effects in solid argon. *Physical Review Letters*, 17(5):249, 1966.

[79] S.C. Mehta and D. A. Smith. *Grain Boundary Engineering.* Inst. Min. Met. & Petrol. Montreal, 1994.

[80] D. Gratias J.W. Cahn D. Chechtman, I.Blech. Metallic phase with long-range orientational order and no translational symmetry. *Physical Review Letters*, 53(20):1951, 1984.

[81] H.J. Gao M. Duchaineau T.D. De la Rubia F Abraham, R. Walkup and M. Seager. Simulation materials failure by using up to one billion atoms and the world's fastest computer: Work-hardening. *Proc. Natl. Acad. Sci.*, 99:5783, 2002.

[82] R.K. Kalia P. Vashishta and A. Nakano. Multimillion atom molecular dynamics simulations of nanostructures on parallel computers. *Journal of Nanoparticle Research*, 6(1):119, 2003.

[83] P.Kraulis. Molscript-a program to produce both detailed and schematic plots of protein structures. *Journal of Applied Crystallography*, 24(5):946, 1991.

[84] R.A.Sayle and E Milner-White. Rasmol-biomolecular graphics for all. *Trends Biochemical Science*, 20:119, 1995.

[85] Z. Chen L.Shen. An inverstigation of the effect of interfacial atomic potential on the stress transition in thin films. *Modelling Simulation: Materials Science and Engineering*, 12:347, 2004.

[86] J.Li. Atomistic visualization. *Handbook of Materials Modeling*, page 1051, 2005.

[87] P.Vashishta A. Nakano, R.K.Kalla. Scalable molecular-dynamics, visualization, and data-management algorithms for materials simulations. *Computing in Science & Engineering*, page 39, 1999.

VITA

Yue Huang was born in Nanjing, China in 1978. Yue graduated from Tsinghua University in 2000 with a B.S. in Materials Science and Engineering. She is receiving her PhD from the University of Washington in Materials Science and Engineering and Nanotechnology. She also earned a certificate in Environmental Management from the University of Washington in June, 2006.